The mineralogy and chemistry of the Spro pegmatite mine, Nesodden, and their genetic implications

Pedro Faria

Master Thesis in Geosciences
Study programme: Geology of Mineral Resources
60 credits

Department of Geosciences
Faculty of Mathematics and Natural Sciences

UNIVERSITY OF OSLO

01 June, 2019

Supervisor: Prof. Axel Müller (Natural History Museum, University of Oslo)
Co-supervisor: Prof. Henrik Friis (Natural History Museum, University of Oslo)

This work is published digitally through DUO – Digitale Utgivelser ved UiO
http://www.duo.uio.no
It is also catalogued in BIBSYS (http://www.bibsys.no/english)

Glossary

BSE **–** Backscattered Electrons

CL **–** Cathodoluminescence

EDS **–** Energy Dispersive x-ray Spectroscopy

EMPA– Electron Microprobe Analyzer

GMV **–** Geologisk Museums Venner

GPS – Global Positioning System

HREEs – Heavy Rare Earth Elements (Gd – Lu)

IBMA – Ion Beam Micro Analysis

ICP-MS –Inductively Coupled Plasma Mass Spectrometry

LCT – Lithium-Cesium-Tantalum

LREEs – Light Rare Earth Elements (La - Eu)

MSREL– Muscovite-Rare-Element

NFS **–** Nesodden Fault Segment

NYF – Niobium-Yttrium-Fluorine

ppb – parts per billion

PPL – Plane Polarized Light

ppm – parts per million

REEs – Rare Earth Elements (Lanthanides: La-Lu)

SE **–** Secondary Electrons

SEM – Scanning Electron Microscope

SIMS – Secondary Ion Mass Spectrometer

XPL – Cross Polarized Light

XRF – X-Ray Fluorescence

Acknowledgments

First and foremost, I would like to express my extensive gratitude to my advisors, Axel Müller for his support, patience, and guidance; and Henrik Friis for his availability, advice, and attention to detail. Their presence and advising were pivotal for the entire process and essential for the study development.
I would also like to thank Nanna Rosing-Schow and Øyvind Sunde for their help. Both helped me tremendously in crucial topics and important details. I also have to thank Salahalldin Akhavan for executing thin section preparation and epoxy cast polishing at Blindern; Nélia Castro and Eirini Zacharaki for their help in conducting SEM/EDS analyses; Muriel Erambert for her instruction during EMPA analyses and Gunborg Bye Fjeld for her availability and support in rock crushing, splitting and milling.

In addition, I would like to thank the ACME Laboratories in Vancouver, Canada, for the performed solution ICP-MS for whole rock chemistry; and the GFZ (German Research Centre for Geosciences) in Potsdam, Germany, and specifically Dr. Robert Trumbull, Dr. Michael Wiedenbeck and Frederic Couffignal for their hospitality, availability and instruction during SIMS analysis.

Lastly, I must thank my family, girlfriend and closest friends for their presence, support and motivation on a daily basis throughout the last months. Despite being apart from scientific matters, their influence was incredibly valuable.

Abstract

In southern Norway and Sweden, the Sveconorwegian orogenic belt hosts over 5000 pegmatite bodies (1100-900 Ma) usually clustered in local pegmatite fields. The Spro pegmatite, the object of this study, occurs, however, as an isolated body on the Nesodden peninsula approximately 20 km SSW of Oslo. Observations from fieldwork characterize the Spro pegmatite as a vertical dyke, approximately 230 m long, with variable thickness (1 to 25 m). The geological setting comprises the dyke emplaced in a tectonically complex region within a shear zone, transecting the Mesoproterozoic basement. The host rocks consist in deformed Spro granite (1542 -1493 Ma) and amphibole gneiss, both affected by amphibolite-facies metamorphism during the Sveconorwegian orogeny which peaked around 1050 Ma. Field observations and analyzed samples revealed that the otherwise homogenous pegmatite body exhibits late-stage, albite veins hosting an unusual mineral assemblage (including tourmaline, fluorite, topaz, and beryl) compared to other Sveconorwegian pegmatites. The Spro pegmatite particular features generated great interest regarding its relation to the shear zone, its unusual mineral assemblage and orogenic events that highly influenced the region's geology as well as the pegmatite genesis.

Interpretations based on the performed fieldwork and tectonic features indicate that the development of a major regional shear zone occurred almost simultaneously with the amphibolite facies metamorphism. The resulting intense deformation within and close to the shear zone is recognizable in the collected host rocks. The Spro pegmatite devoid of internal zonation was emplaced 1035 Ma along the fault. Recognized leucosomes in the region combined with analyzed mineral assemblages point to P-T conditions around 2-6 kbar and ~650 °C. The water circulation associated with the shear zone is assumed to have decreased the pegmatite protolith's melting temperature, and suggest lower crystallization temperatures (~400-600 °C). The geochemical signatures from whole rock analysis by solution ICP-MS indicate that the pegmatite protolith, not seen in the field, is a peraluminous (A/CNK and A/NK ratios of 1.8 and 2.10 respectively), anarogenic, A-type granitic rock, genetically unrelated to the host rocks. The Spro pegmatite mineral assemblage and geochemical data characterizes it as a member of the NYF petrogenetic pegmatite family and the muscovite-rare-element REE class with three distinct crystallization stages: 1) Primary stage of coarse-grained to megacrystic major minerals microline, muscovite, quartz and oligoclase-albite, and accessory monazite, thorite, samarskite-(Y), columbite-(Fe); 2) Late incompatible-element-enriched stage consisting in sugary albite irregular cross-cutting veins, hosting tourmaline, green muscovite, fluorite, topaz, beryl, microlite, apatite, and calcite; 3) Alteration stage with replacement of pre-existing minerals.

EMPA analyses of the Spro micas revealed a systematic increase in Fe, F, Rb, and Na. These concentrations and trends indicate that the initial Spro pegmatite melt was primitive in composition but consistently evolved during pegmatite crystallization from the wall to the core of the body. Micas associated with the late stage albite veins have the most evolved compositions. EMPA analyses of tourmalines occurring exclusively in the albite veins have a relatively homogeneous schorl composition (16.2 wt% FeO and 2.4 wt% Na2O) suggesting a fairly consistent composition of the albite zone forming melts. Additionally, the consistent δ11B values acquired by in-situ microanalysis of the tourmalines by SIMS, averaging −13.2 ‰, suggest a single B source. The B isotopic composition, typical for peraluminous crustal reworked rocks and silicate melts and evidence pointing to partial melting indicate that the pegmatite melt originated from shear zone induced anatexis of a B-rich protolith. Furthermore, the progressive crystallization trends, along with chemical and mineralogical consistency of albite zone veins indicate that these are a product of melt-melt immiscibility.

TABLE OF CONTENTS

The history, mineralogy and genesis of the Spro pegmatite mine, Nesodden

1. Introduction

Granitic pegmatites are well known for its distinctive enormous crystal size, complex internal fabrics and a great variety of accessory minerals. With concentrations and purity not found in any other geological environments (Glover *et al.,* 2012), pegmatites are major sources of rare metals, gemstones and industrial minerals (Linnen *et al.*, 2012). According to London and Kontak (2012), granitic pegmatites have been a focal point in petrology and mineralogy due to the rarity and diversity of its accessory minerals. The importance and value of the economic commodities hosted by pegmatites stimulated many of the past and ongoing studies. Recently, a dispute over pegmatite's genesis arose as the traditional model of its formation via fractionation of large granitic bodies has been challenged (e.g. Černý, 1991c). The possibility of pegmatites bodies forming without parental granite pluton sources, through the process of anatexis, opened the door to more studies (e.g. Müller *et al.*, 2015b).

The Sveconorwegian orogenic belt, which comprises most of southern Norway and Sweden, is home to one of the largest pegmatite clusters in the world, the Sveconorwegian pegmatite province (Müller *et al.,* 2015b). The province hosts over 5000 pegmatite bodies dating from 1.1 Ga to 900 Ma, which usually form pegmatite fields (Müller *et al.*, 2017). Contrary to most of the Sveconorwegian pegmatites, the Spro pegmatite, located on the west coast of the Nesodden peninsula, does not belong to a pegmatite field. Even more interestingly, it is one of the very few pegmatites in Norway that contains the boron silicate tourmaline as an accessory mineral.

The purpose of this investigative study is to reveal the origin and evolution of the Spro pegmatite in the context of the Sveconorwegian orogenesis. The specific aims of this master thesis are: 1) 2) to map the pegmatite body and its host rocks; 2) to compile and reassess mineralogical data of previous studies; 3) to characterize the diversity of the mineralogy and its paragenetic-sequential relationships; 4) to determine the chemistry of major and accessory minerals for the geochemical and mineralogical classification of the Spro pegmatite and to better understand conditions of pegmatite formation; and 5) to gather historical data on the pegmatite mining and the discussion of economic aspects of the pegmatite as a resource of industrial minerals.

To achieve this aims a wide spectrum of analytical methods have been applied including optical microscopy, SEM, EMPA and SIMS. Samples used in this study were gathered from the collection of the Natural History Museum and collected during fieldwork in the frame of this study. There is a focus on the mineralogical investigation of the boron silicate tourmaline, which, as previously mentioned is rarely found in Sveconorwegian pegmatites but relatively abundant in the Spro pegmatite.

2. Theoretical background

2.1 What are granitic pegmatites?

Pegmatites are complex, highly variable, coarse-grained, inhomogeneous intrusive igneous rocks. They generally have a granitic composition but are more defined by their textural characteristics than its composition and are arguably among the most complex rocks known on Earth (London, 2008). Minerals found in pegmatites can display extreme textural variations, especially in crystal size varying from millimeters to several meters, which is a determining characteristic. Within the granitic pegmatites, elements including Li, Be, Rb, Cs, Nb, Ta, Sn, the rare-earth elements, B, P, and F can become enriched to weight-percent levels, majorly through melt fractionation (London, 2008). Other determining characteristics include: the graphic texture due to the intergrowth of quartz and alkali feldspar which gave origin to the term "pegmatite" (London, 2008); extremely variable grain size, often smaller near the margins and larger at the center of pegmatite bodies, sharply bounded spatial zonation of mineral assemblages and prominence of skeletal crystal habits or graphic intergrowths (London, 2008). In addition, the disclosure of its origins is hampered by the fact that although their bulk compositions are similar to ordinary granitic igneous rock (usually composed of quartz, feldspar and mica), their minerals are commonly segregated into essentially mono-mineralic zones which, considered individually, can resemble hydrothermal veins and segregations (London, 2008).

Pegmatite bodies differ from typical plutonic bodies in a few ways. Most pegmatite bodies are small, with dimensions on the scale of meters rather than kilometers, and display internally complex fabrics compared to most plutonic bodies which are commonly mineralogically and texturally much more homogeneous (London and Kontak, 2012).

Pegmatites are known as sources of gems (Simmons *et al.* 2013), specialty metals (Linnen *et al.* 2012) and major industrial minerals which make it a host for exceptionally diverse range of economic commodities (London and Kontak, 2012). Explored minerals in pegmatite include feldspar, quartz, mica, lithium alumino-silicate minerals, spodumene, and kaolin as the chemical fractionation that produces pegmatites refines these minerals to a purity and dimensions that are not achieved in other geologic environments (Glover *et al.*, 2012). Most gem-bearing pegmatites are classified as miarolitic, which refer to the presence of clay-filled or open, crystal-lined cavities (London and Kontak, 2012). Pegmatites are the host for a large variety of gemstones that include varieties of beryl, topaz, tourmaline, and more than 50 less familiar gemstones (Simmons, 2003) but have also always been sought for minerals and metals that have special uses, as soon as the 1940s (London and Kontak, 2012). Some uses for minerals found in pegmatite include: sheet muscovite as grid separators in electronic vacuum tubes; quartz in the manufacture of glasses and ultrahigh pure quartz as a foundational material in the electronics industry; feldspar for ceramics and glass; beryllium as a component of copper alloys used mostly for bearings and gears; while others such as niobium, tantalum, tin, lithium, cesium, rare earths, and other normally rare elements are used for applications in electronics, nuclear energy, aerospace, deep drilling, and other specialized industries (London and Kontak, 2012). Often the sources of these and many other minerals with extensive uses and applications in various industries, pegmatites have a behind the scenes influence in economies and populations daily lives.

2.2 Pegmatite structure

Pegmatite intrusions, similar to other igneous bodies, occur as dikes, sills or pods in other igneous or metamorphic hosts forming segregations commonly as sharply bounded masses (London, 2008). The attitude (dip) of pegmatite bodies is commonly taken as being close to the original orientation of consolidation because most pegmatite-forming events are anorogenic or occur at the waning stages of tectonic events (London, 2008). Pegmatite pods lack planar continuity and form lenticular or bulbous shapes, these occur in schistose metamorphic host-rocks (London, 2008). Formation of miarolitic cavities and gem-quality crystals can occur through decompression, fractional crystallization and depletion of B, Li, F, and P (Simmons *et al.*, 2013)

Zoning or the lack of it provides the starting point for the description of the internal anatomy. Unzoned pegmatites display homogeneity in grain size and mineralogy though they may present a porphyritic texture and oriented fabrics. Unzoned pegmatites tend to occur in association with host rocks of high metamorphic grade (London, 2008). However, the majority of pegmatites exhibit distinct zoning, which is manifested by variations in the spatial distribution of grain size, mineral assemblage, crystal habit, or rock fabric (London, 2008). It is the zoning which is largely what distinguishes pegmatites from other ordinary plutonic igneous rocks. The zoned pegmatite bodies contain the following distinguishable sections: border zone, wall zone, intermediate zones and core.

The thin (few centimeters) *border zone* completely surrounds the pegmatite in contact with its host rocks. The grain size is fine (~2- 5 mm), and the texture can be granitic or bimodal if the fine-grained portion constitutes a groundmass to larger (~1-3 cm) crystals. Unlike other igneous rocks, the border zones of pegmatites do not represent the bulk composition of the pegmatite in which they form (London, 2008).

Where present, the *wall zone* of most pegmatites has thickness to approximately 1 meter, and represents a coarser-grained (-1 - 3 cm) variant of the border zone, thus displaying similar mineralogy (London, 2014). The anisotropic orientation of inwardly flaring minerals including tourmaline, beryl, micas, and feldspars commonly appears first in the wall zone (London, 2008). Per London (2014), k-feldspar and quartz form branching skeletal crystals and graphic intergrowths while micas grow as thin blades towards the pegmatite core.

The *intermediate zone* is characterized by a sharp grain size increase and is commonly dominated by a single mineral phase, usually microcline, plagioclase, quartz, spodumene, petalite or montebrasite (London, 2008; 2014). It may be symmetrically, asymmetrically distributed throughout the pegmatite body or may also be discontinuous while being predominantly developed in the thickest portions of the pegmatite and disappears as the pegmatite thins (London, 2008; 2014).

The *core* is the innermost part of the pegmatite and can display a single mass or the mineralogy found throughout the body (London, 2008). It can have variable dimensions compared to the other zones and are typically characterized by monominerallic quartz (London, 2014).

Pegmatites can also display fracture fillings (usually quartz) that infiltrate through fractures or replacement bodies.

The *Replacement zones/bodies* consist in sections of the pegmatite body where the original pegmatite was converted into a different (typically fine-grained) mineral or mineral assemblage (London, 2008). Pseudomorphism, which is defined by distinguishable morphologic features of crystals in the original mass despite complete alteration is an unequivocal indication of replacement zones (London, 2008). In petrographic thin sections, textural features of the host phase, such as cleavage, twinning among others, may be preserved in the pseudomorphic assemblage while replacement is highly selective as some mineral may be completely replaced and other entirely preserved (London, 2008). The hydrothermal replacement is commonly regarded as responsible for high concentrations of exotic minerals or monomineralic masses of common minerals as their compositions lie so far from that of a feasible igneous (granitic) composition (London, 2008).

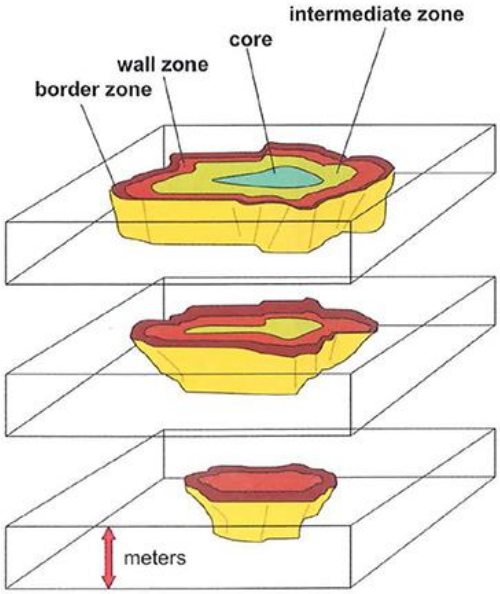

Fig 1. Pegmatite zoning diagram (modified from Cameron *et al*., 1949) (London, 2008).

2.3 Classification of granitic pegmatites

Pegmatites' high mineralogical, geochemical and textural variability and economic importance led to various classification attempts. The currently most applied scheme is the classification by Černý and Ercit (2005). This classification distinguishes five pegmatite classes, ten subclasses, thirteen types, and seven subtypes illustrated in Table 1. According to Černý & Ercit (2005), the five pegmatite classes governed by the pressure-temperature conditions are: Abyssal, Muscovite, Muscovite–Rare-Element, Rare-Element, and Miarolitic pegmatites. The division into classes is based on genetic criteria, such as the temperature-pressure conditions during emplacement depth of pegmatite melts. Within individual classes, the subdivision into subclasses follows geochemical characteristics. The third level of the classification, the pegmatite types is based on mineral assemblages. Recently the classification of Černý and Ercit (2005) has received a lot of critics because the crystallization pressure of pegmatites is hard to determine and, thus, the classification is difficult to apply (e.g. Müller *et al.*, 2015b).

Parallel to the pegmatite class classification, Černý (1991a) introduced the pegmatite family classification that corresponds to the most distinctive enrichment of elements produced by fractionation within chemically distinct pegmatite groups (London, 2008). The three families are: the NYF family with progressive accumulation of Nb, Y and F, a characteristic suite of elements in the granites that are normally labeled as A-type (anorogenic in origin: Collins *et al.* 1982) or "within plate" granites (Pearce *et al.*, 1984; London, 2008); the peraluminous LCT family marked by prominent accumulation of Li, Cs and Ta a characteristic enrichment found mostly, but perhaps not exclusively, in S-type granites (Chappell and White 1992, 2001) that originate from metasedimentary rocks rich in muscovite (London 1995, 2008); and the mixed NYF + LCT family of diverse origins, such as contamination of NYF plutons by digestion of undepleted supracrustal rocks (Černý and Ercit, 2005).

Table 1. Adapted pegmatite classification from Cerný and Ercit (2005) (Cerný *et al.*, 2012). The table provides a simplified version of the complex pegmatite classification into Classes and Type and petrogenetic Family.

Class	Subclass	Type	Subtype	Family
Abyssal	HREE			NYF
	LREE			
	U			NYF
	BBe			LCT
Muscovite				
Muscovite–rare element	REE			NYF
	Li			LCT
Rare element	REE	allanite–monazite		NYF
		euxenite		
		gadolinite		
	Li	beryl	beryl–columbite	LCT
			beryl–columbite–phosphate	
		complex	spodumene	
			petalite	
			lepidolite	
			elbaite	
			amblygonite	
		albite–spodumene		
		albite		
Miarolitic	REE	topaz–beryl		NYF
		gadolinite–fergusonite		
	Li	beryl–topaz		LCT
		spodumene		
		petalite		
		lepidolite		

The minor and accessory mineralogy of pegmatites is mainly controlled by the original melt composition and the fractionation degree of the pegmatite melt thus the LTC and NYF families are chemically related to specific granite types.

LCT pegmatites

The LCT pegmatites are chemically related to S-type granites and have as most prevalent characteristic the enrichment in the rare elements Li, Ce and Ta, This enrichment is expressed by assemblages that include muscovite, garnet, cordierite, sillimanite or andalusite, tourmaline, gahnite and lithium-bearing minerals such as lepidolite, spodumene, amblygonite (Černý *et al.*, 2012). These granites stem from the anatexis of mica-rich metamorphic schists and aluminous gneisses of sedimentary origin which arise from crustal thickening usually associated with subduction and continental collision. Despite lacking the foliation or pervasive deformation, these settings are expected in syntectonic environments (Černý *et al.*, 2012). Many of the LCT pegmatites contain a great variety of primary and secondary phosphates in addition to apatite, with phosphorus as a significant component of the feldspars (London et al., 1995).

NYF pegmatites

The NYF pegmatites with chemical characteristics typical for A-type granites contain chemically complex oxides and silicates that carry heavy rare-earth elements (HREEs), Ti, U, Th, and Nb > Ta among others (Černý *et al.*, 2012). Abundant fluorite or topaz reflects the enrichment in F, while mafic minerals include ferruginous biotite, aegirine, and riebeckite, the latter two denoting peralkaline compositions for these pegmatites (Černý *et al.*, 2012). Most of the NYF pegmatites (e.g. beryl-topaz ; allanite–monazite) bear a chemical affinity to A-type granites (Eby 1990; Černý and Ercit 2005; Martin and De Vito 2005). These granites are sourced from combinations of pyroxene-bearing quartz-feldspathic rocks of the lower continental crust with varying amounts of added mantle components (London, 2008). The magmas are believed to be H_2O-poor and in some instances, may be entirely mantle-derived (e.g. Haapala *et al.*, 2007). Where their tectonic setting can be determined, NYF pegmatites are usually associated with hot spots or rift zones within continents (Černý *et al.*, 2012). Martin and De Vito (2005) state that NYF pegmatites carry the same trace element enrichment patterns of peralkaline igneous rocks that fractionate directly from mantle sources.

2.4 Genesis of granitic pegmatites

Magmatic versus Anatectic origin

Magmatic Origin

According to the classical opinion, the majority of granitic pegmatites is generally acknowledged to form by fractional crystallization of a larger batch of granitic melt (pluton) (Černý, 1991b, c; London, 2008; Černý *et al.*, 2012). The process is usually characterized by cooling and consequent crystallization of magma bodies where two scenarios may take place: As the magma body starts to cool, magma differentiation can take place through fractionation where parts of the melt cool and crystallize while others may become enriched of certain elements that are left “concentrated”; or during the cooling process the body can be “percolated” by exotic fluids (usually volatiles) that by integrating the magmatic body concentrate and generate rare minerals. The resulting pegmatites are considered as granite-related pegmatites or magmatic pegmatites. The classical and most accepted pegmatite formation from a parental pluton is illustrated in Fig 2.

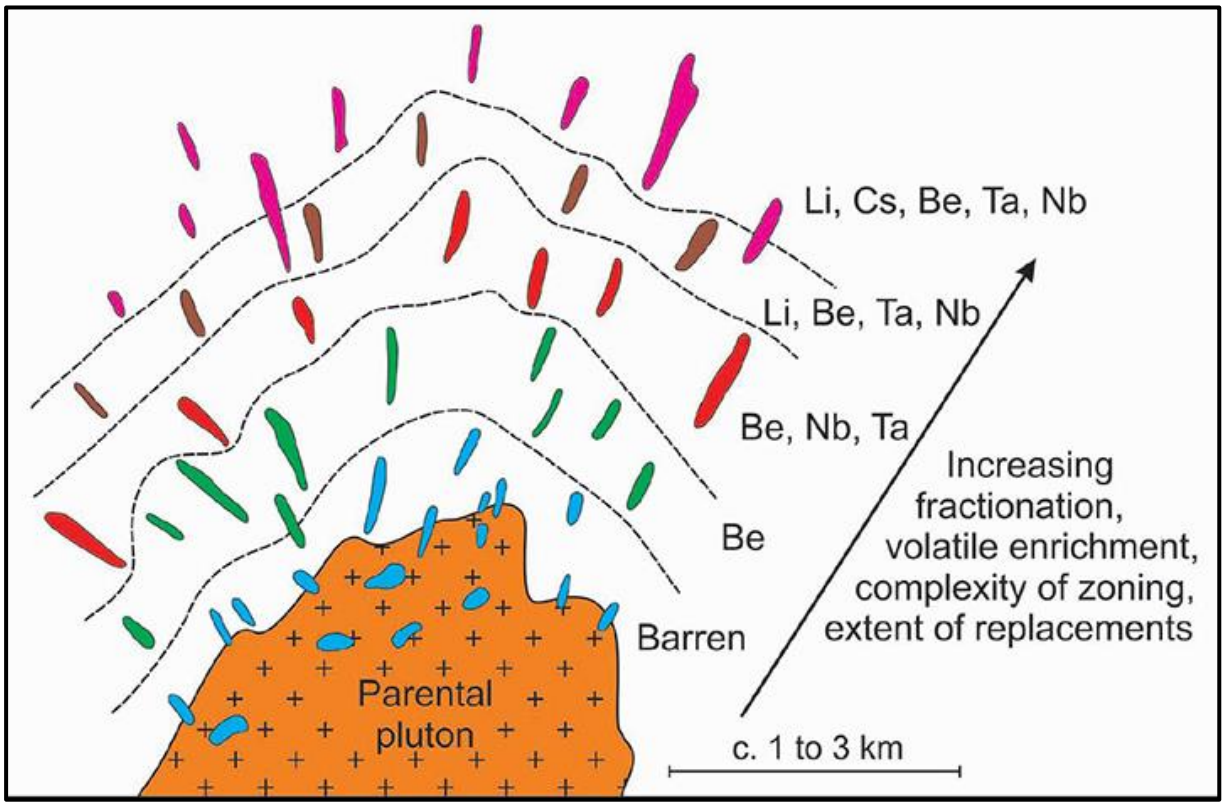

Fig 2. Fractionation trend from parental pluton source to barren and to evolved pegmatites modified from Černý, (1991b) (Müller *et al.*, 2017). The figure illustrates the ideal fractionation trend of a crystallizing primitive parental pluton, with consequent enrichment into various, more evolved pegmatite bodies.

Anatectic origin

The second genetic type of pegmatites, the anatectic pegmatites, is based on the assumption that a pegmatitic melt can form by direct anatexis of rocks (Simmons and Webber, 2008). This process is characterized by the low-degree partial melting of crustal or mantle rocks, resulting in redistribution and enrichment of certain elements as well as formation of new ones which prefer to enter the leucocratic melt (London, 2008). In collisional tectonic environments, a sedimentary sequence (including volcanic rocks) can contain fluxing components and incompatible elements such as B and Li. With partial melting, those fluxing components, incompatible elements and minerals of granitic character will be preferentially partitioned into a low-degree partial melt. This melt can subsequently fractionally crystallize to form a pegmatitic melt (Simmons and Webber, 2008).

Pegmatite bodies commonly form clusters or swarms called pegmatites fields. Pegmatites bodies are commonly near a granite pluton, which traditionally has been considered as the parental pluton of the pegmatites. Most of the Sveconoregian pegmatites in southern Norway are concentrated in fields adjacent to granite plutons (e.g. Froland, Evje-Iveland, Tørdal) suggesting a genetic relationship. However, recent dating of pegmatites and adjacent granite plutons revealed that there are large age differences (>40 Ma) between both, indicating that they are not genetically linked to each other (Müller *et al.*, 2015b, 2017). The Spro pegmatite that is described in this study does not belong to a pegmatite field and is the only pegmatite found in a 30-kilometer radius (Müller *et al.*, 2017). This unusual setting makes the Spro pegmatite genesis disclosure one of the main objectives of this study.

2.5 Mineralogy of granitic pegmatites with special emphasis on tourmaline

The mineralogy of granitic pegmatites is rich, diverse, complex and generally controlled by the fractionation degree of the pegmatite melt. The main minerals found are feldspar (dominant) in both plagioclase and K-feldspar, quartz and mica giving a "granitic character" that resembles common granites. Most pegmatites are mineralogical simple rocks, consisting of approximately 65% feldspar and 25% quartz, along with 5–10% mica and about 5% of other accessory minerals (e.g. garnet, tourmaline, spodumene, oxides, etc.). Though broadly similar in their mineralogy, each pegmatite has its own distinctive attributes, such as crystal size variations, mineral distribution (homogeneous or zoned), feldspar composition, and accessory mineral assemblage (Glover *et al.*, 2012).

Garnet, magnetite and monazite are common accessory minerals with possible occurrence of more exotic ones such as: spodumene, petalite, phosphates, tourmaline and possibly other borates and borosilicates, topaz, beryl, niobium, tantalum, uranium oxides, pollucite, zircon and possibly other zirconoslicates, pyroxene, amphibole, zeolites, carbonates, sulfides and clays. The growth of the referred minerals depends on the availability of incompatible elements. London (2008) states that such great diversity and complexity, as well as giant crystal samples make the study of the mineralogy and respective evolution very challenging. According to Černý *et al.* (2012) pegmatites accentuate the trace element signatures of their granitic sources. That signature is usually used to determine the origin of pegmatites from granites with distinctive characteristics. Possible composition alterations from host rocks interaction are limited by the rapid cooling and low heat content of pegmatite-forming magmas (Černý *et al.*, 2012).

The studied Spro pegmatite is one of the few pegmatites in Norway containing tourmaline (Raade, 1965) and, thus, more detailed information and studies about tourmalines are presented in this study. Tourmaline is a relatively rare mineral in Norway due to the general low B content of the crystalline Archean, Svecofennian and Sveconorwegian basement exposed on Norwegian territory (Larsen *et al.*, 1999). Tourmaline is a crystalline, chemically complex, B-rich trigonal silicate mineral that belongs to the cylosilicate group (ring silicates) (Bosi, 2018). It is often used as a gemstone and can display a wide range of colours directly influenced by its varied chemical composition.

Tourmalines occur in most granitic intrusions as an accessory mineral but in some cases also as a rock-forming mineral and provide a record of the late-magmatic stage and, in places, the transition to hydrothermal conditions (Müller *et al.*, 2006). It commonly forms with the interaction between crustal rocks and migrating hydrous fluids or silicate melts, and its isotopic composition provides a reliable record of the isotopic composition of the fluids and melts from which it crystallized (Marshall and Jiang, 2011). Fractionation the forming melt may lead to the enrichment of tourmaline in the tourmaline-rich intrusion (Müller *et al.*, 2006). Tourmaline's colours have many different causes although it is generally agreed that traces of iron, and possibly titanium, induce green and blue colours, manganese produces reds, pinks, and possibly yellows while some pink and yellow elbaites might be caused by radiation (GIA, 2018). It is the most multi-coloured mineral type known, occurring in virtually every colour of the spectrum (minerals.net, 2018). The major characteristics of tourmalines can be found in Fig 3.

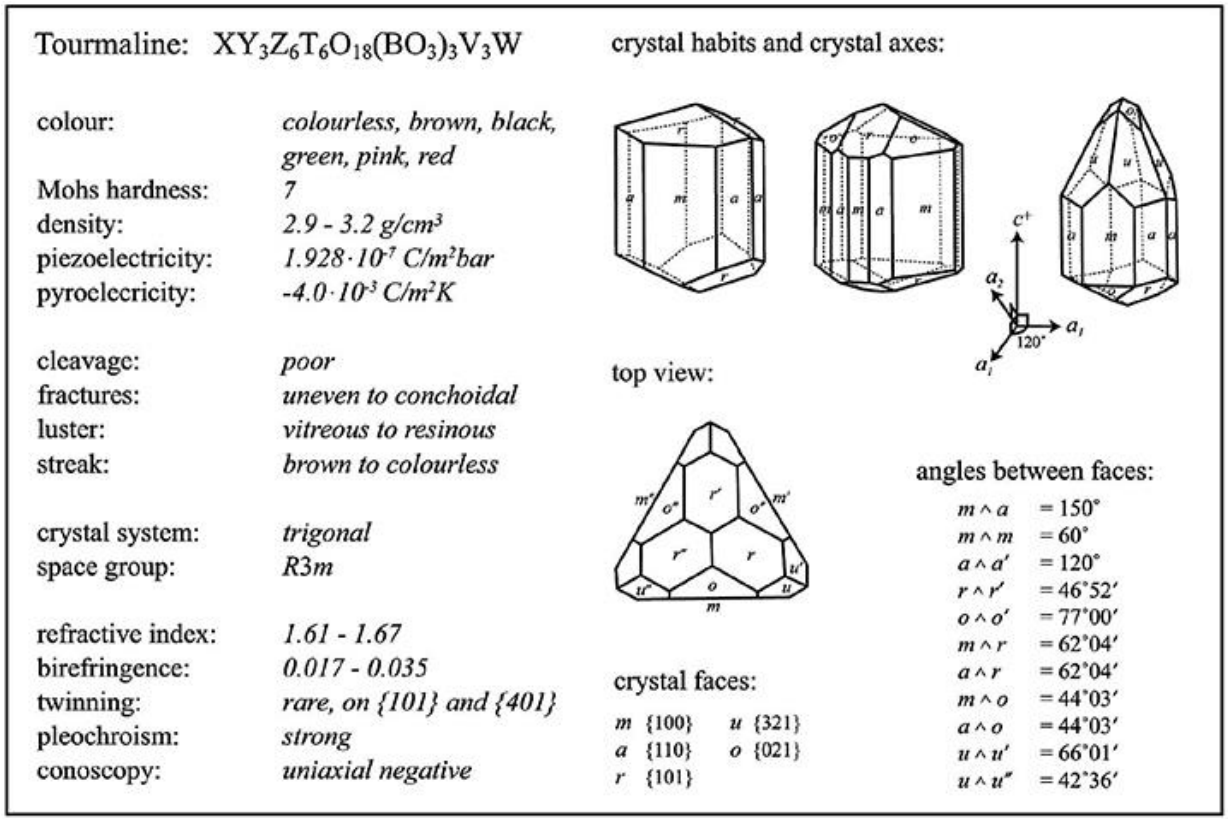

Fig 3. Tourmaline major features and characteristics (Hinsberg *et al.*, 2011).

Minerals of the tourmaline supergroup are exceptionally variable and complex in their chemical composition. These compositions allow us to extract a broad range of isotopic information from a single mineral and present a vast geochemical recorder that is unparalleled among minerals (Marshall and Jiang, 2011). Hawthorne and Henry (1999) indicate that the chemical formula of tourmaline may be written as $XY_3Z_6(T_6O_{18})(BO_3)_3V_3W$, which has the advantage of the generality that results and represents the sites within the asymmetric unit of the structure, and makes no assumptions as to the occupancy of sites apart from those occupied by O^{2-}. Ignoring trace constituents, the letter symbols of the general formula can be assigned as follows:

Table 2. Site preference of elements in the tourmaline group (Henry *et al.*, 2011).

X-site	Ca, Na, K, □ [vacancy]
Y-site	Li^{1+}, Mg^{2+}, $Fe^{3+,}$ $Mn^{2+,}$ Al^{3+}, Cr^{3+}, V^{3+}, Fe^{3+}, Ti^{4+}
Z-site	Mg^{2+}, Al^{3+}, Fe^{3+}, Cr^{3+}
T-site	Si^{4+}, Al^{3+}, B^{3+}
B-site	B^{3+}, □ [vacancy]
V-site	OH^{1-}, O^{2-}
W-site	OH^{1-}, F^{1-}, O^{2-}

The X-site

The X-site typically hosts larger cations such as Na (and K), Ca or □, and basic classification of tourmaline based on X-site occupancy is shown in Fig 4. According to Hawthorne and Henry (1999), the three main tourmaline groups are the Calcic group, the Vacancy group and the Alkali group which can then be classified into subgroups related by heterovalent coupled substitutions.

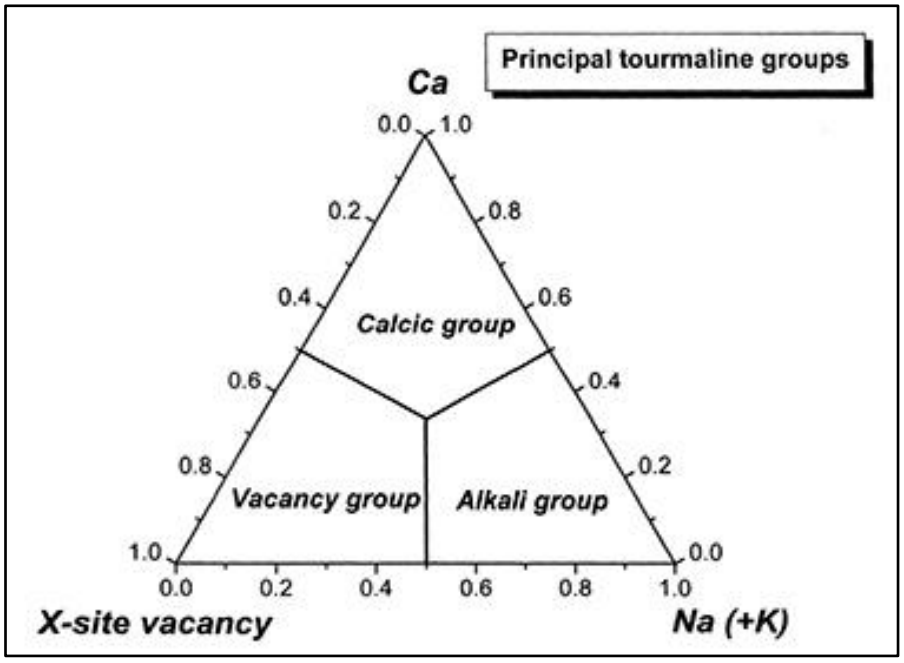

Fig 4. Major compositional groups of tourmaline minerals (Hawthorne and Henry, 1999).

Due to the highly variable and complex Tourmaline group chemistry, many more end-members were discovered after those considered valid by Hawthorne and Henry (1999). Tourmaline's chemical composition and crystal structure are used to define its species and the major groups are elbaite (most common), liddicoatite, dravite, uvite, and schorl (GIA, 2018). The tourmalines found in the Spro pegmatite being analysed in this study belong to the Schrol group. Schorl is typically black and iron-rich variety that is rarely used as a gem.

According to Henry *et al.*, (2011) most chemical variability occurs at the X, Y, Z, W and V sites and these are commonly occupied as shown in table 2.

Hawthorne and Henry (1999) suggested the following procedure for systematical naming of tourmaline according to analytical data and knowledge of probable site occupancies:
1) Consider the dominant X-site species to establish the principal tourmaline group.
2) Establish the dominant anion (OH-, F or O_2) at the W-site, assuming that F occurs exclusively at the W-site.
3) Estimate the dominant anion (OH or O_2) at the V-site. The current state of knowledge is that most tourmalines are dominated by OH at the V-site.
4) Determine the dominant F-cation configuration (Mg, Fe^{2+} or Li). Each of the principal groups has three possible W anions.
5) Establish the dominant Z-site cation (Al, Cr^{3+} or Fe^{3+}).

As mentioned above, tourmaline is the dominant mineral host for boron in most crustal rocks, around 3 wt% B in tourmaline according to Trumbull and Slack, 2018. It is a chemically resistant detrital phase in sediments and a common gangue mineral in a wide range of hydrothermal ore deposits (Trumbull *et al.*, 2008). According to Dutrow and Henry (2011), due to its complex and variable chemistry along with low diffusivities, the complete evolution of tourmalines may be encapsulated in a single grain. The structure's ability to adjust in composition according to changing chemical environments and *T–P* conditions allow tourmalines to have an extensive *T–P* stability range. As shown in Fig 5, it covers most of the conditions found in the Earth's crust, and be in equilibrium with a wide range of geologic fluids (Dutrow and Henry, 2011).

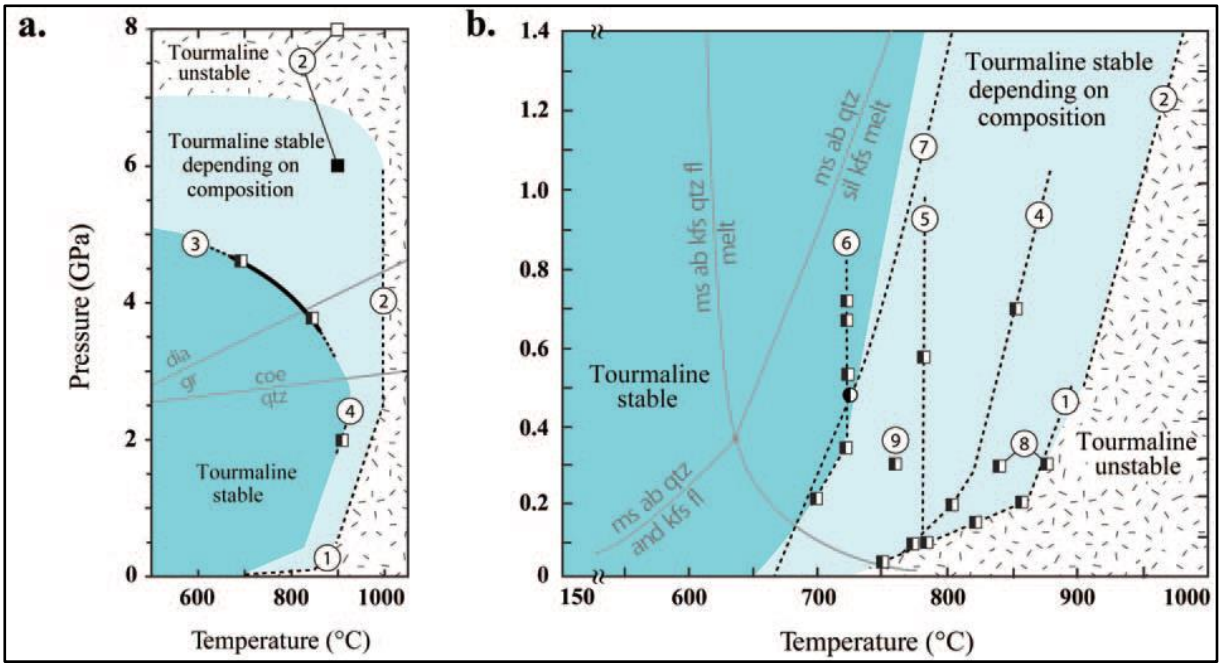

Fig 5. Toumaline stability fields (Dutrow and Henry, 2011). A) Displays the tourmaline stability field over a wide range of P-T conditions; B) Displays a narrower range.

The resultant preserved information on temperatures, pressures, and fluid compositions provide insight into the history of the melt or fluid in which the tourmaline developed (Dutrow and Henry, 2011). Tourmaline is therefore at the center of interest in B-isotope geochemistry as it can grow in both late-magmatic and hydrothermal conditions, which is also analysed in this study. Its zoning provides evidence of changing geochemical conditions and works as an indirect recorder of fluid compositions (Trumbull and Slack, 2018).

The tourmaline B isotope analysis is most commonly performed through Secondary Mass Ion Spectrometry (see Section 3.6). Trumbull *et al.* (2008) indicate that in-situ microanalysis of boron-isotope composition in tourmaline by SIMS has two main advantages over bulk techniques: it avoids mineral inclusions contamination and can resolve variations in isotope ratios at the sub-grain scale. This allows direct coupling of isotopic and chemical composition with important petrographic features such as mineral zoning, replacement or overgrowth textures (Trumbull *et al.*, 2008).

Boron

Boron is known or inferred to be an important component in many peraluminous silicic-magmas that form granites, pegmatites, and rhyolites (Wolf and London, 1997) while primary disseminated tourmaline may indicate the presence of B in magmas. Boron mineralization is commonly more abundant along the margins of intrusive rocks, where mixing between two reservoirs, B from magma, and ferro-magnesian components from wall-rocks produce abundant tourmaline (London *et al.*, 1995). Where granites or pegmatites and their host rocks are well exposed, much of the boron originally present in the magmas is not conserved within the igneous bodies majorly due to devolatilization/dehydration reactions (Morgan and London, 1987, 1989), which hampers the assessment of the melt's boron content (Wolf and London, 1997).

According to Trumbull and Slack, (2018), B is an incompatible lithophile element that is concentrated in the continental crust relative to the mantle for two reasons: 1) the Earth's crust significant built of intermediate-composition to felsic igneous rocks as B preferentially

partitions into granitic melts, where it tends to remain and become concentrated during magma ascent, emplacement, and crystallization; 2) boron is a volatile element, easily diffused by hydrous fluids, which are prevalent on continents. Also according to Trumbull and Slack, (2018), B is generally prone to loss during dehydration reactions, and metamorphic fluid preferentially removes the heavier isotope. This leads to an overall low concentration of B in granulite-facies rocks (ca. 2 μg/g B) but the growth of B-hosting minerals such as tourmaline can revert these effects (Trumbull and Slack, 2018). The preservation of high B contents is then dependent on the early and/or abundant crystallization of B-hosting minerals (e.g. tourmaline) which will preserve/retain B, avoiding its escape even during metamorphic conditions (Trumbull and Slack, 2018).

Per Kowalski and Wunder (2018), boron's isotopes act as geochemical tracers of any vapor-, liquid- or melt-mediated process in the Earth's interior thus its studies for constraining fluid provenance and recognizing fluid sources. There are two stable B isotopes, ^{11}B and ^{10}B, with the prior and heavier being the most abundant (~80%) (Meyer *et al.* (2008).

A critical factor in tourmalines B isotopic composition studies is the coordination, as heavier ^{11}B tend to have trigonal coordination and lighter ^{10}B tens to have tetrahedral coordination (e.g. Trumbull, 2008). Because of the expected fractionation of ^{11}B and ^{10}B (e.g. between aqueous fluid and granitic melt) (Hervig *et al.*, 2002), the B-isotopic composition of tourmaline can help understand the nature of the fluid(s) from which it formed (Trumbull, 2008).

2.6 Regional geology of study area

Sveconorwegian orogeny (in general)

The Sveconorwegian orogenic belt forms major parts of southern Norway and Sweden and is part of the Grenville orogeny resultant of the continent-continent collision between Baltica, Amazonia and Laurentia (Bingen *et al.*, 2008a). The intensity of Sveconorwegian reworking in cluding deformation and metamorphism of previous units as well as intrusion by several generations of magmatic rocks increases from north to south and from east to west (Johansson *et al.*, 1991; Söderlund *et al.*, 1999). The orogeny dates from the end of the Mesoproterozoic (1140 Ma) to the middle of the Neoproterozoic (900 Ma) (Bingen *et al.*, 2008b). The Sveconorwegian orogeny represents the easternmost part of the main Greenville orogenic belt, which extended over at least 10,000 km. The main Greenville belt is defined by zones of continent-continent collision, accretion, and reamalgamation of fragmented and attenuated crustal blocks that eventually resulted in the assembly of the Rodinia supercontinent (Müller *et al.*, 2017). Widespread high-grade metamorphism, partial melting, and deformation of the Fennoscandian crust resulted from the Sveconorwegian orogeny. The process took place over several phases (illustrated in Fig. 6) including the Arendal, Agder, Falkenberg, and Dalane phases (Bingen *et al.*, 2006, 2008a; Müller *et al.*, 2017).

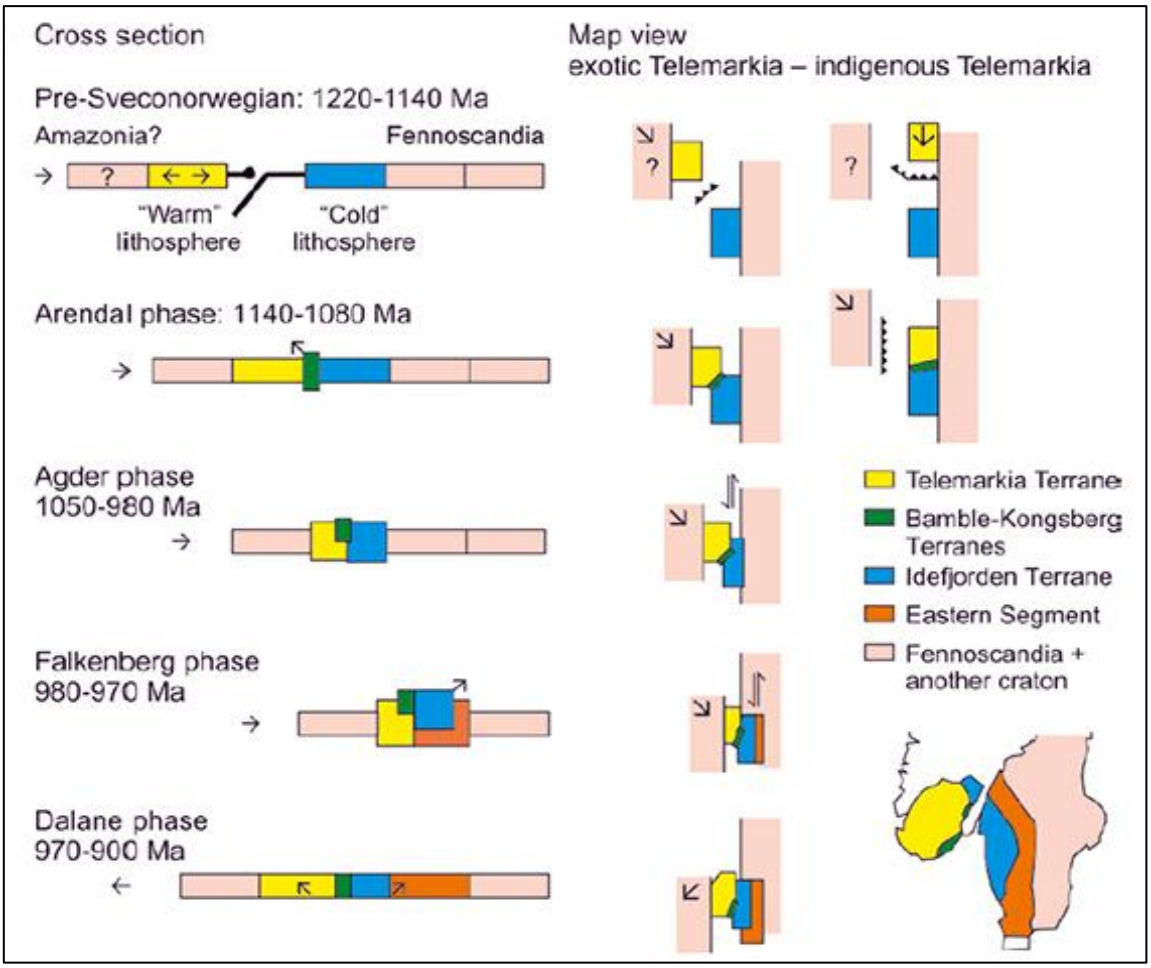

Fig 6. Sveconorwegian orogeny evolution model (Bingen *et al.*, 2008a). The figure illustrates the different phases that gave origin to the various terranes found on the Sveconorwegian orogenic belt.

The Sveconorwegian belt is divided into five main lithotectonic units separated by nearly N-S trending crustal scale shear zones: Telemarkia terrane, Bamble terrane, Kongsberg terrane, Idefjorden terrane and Eastern Segment (Bingen *et al.*, 2008a). In the following the five units are briefly described (in the order from east to west) in respect to the lithology and genesis.

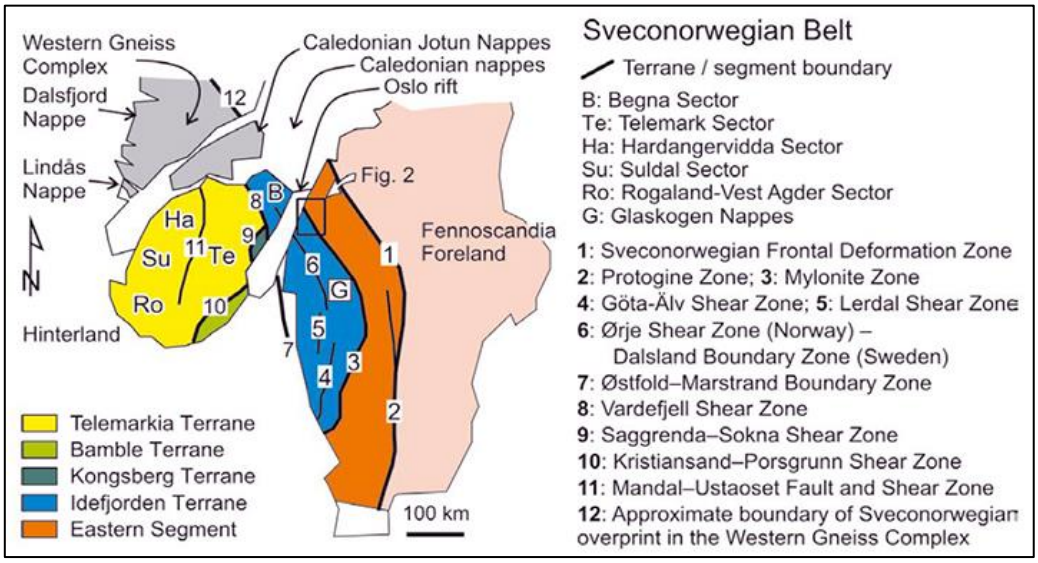

Fig 7. Southern Scandinavia: Sveconorwegian main lithotectonic units and shear zones (Bingen *et al.*, 2008a).

The Eastern Segment is dominated by variably gneissic granitoids (1800-1640 Ma) of similar composition to rocks of the TIB (Möller *et al.,* 2007). These are intruded smaller magmatic suites, mainly mafic dykes (1560 Ma), granite dykes (1460-1380 Ma), plutons and granite plutons (1250-1200 Ma) (Bingen *et al.*, 2008).

The Idefjorden Terrane consists of mainly calc-alkaline and tholeiitic plutonic and volcanic rocks (1660-1520 Ma), associated with greywacke-bearing metasedimentary sequences (Bingen *et al.,* 2001; Åhäll & Connelly 2008). Lithologies indicate younger units towards the west. It contains several amphibolite-facies orogen-parallel shear zones, including the Ørje Shear Zone (Norway) or Dalsland Boundary Zone (Sweden) and the Göta Älv Shear Zone (Park *et al.,* 1991), as well as a nappe complex, the Glaskogen Nappes (Lindh *et al.*, 1998). The grade of Sveconorwegian metamorphism is variable and ranges from green-schist facies to amphibolite-facies and locally granulite-facies (Bingen *et al.*, 2008a). The studied Spro pegmatite is located at the peninsula of Nesodden which is commonly regarded as part of the Idefjorden Terrane.

The Bamble and Kongsberg Terranes, which represent probably the same terrane, consist of mainly calc-alkaline, plutonic suites (1570-1460 Ma) associated with quartzite or greywacke-dominated metasediment complexes (Andersen *et al.,* 2004). The quartzite-rich complexes have a characteristic assemblage of quartzite, mica gneiss, sillimanite-rich gneiss and minor orthoamphibole-cordierite rocks. The Kongsberg Terrane hosts a suite of mafic plutons (1200 Ma) (Munz *et al.*, 1994). The Bamble Terrane hosts the gabbro-tonalite Tromøy complex (1200-1180 Ma), granitecharnockite metaplutons (1170-1150 Ma), pegmatites (1060 Ma) and post-collisional granite plutons (990-920 Ma) (Bingen *et al.*, 2008a).

The Telemarkia Terrane is characterized by a voluminous magmatic event (1520-1480 Ma) (Bingen *et al.*, 2005), the Telemarkian event (Bingen *et al.*, 2008a). There aren't any older magmatic rocks positively identified. The volcanic and plutonic suites (1520-1480 Ma) have a poorly defined geochemical signature. They are interlayered with and overlain by quartzite-bearing metasedimentary sequences older than 1350 Ma (Dons 1960; Bingen *et al.*, 2001a; Laajoki *et al.,* 2002; Andersen & Laajoki 2003; Corfu & Laajoki 2008). These rocks were intruded and unconformably overlain by several magmatic suites and sediments (between 1280 and 1130 Ma) (Bingen *et al.*, 2008a).

Sveconorwegian Pegmatites

The Sveconorwegian pegmatite province, to which the Spro pegmatites belongs, is part of the Sveconorwegian (Grenvillian) orogen and covers most of southern Norway and parts of southwestern Sweden. This includes the pegmatite districts (from west to east) of Hardanger, Mandal, Setesdal, Bamble, Nissedal, Buskerud, and Østfold-Halland to which the Spro pegmatite belongs (Müller *et al.,* 2015a). The province hosts more than 5000 pegmatite bodies (commonly aggregated in pegmatite fields) and represents one of the largest pegmatite clusters in the world dating from 1.1 Ga to 900 Ma (Müller *et al.*, 2017). Available data (although limited) indicate that pegmatite formation within the Sveconorwegian orogen falls into several distinct age groups of contrasting regional distribution and to some extent of poorly known relation to regional tectono-metamorphic events (Müller *et a*l., 2015b). The pegmatite formation occurs within four distinct periods in respective domains of the Sveconorwegian belt: (I) 1094-1060 Ma in the Bamble Sector, (II) 1041-1030 Ma in the Idefjord Terrane, (III) 992-984 Ma in the Idefjord Terrane and Rogaland- Hardangervidda-Telemark Sector, and (IV) 922-901 Ma in the Rogaland-Hardangervidda-Telemark and Bamble Sectors (Muller *et al.*, 2017a).

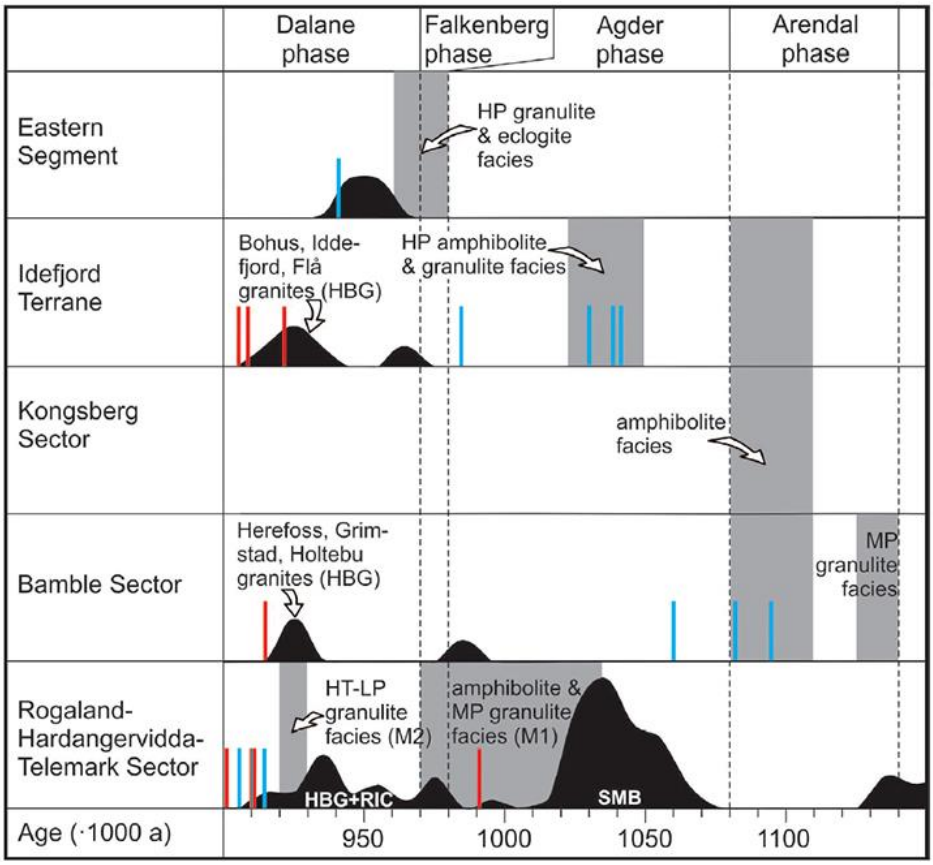

Fig 8. Diagram for the high-grade metamorphic and magmatic events of the Sveconorwegian orogen five lithotectonic sectors. Metamorphic and magmatic events displayed as black curves, pegmatite ages shown as red (data from Müller *et al.*, 2017) and blue (previous literature data) lines. Modified from Bingen *et al.* (2008a).

2.7 Previous studies and the mining history of the Spro pegmatite

Previous studies and investigations of the Spro pegmatite comprise an article by Raade (1965) and reports by the Geologisk Museums Venner (1991a-b, 1993 a-b) as the locality was frequently used for field trips and additional minerals were discovered occasionally.

The mineralogy of the granitic pegmatite at Spro is thoroughly described by Raade (1965) along with a brief characterization of the Spro area. The minerals present in the area are given in Table 3. Raade (1965) indicated that the pegmatite body consisted in two phases regarding its paragenesis: a primordial phase comprising microline, quartz, coarse to megacrystic albite, silver-grey muscovite, monazite, thorite, samarskite, columbite and possibly beryl; and a younger phase that includes fine-grained albite, quartz, green muscovite, black tourmaline (schorl), topaz, microlite, apatite, calcite and fluorite. In addition, it is stated that the 230-meter long pegmatite strikes N-S and is surrounded by a varied Precambrian leptite migmatite.

During various field trips and excursions to the Spro area between 1981 and 1988, different minerals were found and described. In May 1981, Raade found a sample containing bertrandite (NHM X-ray film no. 25795) which wasn't seen in this site on previous visits (GMV 1991a). The bertrandite specimen was described as a porous aggregate of white, plate-shaped crystals (<1 mm long) in micro cavities in samples comprised of microline, albite, quartz, green muscovite, fluorspar, tourmaline and microlite. In May 1982, alvite, which is a metamict, often Hf-rich variety of zircon, was first found at the Spro pegmatite by Eivind Heder (GMV 1991b). The mineral was described as thin prisms, up to 7 mm long, in the form

of a radial aggregate and displaying zoning with a brown glassy interior, but with a grey, lusterless outer zone. The mineral is also associated with violet fluorite and yellow-green muscovite embedded quartz and sugary albite.In April, 1983 anatase was identified for the first time (NHM X-ray film no. 26737) (GMV, 1993a). The anatase forms a small yellow-brown, dense mass, presumably a pseudomorphic alteration product of yttrian titanite, a variety of titanite.

Bastnäsite, hydrocerussite and galena were also discovered during excursions to Spro (GMV, 1993b). Fine-grained yellowish bastnäsite was found in 1986 (NHM X-ray film no. 27399) as aggregates of lath-shaped crystals, probably formed at the expense of allanite. Hydrocerussite (NHM X-ray film no. 28108) occurs as a white coating on galena and was found during an excursion of the Steinklubben Society in June 1988. As previously mentioned, the complete mineralogical inventory adapted from MINDAT (2018) and Raade (1965) is given in Table 3.

Table 3. Major and accessory minerals found in the Spro pegmatite (adapted from MINDAT, 2018).

Albite	xxx	Malachite	x
Anatase	x	Microcline	xxx
Apatite	x	Microlite Group	x
Bastnäsite	x	Molybdenite	x
Bertrandite	x	Monazite	x
Beryl	xx	Muscovite	xxx
Calcite	xx	Pyrite	x
Chalcopyrite	x	Quartz	xxx
Columbite-(Fe)-Columbite-(Mn) Series	x	Samarskite-(Y)	xx
Euxenite-(Y)	xx	Thorite	x
Fluorite	xx	Topaz	xx
Galena	x	Tourmaline	xx
Gypsum	x	Zircon var. alvite	x
Hydrocerussite	x		

xxx – very common (major mineral), xx – common, x – rare.

The central, thickest part of the Spro pegmatite was mined for nearly 40 years beginning in 1880 by the company "Bruun, Hiorth and Frost" and from in 1904, to around 1920 (its peak in production) by "The United Feltspatbrudd A /S (De forenede Feldspatbrudd A/S)". The mined K-feldspar was navally transported to Gdansk and Stettin in Poland, where it was used in porcelain production (Turtumøygard, 2004). The 230-meter long pegmatite contained a 70-meter long feldspar-rich section from which the mine exploited a 50-meter long portion with a 15-meter width in the center (Bugge, 1955). It was initially mined in an open pit, but later the mining proceeded underground with two galleries (around 10 meters wide), northern and southern tunnels with the latter containing railway tracks to drive out the rock with mine hutches. The workforce consisted in around fifteen workers and about 700 tonnes of feldspar were mined yearly (Turtumøygard, 2004). By 1918 the mine was set to close down due to groundwater related issues and it was definitive by 1920 (Bugge, 1955; Raade, 1965; Turtumøygard, 2004).

3. Samples and methods

3.1 Fieldwork

The study included seven days of fieldwork in which the main objectives were to make a representative geological map of the area surrounding the Spro pegmatite, assemble structural data (e.g. strike and dip of foliations), and collect samples of all present rock units for further description and analysis. The area of approximately ~ 89,250 m^2 (from below 6626400 N to just over 6626700 N; from 32V 589050 to 32V 589300 UTM) consists in a ~ 50-meter high hill located at the western coast of the Nesodden peninsula around 20 km SSW of Oslo and 500 m North of the village Nordre Spro. From South to North, the studied area starts at an abandoned quarry where at its north wall most of the regions' rock units are exposed including the pegmatite dike as illustrated in Fig 9 The north boundary of the area is approximately 30 meters north of the point where the pegmatite meets the shore. From West to East, the area starts at the shore, all the way up and down the hill and terminates approximately 130 meters east of the pegmatite at a densely vegetated area. The terrain has light vegetation from the shore to the hill and has a denser forest on the Eastern section after the hill. There is also a beach with loose material (remnants of the pegmatite mine exploration at the western shore of the area. The outcrop locations and boundaries between different rock types were recorded with GPS coordinates while rock structure, texture, and mineralogy were thoroughly described and documented in field notes and photographs. The regional map can be found on Fig 58.

The samples used in this study were gathered from the Oslo's Natural History Museum collection, and pieces collected on the field by Axel Müller and Pedro Faria. The collection includes samples from the pegmatite, host rocks and specific minerals (e.g. tourmaline, muscovite, alkali feldspar). To further study the samples, the following methods were performed: hand sample characterization, optical microscopy, scanning electron microscopy with energy dispersive x-ray spectroscopy, electron microprobe analysis, and secondary ion mass spectrometry. A detailed sample list is shown in Appendix 8.1.

Following the fieldwork, several samples were selected to prepare for specific methods in order to further analyse, describe and classify the rocks, minerals and their chemistry.

3.2 Sample preparation

Preparation for thin sections
Several samples of host rocks and accessory minerals were used to make thin sections. The collected rock samples were cut at strategic areas (either for representative minerology or specific accessory minerals) on a diamond rotary saw at the Natural History Museum of Oslo. The samples were posteriorly sent to prof. Akhavan at Blindern, which performed thin section preparation (standard 30 µm thickness) as well as epoxy casts polishing.

Preparation of Epoxy casts

Along with thin sections, casts were also prepared as shown in Appendix 8.2. The casts' preparation consisted of the following steps: insertion of double-sided tape on a '25 x 10 cm' flat glass or plastic surface, while on a larger glass unit, silicon powder (Silisunkarbid 80k or 220k which is finer grained for minerals more prone to breakage) was used and mixed with a small amount of water. A small enough piece was removed from the main sample (< 0.5 cm preferably), and the small mineral was grinded against the table in the silicon powder mixture until the desired face/side is flat and the process was repeated for all the selected samples. The tape cover was removed and the outline of the support cup (where the cast would be made) was drawn with north for orientation. The samples were placed on the flat side and their position on the cast was recorded, and the support cup was then placed on the tape and the bottom was surrounded with plasticine to prevent liquid escape. The glass was placed on a disposable box for precaution in case the liquid escapes. The poisonous epofix resin and epofix hardener with a 25:3 ratio was inserted on a disposable recipient with rubber gloves and measured with a scale. These were then mixed with a mixing rod for around 1 minute to create the epoxy "glue" which was inserted in the cast support cups carefully to prevent the samples from falling out of position. A waiting period of 24 hours was required for the epoxy to solidify. After solidification, the epoxy was no longer poisonous and the final result is shown in Appendix 8.2.

Carbon Coating

In order to perform SEM, EDS, and EMPA on the samples, it is necessary to make a carbon coating. The coating is usually 5-50 nm, which is thick enough to generate conductivity on the sample, dissipate charging, prevent overcharge, heat, and build-up or beam damage on the sample without affecting or covering the surface morphology (JEOLUSA, 2018). The coating is performed on an 'AGAR auto carbon coater' (with required use of gloves) and consisted on the following steps: sharpening of the carbon sources if necessary followed by placement of the sample on the sample holder. Closing the top-plate and turning the machine on which is followed by the chamber pump (for around 30 seconds). It was crucial to confirm that the chamber pressure is below 0.05 mb (Vacuum Check), and confirm that the following settings are selected, AUTO mode, voltage 5.0 V and timer 10 seconds. The machine was then started without looking at the process as observing the carbon evaporation is dangerous for the sight. The process was repeated when necessary.

This procedure was instructed and monitored by laboratory managers Ph.D Nélia Castro and Ph.D Eirini Zacharaki.

Table 4. Pegmatite and host rocks thins sections used in optical microscopy, SEM and EMPA.

Sample #	**Locality**	**Rock/Mineral Type**
690a	Spro Pegmatite	Large Tourmaline crystal 1.5 cm diameter
690b	Spro Pegmatite	Tourmaline with beryl and microlite
690c	Spro Pegmatite	Tourmaline in albite vein in muscovite-plagioclase host
20160	Spro Pegmatite	Tourmaline in quartz
18081715	Spro Pegmatite	Tourmaline in sugary albite of replacement zone
04081801	Spro Pegmatite	Amphibole gneiss
04061802	Spro Pegmatite	Strongly deformed granite
05061801	Spro Pegmatite	Deformed granite
05061802	Spro Pegmatite	Amphibole gneiss
05061803	Spro Pegmatite	Granite (undeformed)
05061804	Spro Pegmatite	Amphibole Gneiss

Preparation for whole rock analysis
To obtain representative samples of the studied region's host rocks, crushing, milling and splitting rocks collected during fieldwork was required.

The procedure was realized by placing the cleaned sample individually in a jaw crusher type Christy Hunt 2" x 6" Roll which crushed the sample down to < 5 mm grain size. Then, the splitter was used to separate the sample in equal halves, take one and repeat until one of the containers has 100 grams representative of the rock. Additional 500 grams were taken from the remaining material (after splitting), as reference in case of the necessary repetition of the process or performance of different/further analyses in future.

To avoid any contamination on the sample the method required a strict cleaning procedure during crushing and splitting that consisted in: cleaning the splitter pieces and sample containers with water, alcohol and blow it with compressed air; blow all machine parts and instruments with compressed air after using; drill the crushing plates and its screws, the covering plate and machine parts that were exposed to the sample followed by alcohol wipe and blow with compressed air. Then prior to the following procedure, a plastic bag was inserted between the machine and the plates to minimize machine exposure to the sample and a bucket with two plastic bags underneath the machine to where the crushed sample fell. The whole process was meticulously executed following the instructions of Dr. Gunborg Bye Fjeld. 50 grams of the milled samples were sent ACME laboratories in Vancouver, Canada (ACME Labs, 2018) were inductively coupled plasma mass spectrometry (ICP-MS) and inductively coupled plasma emission spectrometry (ICP-ES) applied on the sample powder fused to lithium tetraborate tablets (analytical codes LF202, PF370 [for Li], GC841 [for F], and PF100 [for B]).

Table 5. Results of host rocks' crushing, milling and splitting for whole rock chemical analysis by inductively coupled plasma mass spectrometry (ICP-MS).

Sample #	**Rock Type**	**100 g**	**500 g**
04061802	Strongly deformed granite	94.97 g	495.27 g
05061801	Deformed granite	106.66 g	515.57 g
05061803	Granite (undeformed)	105.38 g	511.64 g
05061804	Amphibole Gneiss	110.46 g	523.09 g
05061802	Amphibole Gneiss	109.87 g	516.98 g
04061801	Amphibole Gneiss	98.37 g	526.66 g

3.3 Optical Microscopy

The fully prepared thin sections shown in table 4 were then analysed for petrographic studies through a Leica DMLP microscope with an incorporated Leica MC170HD digital camera, also at the Natural History Museum of Oslo. The samples' thin sections (host rocks and tourmalines) were analysed in both PPL (plane-polarized light) and XPL (cross-polarized light) as shown in Figs 14 to 19.

3.4 SEM and EDS

The scanning electron microscope (SEM) was used after the thin section optical microscope descriptions. It allowed a more in-depth observation and characterization of the samples as well as semi-quantitative compositional analyses through the attached Bruker XFlash® 5030 EDS detector. The operating machine was a Hitachi S-3600N.

The SEM is an instrument that allows the visualization of materials at a highly detailed and magnified level (up to 300,000 times) with three main advantages over light microscope*:* resolution at high magnification, depth of field and microanalysis (AMMRF, 2018). The machine consists in an electron gun, anode, aperture holder, condenser aperture, condenser lenses, stigmator, deflection coil, specimen chamber, vacuum as the system also includes an attached EDS detector for semi-quantitative analysis, a computer, settings rotary knobs, navigation trackball and monitors to control the system.

For sample imaging, the electron beam produced by the electron gun scans the sample surface in a vacuum, detects BSE and/or SE signals produced from the sample interaction with the electrons. It then transforms the signal into an image of the sample surface (by amplifying and modulating the brightness of the detected electron signals) which is displayed on an attached monitor. The electron column adjusts the focus and brightness of the specimen using the electron beam generated by the electron gun. The interaction of the electron beam with the sample surface generates secondary electrons (SE), backscattered electrons (BSE), cathodoluminescence (CL) and characteristic X-rays that vary according to the composition of the sample. The BSE reflected after striking the sample are dependent on the sample composition resulting in different grey tones. Heavy elements such as Fe and those with high atomic numbers appear brighter on BSE images and, thus, provide some compositional variation and distribution.

The EDS (Energy Dispersive x-ray Spectroscopy) detector attached to the used SEM system and detects chemical elemental composition and allows the semi-quantitative chemical identification and characterization of targeted points in the sample surface. The EDS is composed of an X-ray detector and software to collect, store and analyse the data. The generated electron beam strikes the specimen surface and the electrons within the atoms of the selected area of interest get elevated to an excited state (NTS, 2018). The electrons in these atoms then return to their ground state, releasing characteristic x-rays, whose respective energy is absorbed by a crystal (in the EDS) through ionization. The x-ray absorption then converts the energy of individual x-rays into electrical voltages of proportional size, as the electrical pulses correspond to the characteristic x-rays of the element (SERC, 2018). The EDS spectrum is displayed as a plot of x-ray counts vs. energy (in keV) and energy peaks correspond to the various elements in the sample. As a result, the EDS technique can detect elements from carbon (C) to uranium (U) in quantities as low as 1.0 wt% (NTS, 2018).

Prior to the SIMS analysis (Sections 3.6 and 4.4.3), the samples were scanned and “mapped” through secondary electron image scanning at the SEM. As previously explained in greater detail, the secondary electrons are generated at or near the sample’s surface, have lower energy than the backscattered electrons and are ideal for topography inspection and characterization.

3.5 EMPA

The electron microprobe analyser (EPMA) enables the determination of the chemical composition at a sub-micron resolution of solid inorganic materials (with atomic numbers >4) in small crystals or polished thin sections. It can be used for point analysis or quantitative X-ray mapping mode and phase identification, on the sample without physically altering it.

The principle of the Electron Probe Micro Analyser (EPMA), involves an electron beam (typical energy = 5-30 kV) focused on a small spot on the sample which liberates heat, energy, matter, cathodoluminescence, resultant backscattered and secondary electrons as well as X-ray photons. The latter is critical to obtaining the sample's surface imaging and composition. The cathodoluminescence, secondary and backscattered electrons are used for imaging purposes.

The electron beam displaces an orbiting electron from an atom in the target and leaves a vacancy that is filled by one that was located at a higher shell, shedding energy and X-ray characteristic of the element. The wavelengths and energies of these X-rays provide information about the chemical elements present in the sample (qualitative analysis) and are later compared to reference materials to determine element concentrations (quantitative analysis) (RUHR, 2018). The wavelengths and respective intensities of the x-rays are measured in the Energy Dispersive System (EDS) to determine the present element's concentrations by Wavelength Dispersive Spectrometry. Only selected identified samples in the petrographic and SEM analyses were probed. The studied samples are given in Appendix 8.10-8.15.

The electron microprobe consists of an electron gun that generates the electron beam, an anode that accelerates the electrons under vacuum towards the sample using high voltages (up to 30kV), a set of electron-optical lenses that focus the beam, ion pumps, alignment coils, automated apertures and beam stabilizer, annular Faraday cup, wavelength dispersive spectrometers, optical encoders, automated gun valve, x-ray counter, vacuum, and a specimen chamber with 2 slots. For navigation with micrometer precision, the sample is mounted on a motor-controlled stage as a computer drives and control the system which also has multiple monitor screens attached to observe the sample in transmitted and reflected light.

A Cameca SX 100 EPMA operating system was used during this analysis with accelerating voltage = 15KeV, beam current = mA, beam size = 5µm. The calibration standards utilized were the natural minerals wollastonite (for Si, Ca), pyrophanite (Ti, Mn), albite (Na), orthoclase (K), apatite (P), $BaSO_4$ (Ba), fluorite (F) and pollucite (Cs); as well as synthetic minerals, compounds and metal - Al_2O_3, MgO, Cr_2O_3, Fe, synthetic orthophosphate $ScPO_4$ (for Sc - Jarosewich and Boatner, 1991), $RbNO_3$ (Rb), synthetic alforsite (Cl). The geochemical microanalysis performed by the EPMA was supervised and instructed by Dr. Muriel Erambert.

3.6 Secondary Ion Mass Sprectrometer (SIMS)

In this study, pieces of the tourmaline samples 690a, 690b and 690c were placed in cast X (as described in section 3.2; given in Appendix 8.16) and taken to the GFZ German Research Centre for Geosciences in Potsdam, Germany for SIMS analysis.

The goal of this analysis is the isotopic study (high precision isotope ratio measurements) of B in tourmalines. The Secondary Ion Mass Spectrometer (SIMS) is an in situ microanalytical, highly sensitive quantitative technique that allows the study of trace elemental and isotopic compositions, distribution of elements in a sample, surface characterization, molecular analysis and depth profiling (CAMECA, 2018). According to CAMECA (2018), SIMS is the most sensitive elemental and isotopic surface analysis method. The 'dynamic' SIMS used in this study, which according to CAMECA (2018) has an in-depth resolution from sub-nm to tens of nm, and detection limit down to ppb level. It produces a high yield of secondary electrons and is mostly used for bulk analysis of trace element and isotopes (SERC, 2018). The method can be applied to any solid material that can be used under vacuum (CAMECA, 2018), and "consumes" sample material at ppb levels as the analysis spots are below than 1 μm deep and 10 μm in diameter (Dutrow and Henry, 2011).

The SIMS instrument used in this study is a CAMECA IMS 1280/HR operated by Frederic Couffignal and supervised by Dr. Michael Wiedenbeck at the GFZ German Research Centre for Geosciences in Potsdam, Germany. The machine specifications and data reduction measurements were posteriorly addressed by Dr. Robert Trumbull. The instrument mainly consists of a primary ion source, sample chamber and holder, secondary ion extraction lens, sectors (magnetic and electrostatic analysers), and detector.

The samples' cast arrived in Potsdam a week prior to the SIMS analysis so that the cast could be prepared in optimal conditions. Upon arriving, the cast was repolished with SiC (silica carbide) and ethanol to remove the carbon coating. It was then coated with a 35 nm thick gold coat (for conductivity) and cut (in height to 12 mm) to fit the sample holder.

The process consisted in a primary beam microprobe shooting primary $^{16}O^-$ ions of 13 kV, 3 nA to a focused target (~ 5 μm) on the sample surface in high vacuum state (Trumbull, 2008). Unrastered 18 seconds preborn was applied before each analysis to remove the gold coat and reach equilibrium sputtering conditions (Trumbull, 2008; The interaction between the primary ions (as they "burry" in the sample) and the sample surface produces favourably positively charged secondary ions (opposite of the primary ions, known as sputtering (Cameca, 2018). After the primary and secondary ions reach a sputtering steady state of equilibrium, the produced ions are then collected by ion lenses and transmitted through a high vacuum environment (SERC, 2018). The ions are accelerated, focused and filtered according to their mass-over-charge ratio through electrostatic and magnetic analysers known as sectors (GFZ, 2019; SERC, 2018). The machine magnet retains the same magnetic field strength throughout the entire analysis. Finally, the measurements are concluded at the mass spectrometer analyser where ^{11}B and ^{10}B are separated and measured in different chambers in the machine. The detector then produces the results which are later corrected using measured data IMF values due to the machine-generated fractionation at rates of ~3-4% (35-40 permil^d) (Trumbull, 2008).

The instrument has the ability to count individual ions results in detection limits in the parts-per-billion range for many elements (GFZ, 2019). The mass resolution ($M/\Delta M$) to resolve the $^{10}B^1H$ and $^9Be^1H$ peak needed for B isotopic studies was ~2000 permil^d and the analytical repeatability down to below 0.2 ‰ (1sd). The standard reference samples of tourmalines (dravite (#108796), schorl (#112566) and elbaite (#98144) described by Dyar *et al*., (1998, 2001)) from the Harvard mineral collection were used to calibrate the instrumental and matrix-induced isotopic fractionation (Trumbull, 2008). The complete tourmaline SIMS analyses data is presented in Appendix 8.16.

4. Results

4.1 Field description of the Spro pegmatite and its host rocks

The studied area sits on the footwall of the half-graben with the Nesodden Fault Segment (NFS), the northern segment of the Oslofjorden Fault. It is one of the major N-S to NE-SW trending faults that delimit the Oslo Rift and display evidence of ductile and brittle deformation regimes (active during the Permo-Carboniferous) (Swensson, 1990). The Spro pegmatite is part of the Sveconorwegian rock suite exposed at the Nesodden peninsula. It has a length of approximately 230 meters and extends from the north wall of the abandoned Nordre Spro gravel quarry to the shore of the Oslo Fjord where it meets NFS (underwater) which runs parallel to the shoreline (Bugge, 1955).

In contrast to other Sveconorwegian pegmatites which commonly occur in clusters, the Spro pegmatite forms as an isolated body being the only major pegmatite body in a 30-kilometer radius. It forms a vertical dyke with variable thickness from 1 to 25 m. The pegmatite widens up beneath the hill along a major N-S-striking shear zone and continues all the way until it meets the shore as the elevation decreases.

The Spro area is composed by amphibolite facies to migmatitic amphibole gneisses, variably deformed granite and the Spro pegmatite body (not affected by metamorphism). The amphibole gneisses can be found sheared into the granites, heavily ductile deformed displaying migmatization in particular by the shore (Fig. 58). Amphibolite boudinsare also found sheared concordantly into shear-planes of the deformed granite close to the major shear zone (Fig 9). These amphibolitic basement rocks have protolith ages between 1600-1900 Ma (Versteeve, 1975; Jakobsen and Heier, 1978; Pedersen *et al.*, 1978; Skiold, 1976). According to Pózer Bue (2008), the granite from the Spro area has a crystallization age between 1542 and 1493 Ma. These rocks were metamorphosed under amphibolite facies metamorphism with some migmatitization during the Sveconorwegian Orogeny (950-1200 Ma) (Magnusson, 1960; Graversen, 1984; Swensson, 1990).

The complex tectonic history of the region is evidenced in the degree of deformation of the host rocks, boudinage, and presence of shear zones. The region also contains many discordant quartz veins, with thickness varying from <1cm to nearly 20cm. These are usually found in heterogeneous areas where amphibolite is sheared into the granite, especially in the southwestern region of the studied area. Outcrops on the area (at the shore), are also characterized subparallel scratches at ice-polished rock surfaces caused by glacier movements during the last ice coverage c. 14,000 years ago (Older Dryas) (e.g. Vorren and Mangerud, 2008).

In the quarry located on the southern region of the studied area, the northern wall exhibits the pegmatite dyke and the most common host rocks exposed in the area as shown in Figure 9.

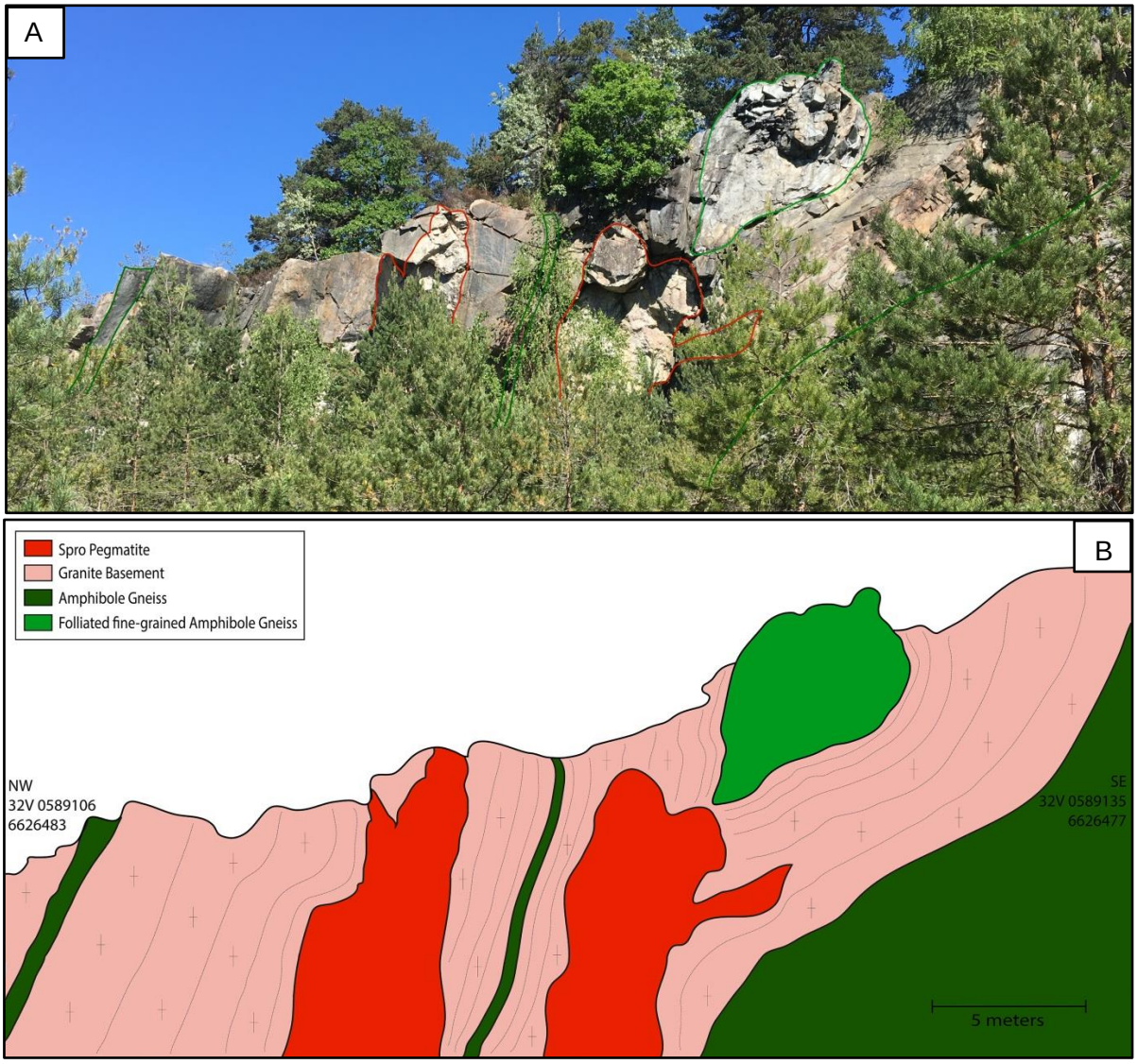

Fig 9. A) Photograph of the quarry's north wall with the exposed rock units. B) Schematic geological section of the quarry wall showed in Figure A) displaying the foliated granite with in-sheared boudin amphibole gneiss (light green) and intruded by the Spro pegmatite. The increasing proximity of the thin lines reflects increasing foliation and deformation degree towards the pegmatite intrusions which sit at the centre of a major shear zone.

The rock units present at the Spro pegmatite region are described as follows:

Spro Pegmatite

The pegmatite dyke (nearly 230 meter long and 25 meters thick at its core) displays an easily recognisable white coloration and consists mostly of large (cm- to m-scale) crystal aggregates of quartz, muscovite, K-feldspar and albitic plagioclase. Due to the fact that most of the pegmatite has been mined, it is hard to infer if there was internal zoning (e.g. a blocky core zone). Despite that, it is possible to conclude from the preserved parts of the body that the Spro pegmatite is quite homogeneous and is not distinguishably zoned. However, inside the mine galleries (from the pegmatite margin towards the core) the size of quartz, feldspar and mica aggregates increases and muscovite becomes more abundant. At the wall zone, near the contacts, the mineral aggregates are smaller, the accessory minerals are less abundant, and the plagioclase is more abundant than the K-feldspar, quartz and muscovite.

These major minerals are cross-cut and partially replaced by late irregular veins (mm- to 20 cm in width) of sugary albite as seen in Figure 10-E. Most of the tourmalines are found in the veins together with topaz (up to 5 cm), beryl (up to 6 cm) and fluorite (up to 5 cm). These albite-tourmaline zones are very distinct from the main pegmatite body, both in texture and mineralogy, and are further analysed in this study.

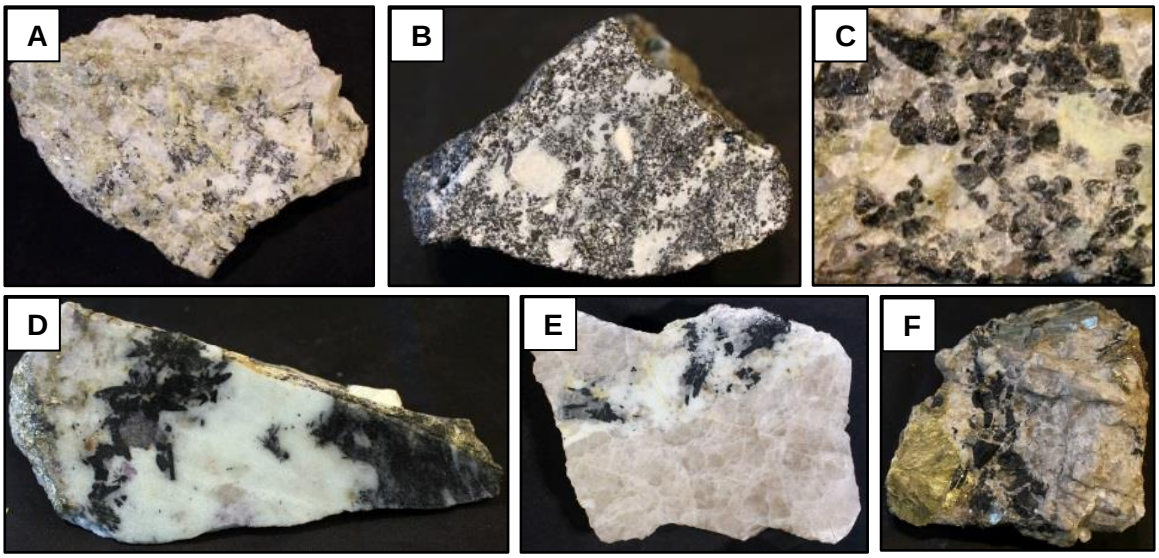

Fig 10. Spro pegmatite samples, highlighting tourmaline occurrences in the albite-tourmaline zones: A) Sample 18081714; B) Sample 690c; C) Sample 04061824; D) Sample 18081715; E) Sample 690; F) Sample 20160.

The accessory minerals include but are not restricted to the following minerals described according to analysis from this study, Raade (1965) and reports by the Geologisk Museums Venner (1991a-b, 1993 a-b). Fluorite found as single crystals (< 3 cm), coating on other minerals and crystal aggregates (up to 15 cm) with a strong purple tint. Black tourmalines are found as thick prismatic and columnar crystals of different sizes ranging from <1 mm to 6 cm that are usually triangular in cross-section. Characteristic for the Spro pegmatite is also the occurrence of irregular batches of black samarskite up to 4 cm in size (Figure 11-A). Thorite as shinny dark grey irregular batches (up to 3-4 cm). Altered monazite fragments (up to 2 cm) found in microcline (Raade, 1965). Topaz as clear faint-green crystal masses up to 5 cm and found near tourmalines.

In addition, according to Raade (1965) the following minerals were identified in the Spro pegmatite: calcite seen in large clusters (10-20 cm); beryl as bluish-green euhedral crystals (1-2 cm) often altered; rare occurrences of microlite euhedral brown crystals (1-3 mm) and irregular masses found in quartz; very rare occurrences of brown euxenite in microline; columbite as small black crystals (up to 2 cm); white apatite in small masses; as well as very rare occurrences of pyrite, chalcopyrite, molybdenite, gypsum and malachite.

Some other minerals were also described in reports by the Geologisk Museums Venner (1991a-b, 1993 a-b) (see Section 2.7) and include: Porous aggregate of white bertrandite, plate-shaped crystals (<1 mm long) in microcavities; thin prisms of alvite, up to 7 mm long, in the form of a zoned radial aggregates associated with violet fluorite and yellow-green muscovite embedded quartz and sugary albite; dense masses of small brownish-yellow anatase, a pseudomorphic alteration product of yttrian titanite; fine-grained yellowish bastnäsite as aggregates of lath-shaped crystals; hydrocerussite as a white coating on galena.

A complete inventory of the accessory minerals found in the Spro pegmatite is previously described in Table 3.

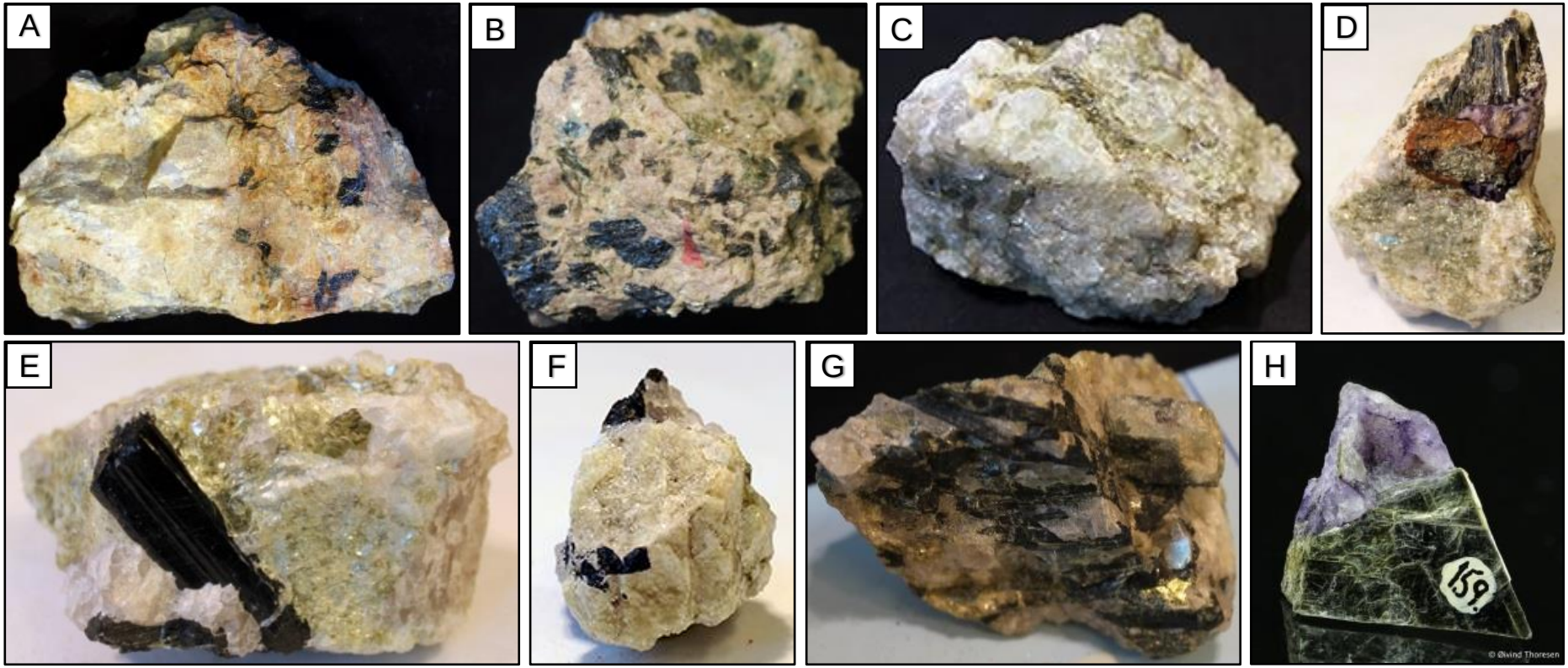

Fig 11. Examples of accessory minerals found in the Spro pegmatite : A) Samarskite-(Y) (black) in K-feldspar (sample 41072); B) Euxenite-(Y) (marked with red arrow) surrounded by black samarskite-(Y) batches (sample 35699); C) Topaz occurrence (white mineral in front) within quartz and green mica (sample 690); D) Fluorite and pyrite next to muscovite (sample 157); E) Large tourmaline prismatic crystal surrounded by quartz and green mica (sample 690); F) Beryl prismatic crystal fragment.; G) Large beryl crystal surrounded by elongated tourmaline crystals; H) Fluorite on muscovite (sample 159), photo by Øivind Thoresen.

Spro Granite

The dominant granitic rock exposed in the study area is a variably deformed weakly porphyritic granite (named Spro granite). It is vastly abundant in the central and western region of the studied area, as a massive light-pink basement unit. The granite is mainly medium to coarse-grained, weakly porphyritic, composed by K-feldspar (often as euhedral phenocrysts up to 2 cm), quartz, plagioclase and mica (biotite). Accessory minerals include zircon, apatite, titanite and some opaque minerals.

Macroscopically, the entire sequence of different deformation degree of the Spro granite is found in the area comprising: undeformed granite with weakly porphyritic texture (Fig 12-A), slightly foliated granite with aligned biotite aggregates which are partially altered to chlorite (Fig 12-B), and strongly foliated granite with fine mylonitic texture (Fig 12-C).

The deformation degree of the granite increases towards the Spro pegmatite body which sits in the center of a major shear zone (see also Fig. 9, quarry wall illustration). With increasing proximity to the major shear zone, the deformation degree on the granites increases displaying decreasing grain size, mineral stretching, and alignment in foliation, along with mica alteration to chlorite.

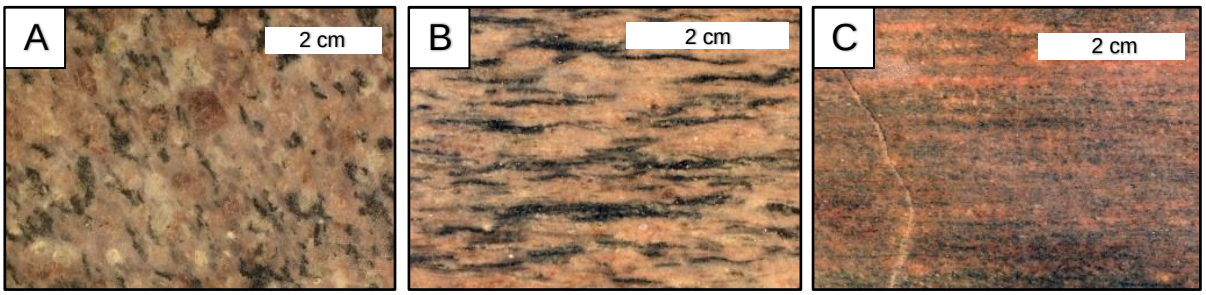

Fig 12. Granite samples variation representatives. A) Undeformed granite; B) Deformed granite; and C) Very deformed granite.

Amphibole gneisses

Amphibole gneisses of various textures are the most abundant rock formation in the eastern region of the studied area but occur also as mega boudins within the Spro granite, west of the major shear zone (as shown in Fig 58)

The most common variety is dark-grey, equigranular and homogeneous, medium to fine-grained and consists of amphibole, plagioclase, quartz, some biotite and in the sheared varieties also muscovite. The rock exhibits a strong foliation marked by the alignment of amphibole and micas (Fig 13-A). Close to the shear zone, just east of the pegmatite body, there is a muscovite-bearing, strongly foliated variation of the amphibole gneiss. It consists of a light-grey, shiny, fine grained and platy variation. The mineral assemblage is mica-rich, and includes amphibole, quartz and some plagioclase. The muscovite is interpreted as an alteration produced of amphibole when water was introduced during retrograde shearing.

There is also an area, located by the shore, which is characterized by highly ductile deformed, heterogenic amphibole gneiss, with indications of migmatization and mobilized and ptygmatic folded leucosomes and as seen in Fig 13-C.

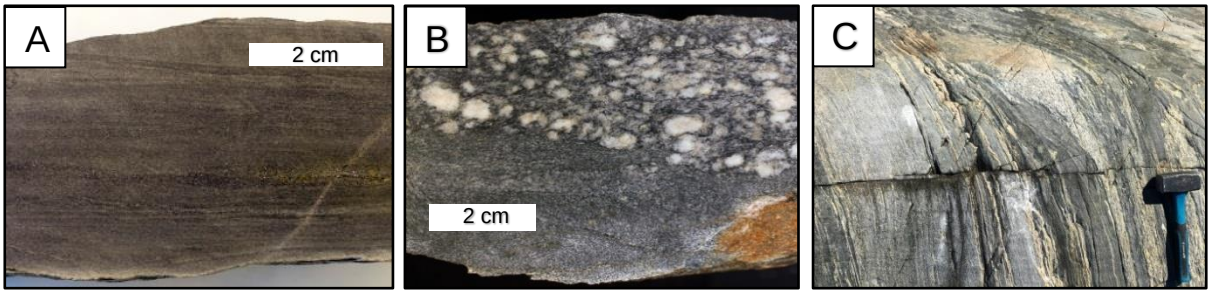

Fig 13. Amphibole gneiss samples. A) Foliated sample; B) Amphibole encasing granitic minerals - contact; and C) Very deformed, folded migmatized amphibolite.

4.2 Petrography and chemistry of the host rocks

To further study and characterize the Spro pegmatite host rocks, six thin sections of six host rock samples were analysed through optical microscopy. The samples consist of granites (with varied degrees of deformation from nearly undeformed to very deformed) and amphibole gneisses. The following figures (from 14 to 20) were recorded during the petrographic study as previously explained in Section 3.3, and all were taken at 5x magnification with a field of view of 1.2 mm.

Amphibole gneiss - Sample 04061801

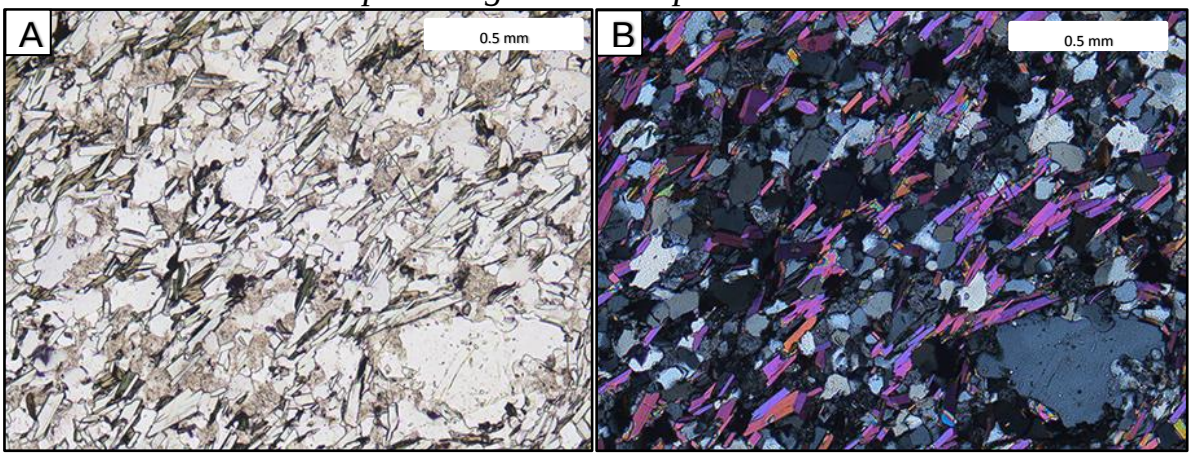

Fig 14. Representative thin section of sample 04061801. A) PPL view; B) XPL view.

The mineral assemblage of this amphibole gneiss consists in biotite (25%), amphibolite (15%), quartz (30%), plagioclase (10%), sericite (15%) some and opaque minerals 5%. The amphiboles have a subhedral shape, strong olive green coloration and reach up to 0.3 mm. The abundant biotites display a strong pleochroism from colourless to light brown/green and range in size from >0.1 mm to 0.6 mm. They occur as tabular and elongated crystals and define a weak (compared to the other amphibole gneisses) but still recognizably foliation. The quartz grains range from >0.1 mm to 0.7 mm and display a rounded anhedral shape. The plagioclase crystals are colourless, exhibit an anhedral shape and reach sizes of 0.3 mm. The sericite is well spread out and exhibit a light brown/grey turbid coloration and reach up to 0.3 mm. Rare opaques occur as small (<0.1 mm), subhedral and black minerals.

Spro granite (very deformed) - Sample 04061802

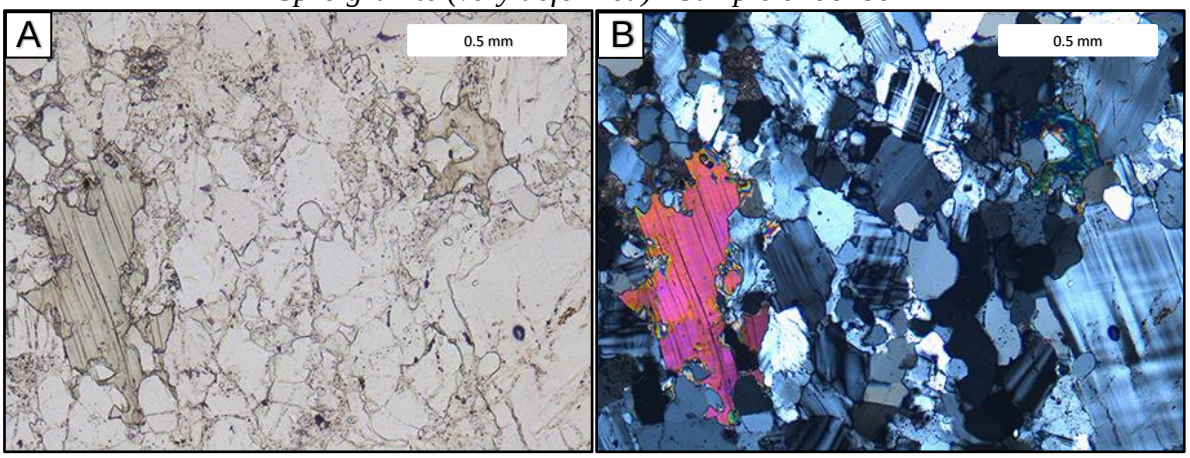

Fig 15. Representative thin section of sample 04061802. A) PPL view; B) XPL view.

The mineral assemblage of this sample constitutes quartz (30%), microline (25%), muscovite (15%), plagioclase (15%), sericite replacing feldspars (10%) and opaque minerals (5%). The quartz crystals are abundant and spread throughout the sample as anhedral and rounded shaped grains averaging ~0.4 mm in diameter. In certain areas, the quartz grains are elongated and aligned. Microline in this sample display subhedral tabular shapes with low-med relief, a distinctive tartan twinning under XPL, and range from 0.2 to 0.7 mm in size. Muscovite occurrences are spread out through the sample, as elongated subhedral grains and in some cases form ~1mm long alignments. The micas also display the characteristic perfect cleavage and high birefringence. Plagioclase grains reach up to ~0.5 mm in size and exhibit tabular subhedral shape. In various areas of the sample, the feldspar is replaced by turbid greyish sericite including a nearly 2 cm long vein across the thin section. Minor opaque minerals occurrences have dimensions below 0.1 mm and anhedral irregular shapes.

Spro granite (deformed) - Sample 05061801

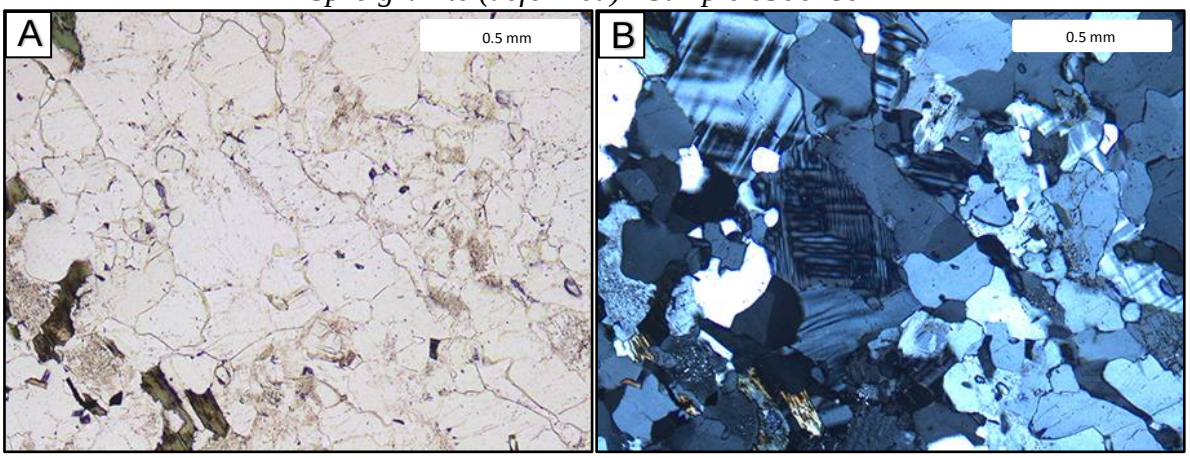

Fig 16. Representative thin section of sample 05061801. A) PPL view; B) XPL view.

The major minerals in this sample are quartz (30%), microline (25%), sericite (15%), amphibolite (15%), plagioclase (10%), and opaques (5%). Quartz is abundant in this sample and the grains with 0.2 mm of average dimensions form large (~1 cm) masses. The microline crystals occur as subhedral crystals 0.2-0.8 mm in size and display the typical tartan twinning. Plagioclase (up to 0.5 mm in size) displays Carlsbad twinning and is partially replaced turbid greyish sericite (up to 0.8 mm in size). The amphiboles occur as deformed and broken light brown-green crystals and are pleochroic in some cases. The broken grains form irregular

aggregates reaching up to ~0.6 mm in size. Similarly to the previous samples, the opaque minerals are rare and usually below 0.1 mm in size.

Amphibole Gneiss - Sample 05061802

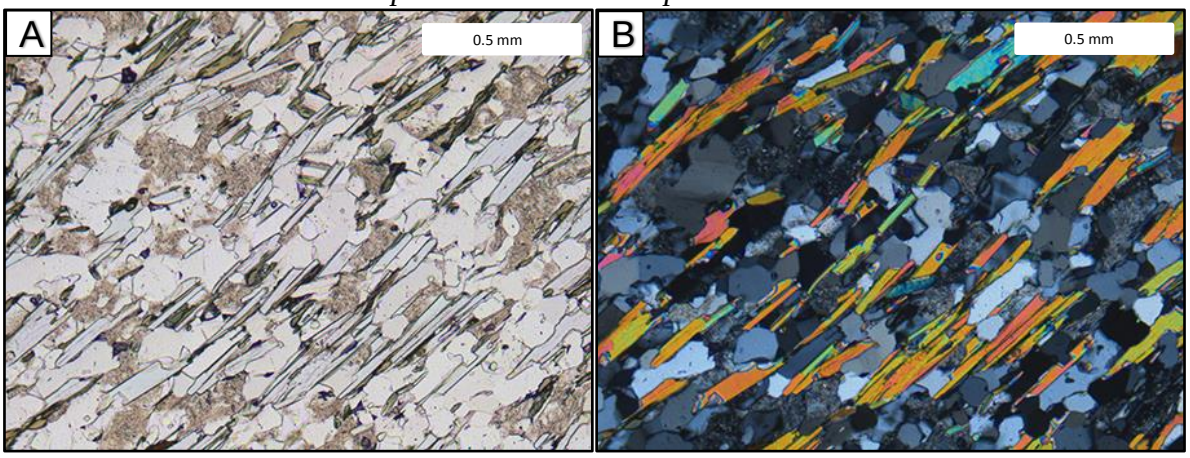

Fig 17. Representative thin section of sample 05061802. A) PPL view; B) XPL view.

This sample is composed by quartz (30%), amphibole (15%), biotite (20%), plagioclase (10 %), sericite (20%) and opaque minerals (5%). This sample is generally richer in quartz compared to the other two investigated amphibolites and displays two distinct mineralogical regions. One region with more abundant amphiboles and thus slightly less quartz, and one finer-grained where quartz is more dominant while the amphiboles and biotites are rarer. The quartz grains exhibit similar anhedral round shapes and 0.1-0.3 mm in average size while the amphiboles display some differences. The amphiboles are rarer and smaller (0.1-0.4 mm) in general and exhibit a light brownish tint. The tabular, elongated and aligned biotites (0.2-0.4 mm in size) are similar and define a strong foliation. The overall pleochroism is weaker and the colour varies from pale/colourless to a brownish tint. The plagioclase crystals are colourless subhedral, exhibit carlsbad twinning and reach up to 0.4 mm in size. The sericite is common/well spread out in this sample, display the light brown/grey turbid coloration and reach up to 0.4 mm. The opaque minerals are rare and small (<0.1 mm).

Spro granite (undeformed) - Sample 05061803

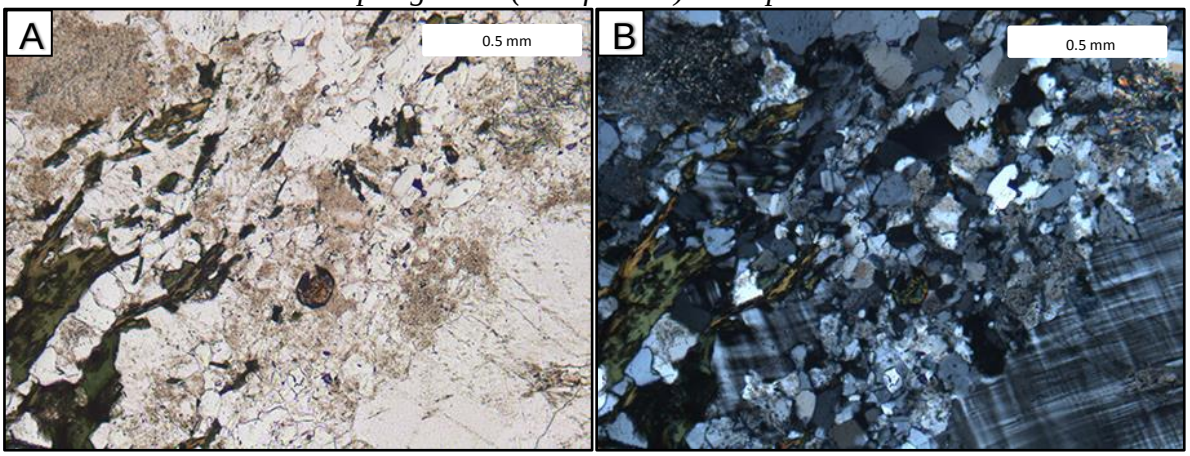

Fig 18. Representative thin section of sample 05061803. A) PPL view; B) XPL view.

The mineral assemblage of this sample is quite heterogeneous and includes larger crystals than the deformed varieties of the Spro granite. The present minerals consist in microline (30%), quartz (20%), amphibolite (20%) sericite (15%), plagioclase (10%), pale pink (3%) and opaques (2%). Euhedral microline reaches dimensions up to nearly 7 mm and displays the common tartan twinning. Quartz crystals are subhedral and form aggregates surpassing 2 mm. The olive green to brow amphiboles also forms aggregates (skeletal and irregular shapes) up to 4 mm, and some display pleochroism. The subhedral to euhedral colourless plagioclase crystals reach nearly 3 mm and exhibit Carlsbad twinning. The replacement mineral sericite exhibits a foggy light brown to greyish colour. Inside the larger sericite agglomerates occur small subhedral micas (< 0.2 mm) as in the other granite samples. Similarly to the previous samples, the opaque minerals are rare and usually below 0.1 mm in size.

Amphibole Gneiss - Sample 05061804

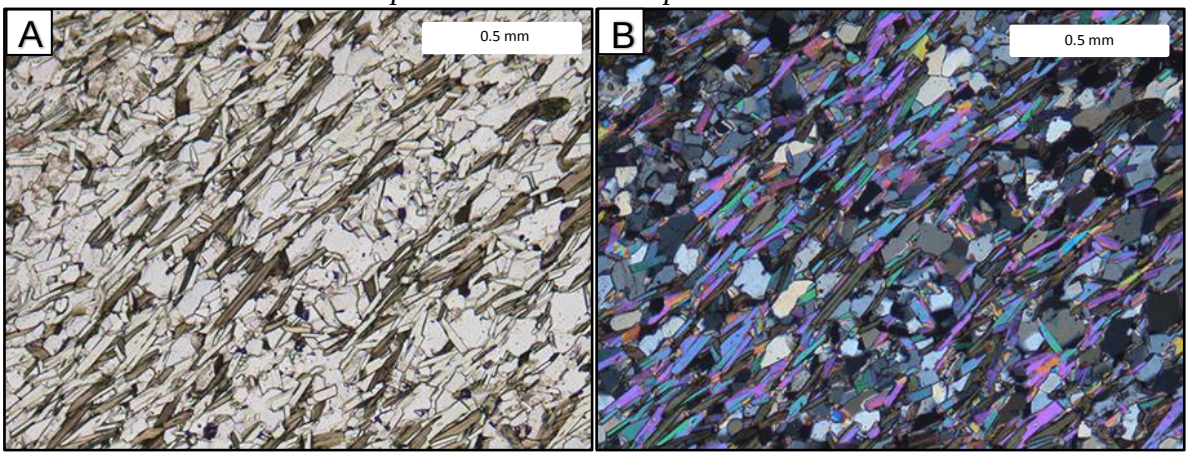

Fig 19. Representative thin section of sample 05061804. A) PPL view; B) XPL view.

The mineral assemblage of this sample is composed by quartz (30%), amphiboles (15%), biotite (20%), plagioclase (10%), sericite (10%), green tourmaline (10%) and opaque minerals (5%). Quartz occurs as rounded anhedral crystals reaching up to 0.3 mm in size. The amphiboles are found as subhedral 'fragments' with dimension from 0.1 to 0.6 mm, with a light brown to olive green colouration. The biotites are tabular shaped, weakly pleochroic (from colourless to brown), reaching sizes of 0.5 mm. This sample exhibits the strongest foliation with biotites and some amphiboles aligned. Plagioclase occurs as colourless subheadral crystals up to 0.4 mm with low relief and carlsbad twinning. The sericite exhibits the usual turbid grey-brown colour and reaches up 0.4 mm in size. There is an occurrence of green tourmalines as euhedral prismatic crystals of up to 0.5 mm in diameter. Rare opaque minerals occur with dimension below 0.1 mm.

4.3 Whole Rock Chemistry

To further understand the Spro pegmatite genesis and the emplacement environment, six host rock samples were selected for bulk chemistry analysis including major and trace elements. Data from host rock samples 04061801, 04061802, 05061801, 05061802, 05061803 and 05061804 as well as the bulk Spro pegmatite and the albite-tourmaline zones, samples 16091806 and 690 respectively was acquired by solution ICP-MS at ACME Laboratories in Vancouver, Canada. The whole rock chemistry data are given on Appendix 8.5-8.6.

Firstly, to characterize the host rocks in the Spo pegmatite area, two plots (Figs 20 and 21) were constructed to discriminate between magmatic or non-magmatic origin of the metamorphosed rocks. Because of the strong metamorphic overprint, it was not possible to specify visually whether the protoliths of the fine-grained amphibole gneisses were sedimentary or igneous rocks. For the TiO_2 vs SiO_2 plot, all the samples including gneisses and granites display TiO_2 values below 0.65 wt% and SiO_2 values above 62 wt% defining them as igneous rocks. In the Zr/Ti vs Ni plot the samples Zr/Ti ratios fit between 0.01 and 0.1 while the Ni content below 25 ppm. This indicates that every sample plotted has a magmatic origin.

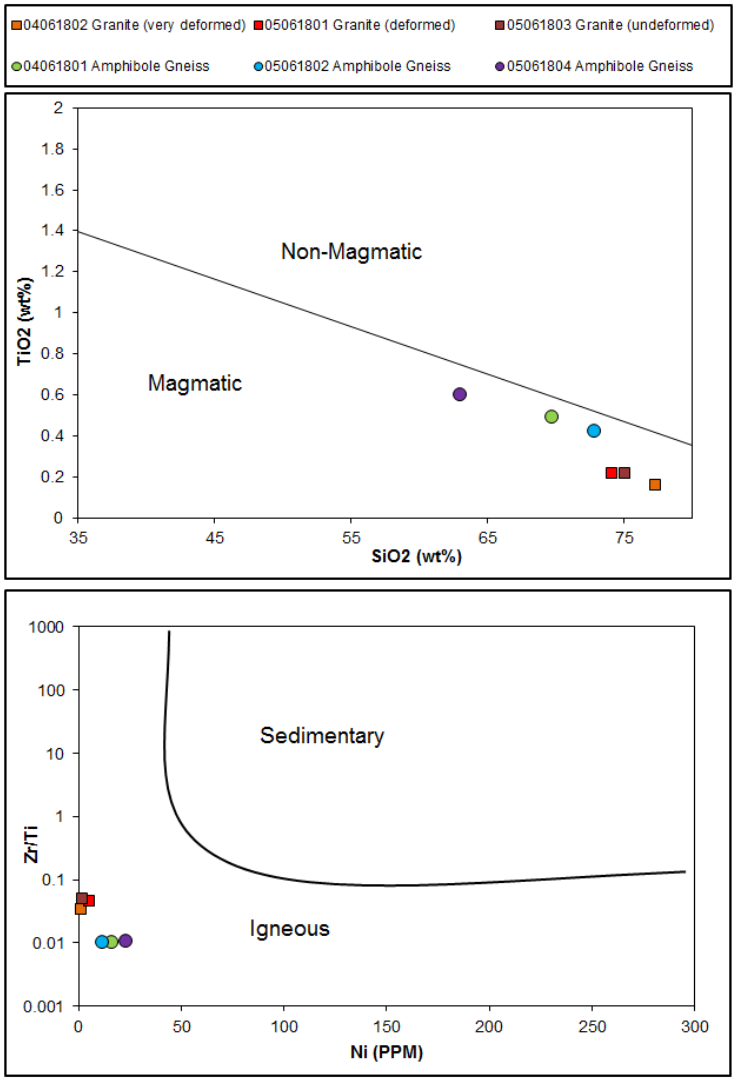

Figs 20 and 21. Plots for disclosure of protolith's nature: igneous vs sedimentary. (TiO_2 vs SiO_2 wt%; Zr/Ti vs Ni ppm after Winchester and Max (1984) and Winchesterand Floyd (1977) respectively).

The total alkali vs SiO_2 (TAS diagram) shown in Fig 22, was then used to classify the type of igneous rock to which the Spro pegmatite host rocks belong. The samples recognized in the field as the pegmatite and granite samples fall in the granite field, while the samples described as amphibole gneiss samples spread over a larger area from granite (sample 05061802), granodiorite (sample 04061801) and diorite (sample 05061804). The granites have SiO_2 content above 74 wt % and total alkalis sum to approximately 8 wt%. The amphibole gneisses display SiO_2 between 62 and 73 wt% and total alkalis sum to approximately 6.3 wt%.

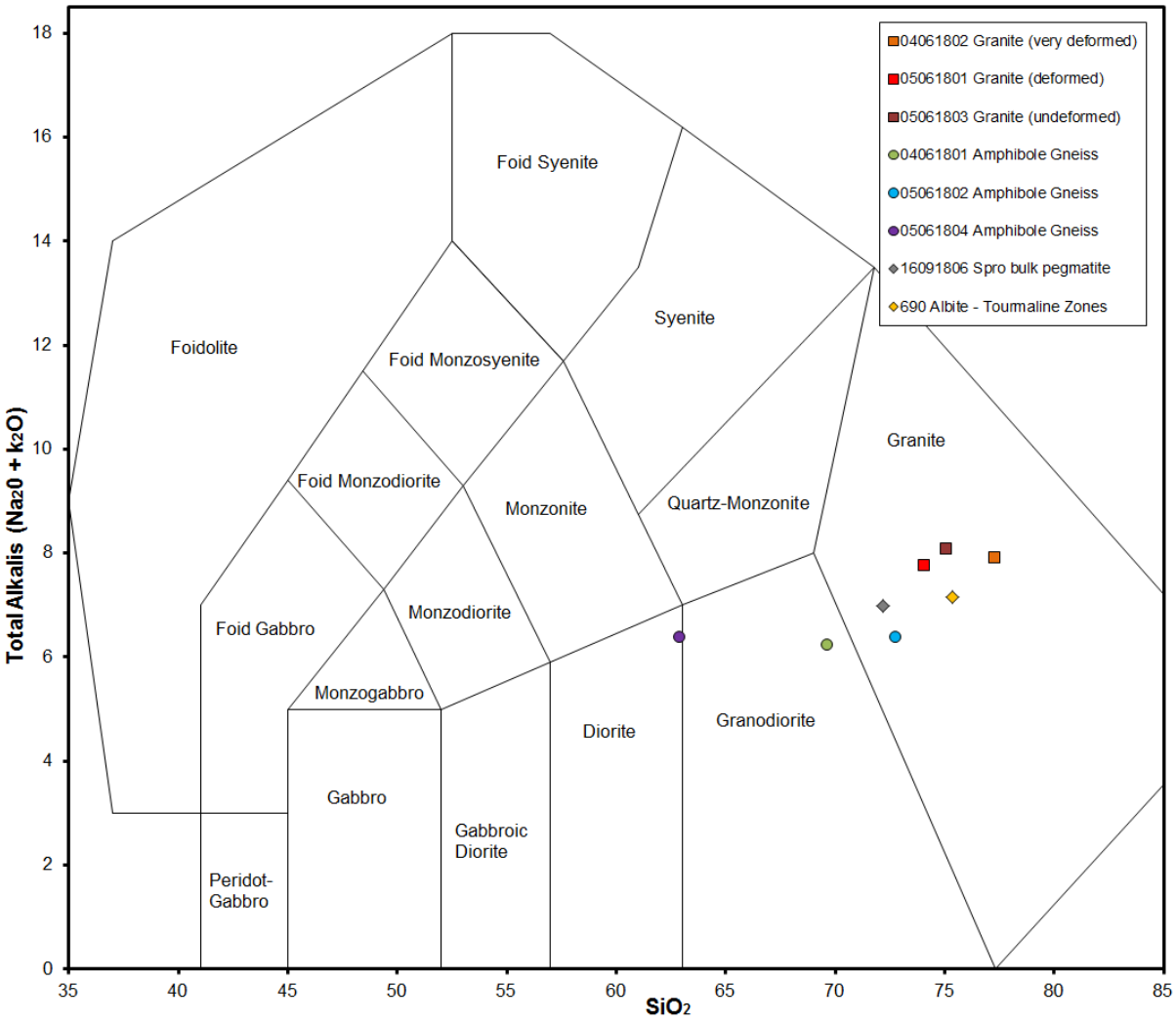

Fig 22. TAS diagram (Total alkalis vs SiO_2) showing the igneous classification of the studied host rocks, showing the granites and pegmatites classified as granites while the amphibole gneisses display greater variation with classification from diorite to granite. After Le Bas *et al.*, (1986).

On the $Al_2O_3/(Na_2O + K_2O)$ (A/NK) vs $Al_2O_3/(CaO + Na_2O + K_2O)$ (A/CNK)) diagram (Fig 23), all the investigated samples are classified as peraluminous. The three granitic samples have A/CNK ratios slightly under 1.5 while the A/NK ratios for samples 04061802 and 05061803 are also just below 1.5, sample 05061801 display a ratio above 2.0. The amphibole gneisses have A/CNK ratios ranging between 1.75 and 2.5 while the A/NK ratios sit between 2.0 and 2.8. The pegmatite samples have A/CNK ratios of approximately 1.8 and A/NK ratios between 1.95 and 2.25.

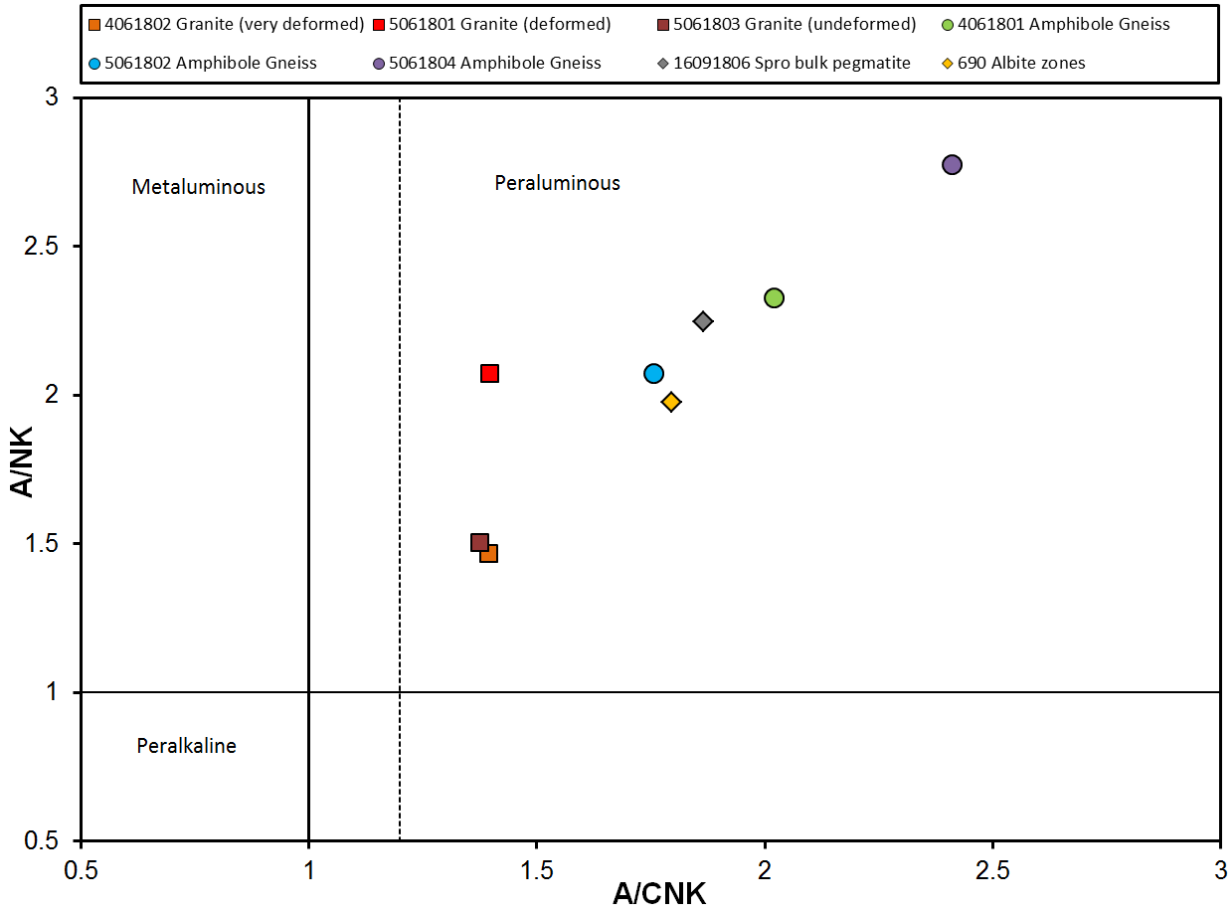

Fig 23. A/NK (Al_2O_3/Na2O + K2O) vs A/CNK (Al_2O_3/CaO + Na2O + K2O) discrimination plot adapted from Shand (1943) (Müller *et al.*, 2018).

According to granite type classification plots adapted from Whalen *et al.*, (1987) seen in Figs 24 and 25, the amphibole gneisses have compositions sitting on the M-, I- and S-type range. These samples are FeO- and MgO-rich but K_2O-poor compared to the granitic host rocks. The pegmatite and the granitic samples display variation due to the metamorphism and alteration. These variations are suspected to represent a transition from A- to I-type granites.

The Spro pegmatite, which belongs to the NYF family, has its samples in the A-type field (anorogenic and anhydrous granites) of the 10000*Ga/Al versus K_2O+Na_2O/CaO classification diagram as expected. However, in the Zr+Nb+Ca+Y versus FeO/MgO discrimination diagram the Spro bulk composition plots in the "Fractionated felsic granite" field whereas the Spro albite tourmaline zone composition has A-type signature. Summarizing the classification plots, the granitic host rocks represent A-type granites whereas the Spro pegmatite, which also has an A-type affinity, is further discussed in this study.

The granite samples display compositional variations. Sample 04061802 is the richest in SiO_2 but is Fe_2O_3-, Na_2O- and especially CaO-poor, while sample 05061801 is recognizably Fe_2O_3-rich. These variations may reflect different fractionation degrees of the granite or the different deformation degrees of the collected samples may have caused modifications of their bulk composition.

The pegmatite samples are generally Fe_2O_3- and K_2O-poor but Na_2O-rich compared to the granitic host rocks. The bulk pegmatite (sample 16091806) is the poorest in K_2O but the richest in Na_2O and CaO. Both pegmatite samples are FeO- and MgO-poor. The TiO_2 and P_2O_5 contents are very low for both samples but sample 690 exhibits the lowest values. For more detailed chemical composition of the samples please refer to Appendix 8.5-8.6.

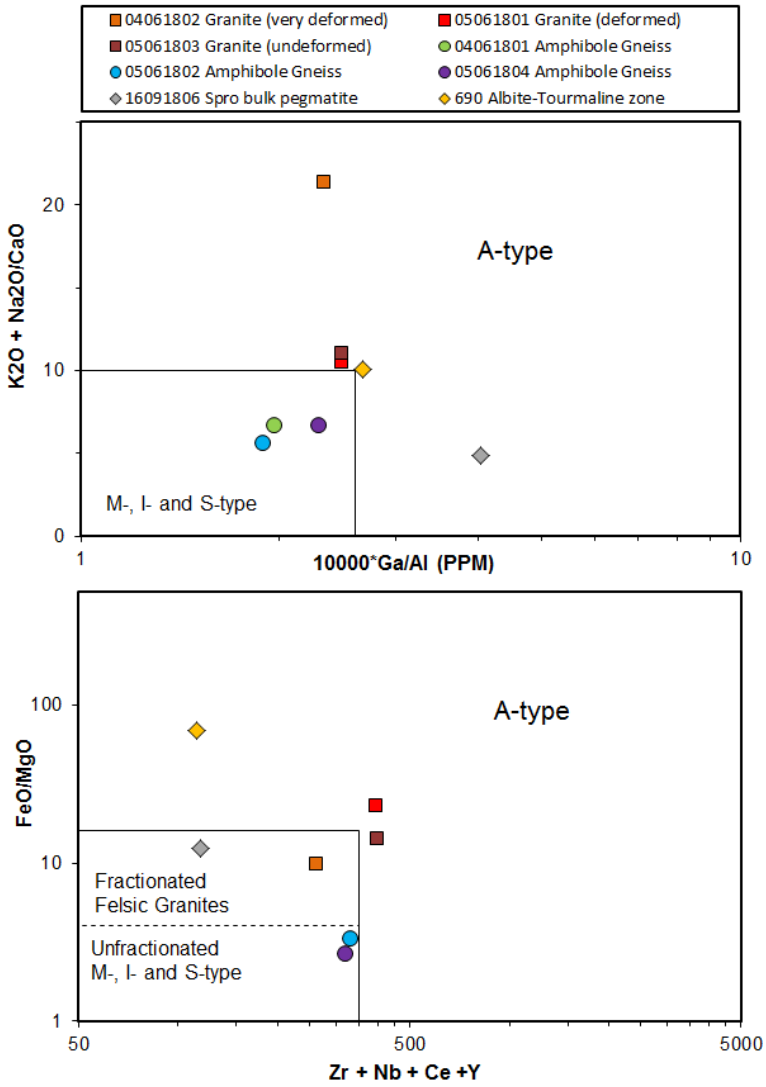

Fig 24 and 25. Granitic discrimination plots after Whalen *et al.*, (1987).

The upper continental crust-normalized diagram of selected incompatible elements (Fig 26) adapted from Rudnick and Gao (2004) was constructed to determine if there is a genetic relationship between the pegmatite and the host rocks. In comparison to the average upper crust composition, the amphibole gneisses are slightly depleted in Sr and Ti and slightly enriched in Rb, Y, and Yb. Otherwise, the amphibole gneisses correspond roughly the upper continental crust composition.
The granitic samples show similar distribution patterns as the amphibole gneisses with the difference that they are slightly enriched in most elements compared to the average UCC. The most distinct features are the relatively strong depletion in Ba, Sr and Ti and the enrichment in Rb, Y, and Yb. Within the granitic samples, the major differences are in sample 04061802 which is more depleted in most elements than the other samples.

The pegmatite samples show very different patterns characterized by strong depletion in Ba, La, Ce, Sr, Nd, Sm, Zr, Hf and Ti, whereas Rb, Yb and particularly Nb and Ta are strongly enriched. Despite the similar pattern of the bulk pegmatite and its albite-tourmaline zones, both samples display distinct features. Sample 690 (albite-tourmaline zone) is significantly more depleted in Sr and Zr while also being much more enriched in Nb and especially Ta. The incompatible element signature suggests that the pegmatite does not have a genetic relationship with the granitic nor the amphibole host rocks and the albite-tourmaline zone represent the most fractionated part of the pegmatite as inferred by textural relationships.

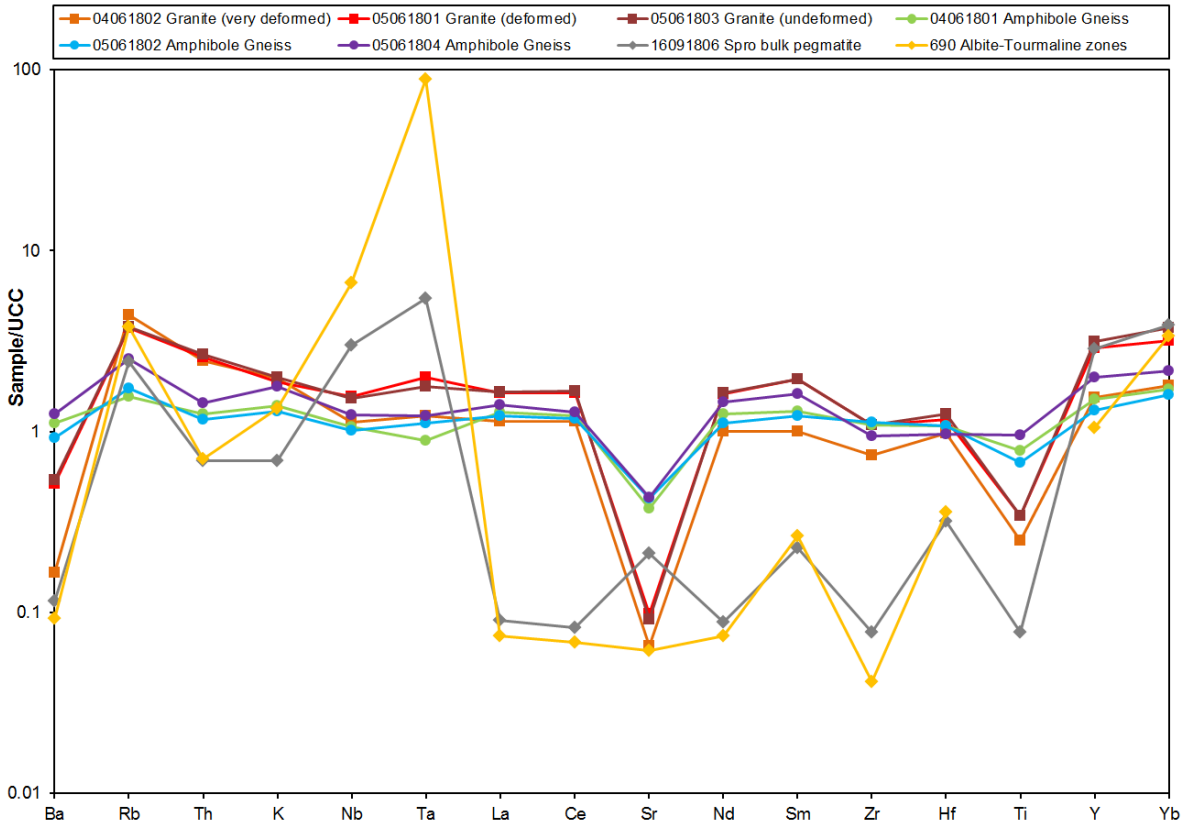

Fig 26. Upper Continental Crust (UCC)-normalized diagram of selected incompatible elements adapted from Rudnick and Gao (2004).

In addition, a REE discrimination diagram (Fig 27) adapted from Anders and Grevesse (1989) was used to get more information about rocks genesis, evolution and fractionation level. Overall, the host rocks are strongly enriched in light REE and become more depleted along the heavy REE. The pegmatite samples are much less enriched in light REE than the host rocks and become increasingly enriched in heavy REE. The granite sample 04061802 is the most fractionated sample with the largest negative Eu anomaly of 0.111, followed by Ab-tourmaline zone in the pegmatite sample 690 with 0.170, then the granitic samples 05061801 and 05061803 with values of approximately 0.255, amphibole gneiss sample 05061804 and bulk pegmatite around 0.486, and amphibole gneisses samples 04061801 and 05061802 with values over 0.535. The amphibole gneisses display poor fractionation patterns and have a small negative Eu anomaly. The granitic samples 05061801 and 05061803 display a similar pattern, slightly more enriched in every REE with the exception of Eu. Sample 04061802 also has a similar pattern but is more depleted in all REE than the other granites and even more depleted than the amphibole gneisses in light REE. In addition, sample 04061802 is the most fractionated rock with a very strong negative Eu anomaly. As expected, the pegmatite sample from the albite-tourmaline zone exhibits high levels of fractionation with strong negative Eu anomaly. The albite-tourmaline zone is more depleted than the bulk pegmatite body in every REE with the exception of Sm. The samples are very similar in the light REE while the differences accentuate in the heavy REE and are most significant in Eu. The Spro pegmatite samples' REE signature patterns are very different from the host rocks' patterns. Thus, it is very unlikely that the pegmatite melts originate from the investigated host rocks.

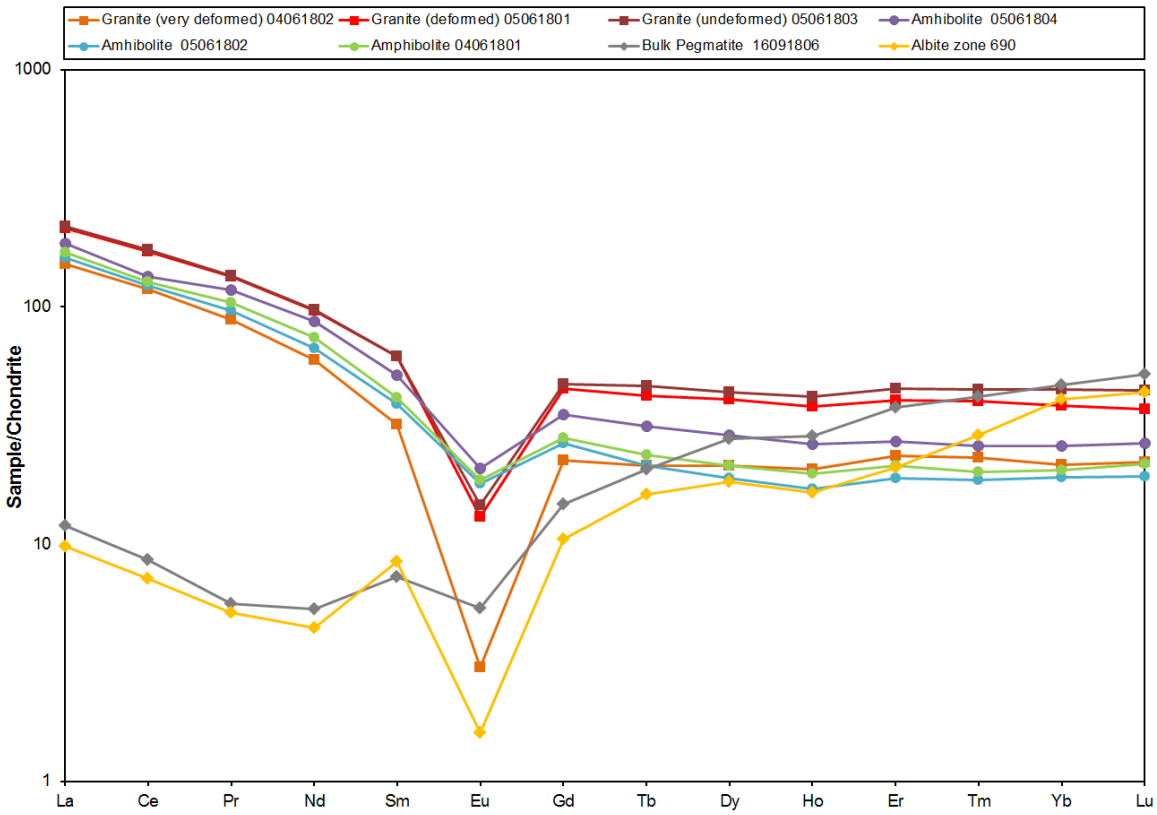

Fig 27. Chondrite-normalized REE pattern diagram adapted from Anders and Grevesse (1989).

4.4 Textures and chemistry of major and some accessory minerals of the Spro pegmatite

A major goal of this study consists in the characterization of the pegmatite mineralogy and paragenetic relationships to unveil and describe the pegmatite evolution. The textural and chemical characteristics of the pegmatite major and accessory minerals are key for the geochemical characterization of the Spro pegmatite. 1) Micas and alkali feldspars are common petrogenetic indicators of pegmatite evolution, and their geochemistry has been used to determine the history and evolution of pegmatite bodies (Neiva, 2013); 2) Per Soares *et al.* (2008) tourmaline major element chemistry and patterns may reflect magma differentiation and enrichment of incompatible elements; 3) And according to Slack and Trumbull (2011), B-isotope compositions in tourmaline have proven valuable in demonstrating the presence, relative timing of multiple fluid sources, as well as in the role of silicate melts and exsolved fluid(s) in pegmatite formation, zoning and mineralization (Trumbull *et al.*, 2013). Thus, the following section dives into the mineralogy and chemistry of the Spro pegmatite.

4.4.1 Feldspars

As a major constituent of granitic pegmatites, there are abundant feldspars throughout the studied area. The Spro pegmatite includes several feldspars (mainly k-feldspar) aggregates surpassing 1 meter in some regions. The most common is a K-feldspar with a pink coloration ranging from strong salmon pink to very light/faint nearly white coloration. There are also several albite aggregates and veins reaching ~20 cm in thickness, with a sugary white to pale white coloration which is very characteristic and distinguishable in the pegmatite. During fieldwork, several samples were collected and a total of 17 samples (placed in 3 casts) were analysed through EMPA as described in Section 3.5. Although most samples were found loose at the western shore of Nesodden, the samples 05061809, 05061810, 05061811, 05061812, 05061813 and 05061814 were collected from the mine cave, towards the pegmatite core as described in table 6.

Table 6. Textural characteristics of investigated feldspar samples.

Sample nr.	Cast nr.	Location	General texture	Classification	Distinctive chemical features
04061803	9	Loose	Dark salmon pink, coarse-grained	K-feldspar	Large spread, evolved
04061804	9	Loose	Light pink, coarse-grained	K-feldspar	Large spread, evolved
04061805	9	Loose	Very light/faint pink, coarse-grained	K-feldspar	Primitive
04061806	9	Loose	Whitish, coarse-grained	Albite	
04061807	9	Loose	White, coarse-grained	Oligoclase	
04061808	9	Loose	White, coarse-grained	Albite	
04061809	10	Loose	Vitreous white, medium grain	Albite (pure)	
04061810	10	Loose	Smoky white, coarser grain	K-feldspar	Evolved
04061811	10	Loose	Smoky white, coarser grain	Albite	
04061812	10	Loose	Smoky white, coarser grain	Albite (most pure)	
04061813	10	Loose	Sugary/vitreous white, medium grain with vivid orange garnet	Albite-Oligoclase, varied/spread	
05061809	10	Near core 10 cm from contact Cave western wall	Whitish, very coarse (>20 cm)	Albite-Oligoclase-Anorthoclase, most varied	
05061810	10	Near core 30 cm from contact Cave western wall (2nd hole)	Faint light pink, very coarse (>20 cm)	Oligoclase	
05061811	11	Near core 1 m from contact Cave western wall	Light pink, very coarse (>20 cm)	K-feldspar	Anomalous (primitive) point, primitive
05061812	11	Near core 1 m from contact Cave western wall	Whitish, very coarse (>20 cm)	Albite-Oligoclase	
05061813	11	By core Cave adjt side ceiling	Light pink, very coarse (>20 cm)	K-feldspar	Less spread, most evolved
05061814	11	By core Cave adjt side ceiling	Whitish, very coarse (>20 cm)	Albite (pure)	Less spread, most evolved

Feldspars are primary minerals used in igneous rocks classification due to their abundancy and wide range composition (Deer, W.A. *et al.*, 2001). Most feldspars are classified within the Ab-Or-An ternary system and are divided into alkali or potassium feldspars and plagioclase feldspars as shown in figure 28 (Deer, W.A. *et al.*, 2001). Proper characterisation of feldspars must also include analysis of its structure which gives insight into the crystallization conditions (Deer, W.A. *et al.*, 2001).

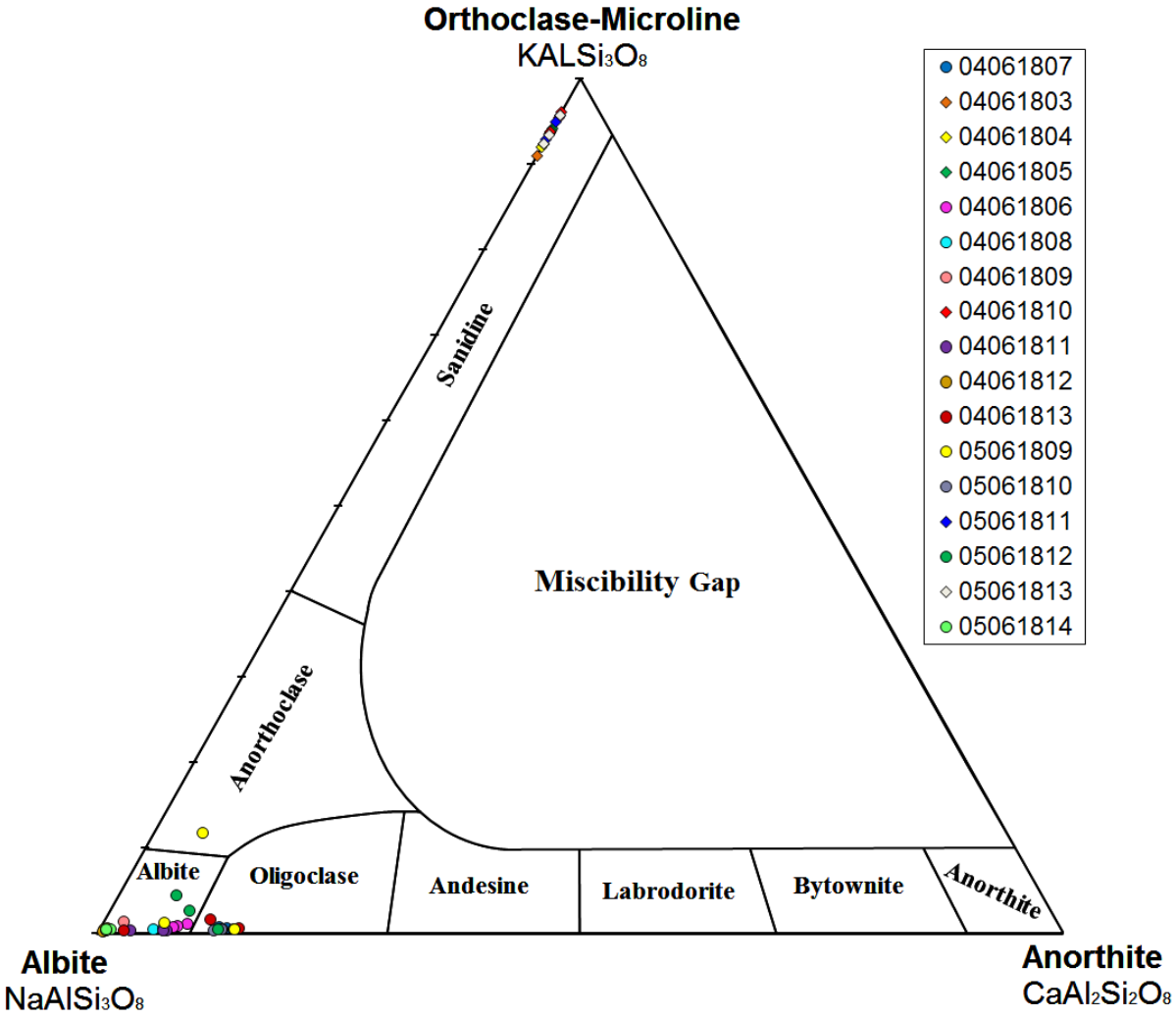

Fig 28. Feldspar An-Ab-Or discriminant diagram.

The Feldspars' data aquired from the EMPA as described in Section 3.5, converted to apfu and plotted in a Ab-An-Or classification ternary diagram. The diagram (Fig 28) indicates that samples 04061807, 04061806, 04061808, 04061809, 04061811, 04061812, 04061813, 05061809, 05061810, 05061812 and 05061814 are classified as Albite and Oligoclase. The samples 04061803, 04061804, 04061805, 04061810, 05061811 and 05061813 are classified as Orthoclase-Microline. The Ab-rich samples display greater variability and spread with sample 05061809 displaying extreme variability in particular. The Or-rich samples are all classified as sanidine and sit consistently between Ab_8-An_0-Or_{92} and $Ab_{3.8}$-An_0-$Or_{96.2}$. A more detailed view of the different feldspars is shown in Figs 29 and 30 while the full data results are presented in Appendix 8.8.

Table 7. Composition of feldspars from the Spro pegmatite acquired from EMPA. Data in parenthesis indicates double standard deviation. - = under detection limit.

Sample	**04061803**	**04061804**	**04061805**	**04061806**	**04061807**	**04061808**	**04061809**	**04061810**	**04061811**	**04061812**	**04061813**	**05061809**	**05061810**	**05061811**	**05061812**	**05061813**	**05061814**
n	**3**	**3**	**3**	**3**	**3**	**3**	**3**	**3**	**3**	**3**	**3**	**3**	**3**	**3**	**3**	**3**	**3**
SiO_2 (Wt%)	64.6(3)	65.0(7)	64.5(7)	66.7(3)	65.3(9)	67.1(5)	68(1)	64.5(3)	67(1)	69.0(2)	66(2)	65(2)	65.10(9)	64.5(6)	65.4(4)	64.8(4)	68.3(1)
Na_2O	0.8(1)	0.86(2)	0.67(4)	10.8(1)	10.39(6)	11.13(1)	11.6(1)	0.5(2)	11.1(4)	11.7(2)	10(1)	10(1)	10.4(1)	0.6(2)	10.3(1)	0.6(3)	11.85(5)
FeO	-	-	-	-	0.017(8)	0.02(2)	-	0.03(2)	0.01(1)	-	-	-	0.02(1)	-	-	-	0.006(6)
MnO	-	-	-	-	-	-	-	-	-	-	-	-	-	-	-	-	-
CaO	-	-	-	1.7(2)	2.8(3)	1.3(2)	0.2(2)	-	1.2(7)	0.12(4)	1(2)	1(1)	2.6(1)	-	1(1)	-	0.19(8)
Al_2O_3	18.43(8)	18.3(4)	18.4(1)	20.9(1)	21.8(2)	20.5(2)	19.8(2)	18.3(1)	20.5(5)	19.65(7)	21(1)	21(2)	21.5(2)	18.3(2)	21.5(2)	18.3(2)	19.57(7)
MgO	-	-	-	-	-	-	-	-	-	-	-	-	0.009(8)	-	-	-	-
K_2O	15.7(2)	15.7(3)	16.1(1)	0.18(6)	0.13(3)	0.10(2)	0.1(1)	16.2(2)	0.078(9)	0.09(4)	-	-	0.09(2)	16.0(2)	0.4(5)	15.9(4)	0.09(1)
Rb_2O	0.10(4)	0.08(7)	-	-	-	-	-	0.09(5)	-	-	-	-	-	-	-	0.10(1)	-
BaO	0.03(2)	-	-	-	-	-	-	0.04(2)	-	-	-	-	-	-	-	0.01(1)	-
P_2O_5	-	-	0.023(5)	0.01(1)	-	-	-	-	-	-	-	-	-	-	-	-	-
TiO_2	-	0.01(1)	-	-	-	-	-	-	-	-	0.01(1)	-	-	-	-	-	-
Total	99.66	99.95	99.59	100.29	100.43	100.15	99.7	99.66	99.88	100.56	98.01	97.01	99.71	99.40	98.6	99.71	100.00
Si (apfu)	2.99	2.99	2.98	2.91	2.86	2.93	2.97	2.99	2.93	2.99	2.90	2.87	2.87	2.99	2.88	2.99	2.98
Al	1.00	0.99	1.01	1.077	1.12	1.05	1.02	1.00	1.06	1.00	1.00	1.1	1.12	1.00	1.11	1.00	1.00
Na	0.07	0.08	0.06	0.92	0.88	0.94	0.98	0.04	0.94	0.99	0.90	0.8	0.89	0.05	0.88	0.06	1.00
Ca	-	-	-	0.08	0.13	0.06	0.01	-	0.05	0.01	0.09	0.08	0.12	-	0.08	-	0.01
K	0.93	0.92	0.95	0.01	0.01	0.02	0.01	0.96	0.00	0.01	0.01	0.04	0.01	0.95	0.02	0.93	0.01
Fe	-	-	-	-	-	-	-	-	-	-	-	-	-	-	-	-	-
Mn	-	-	-	-	-	-	-	-	-	-	-	-	-	-	-	-	-
Mg	-	-	-	-	-	-	-	-	-	-	-	-	-	-	-	-	-
Rb	-	-	-	-	-	-	-	-	-	-	-	-	-	-	-	-	-
Ba	-	-	-	-	-	-	-	-	-	-	-	-	-	-	-	-	-
P	-	-	-	-	-	-	-	-	-	-	-	-	-	-	-	-	-
Ti	-	-	-	-	-	-	-	-	-	-	-	-	-	-	-	-	-
An	0	0	0	8.03	13.05	6.22	1.32	0	5.66	0.58	9.22	8.43	12.37	0	8.81	0	0.89
Ab	7.22	7.70	5.98	90.98	86.23	93.22	97.82	4.82	93.91	98.92	89.81	86.99	87.10	5.40	88.58	6.08	98.60
Or	92.78	92.30	94.02	0.99	0.72	0.56	0.86	95.18	0.43	0.50	0.97	4.58	0.53	94.60	2.61	93.92	0.51

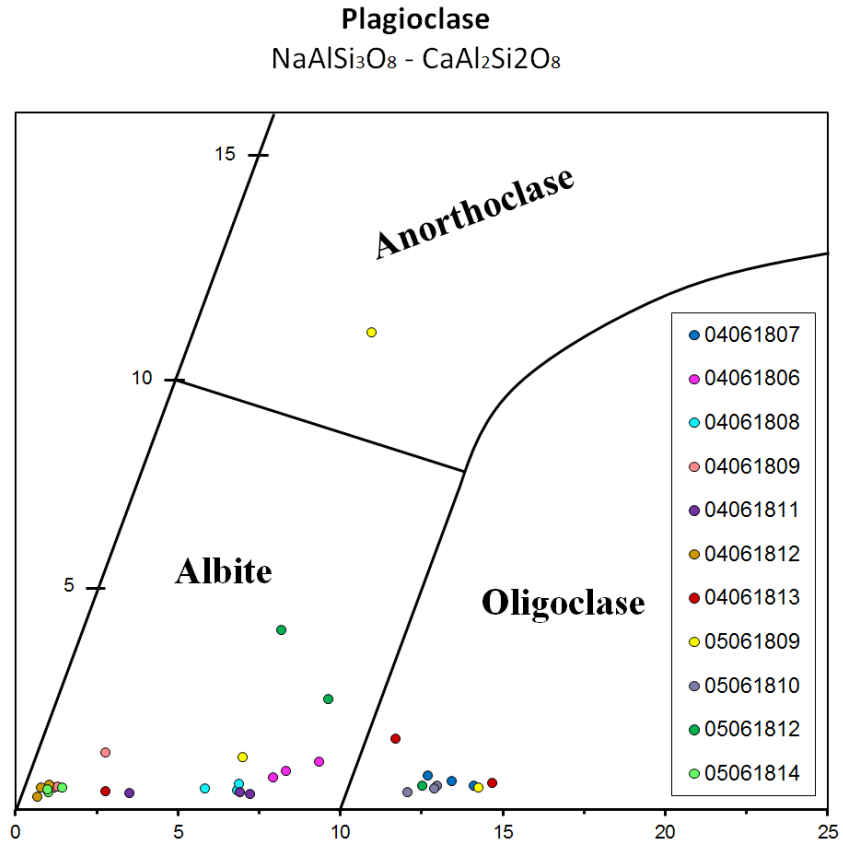

Fig 29. Plagioclase feldspar samples classification, from Fig 28.

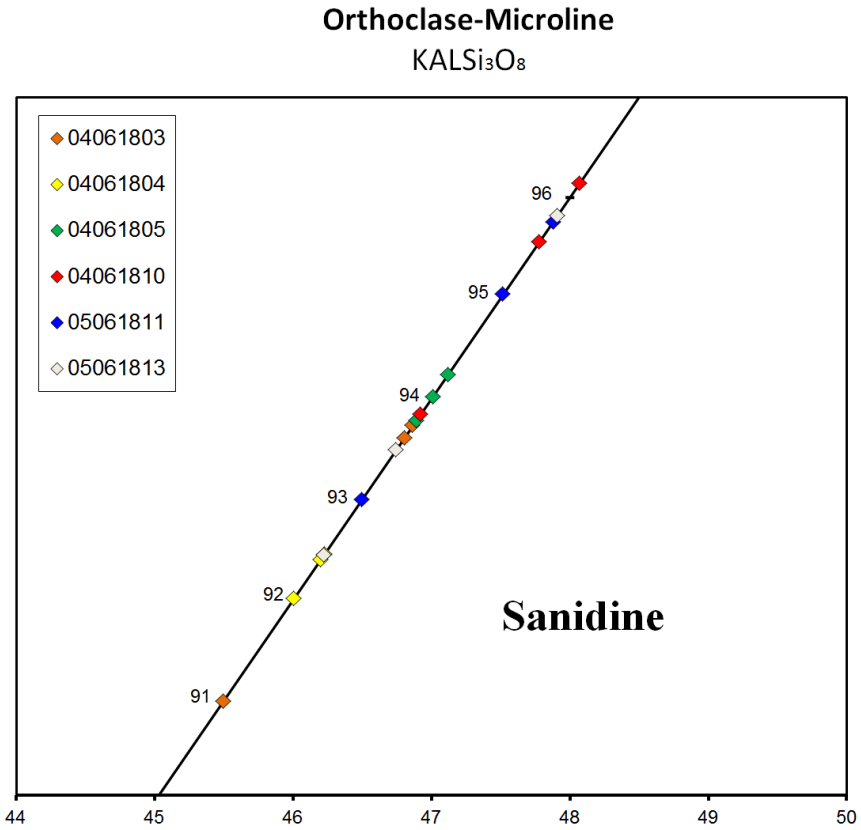

Fig 30. AlkalI feldspar samples classification, from Fig 28.

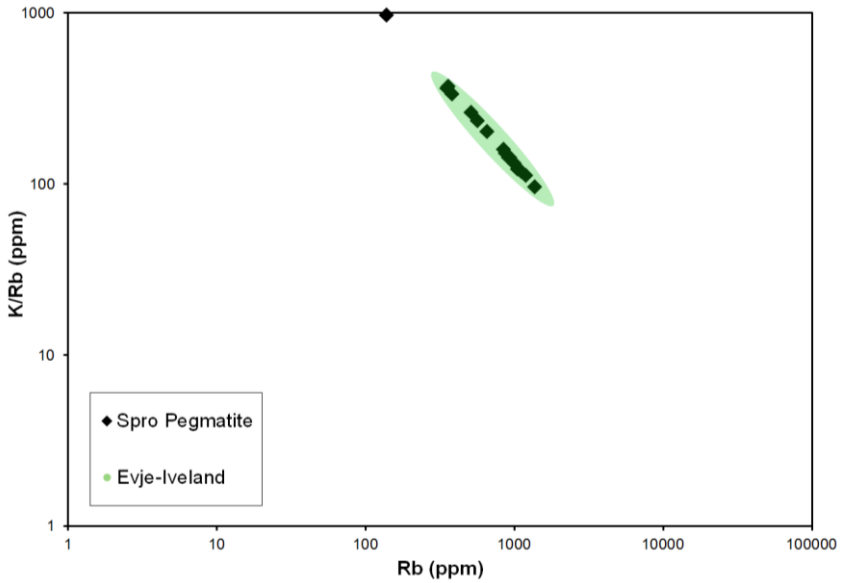

Fig 31. K/Rb ratio vs Rb in mica from Spro pegmatite (black points) and Evje-Iveland pegmatite field data (Green shade area) from Rosing-Schow *et al*., (2018).

To analyse how primitive the Spro pegmatite is, a K/Rb ratio vs Rb plot was used to evaluate the Spro pegmatite feldspars' fractionation as the ppm values were acquired through conversions from the EMPA data. The Spro data is plotted against literature data, in this case k-feldspars from the Evje-Iveland pegmatite. The plot (Fig 31.) indicates that the k-feldspars from the Spro pegmatite are quite similar to the ones found in the Evje-Iveland pegmatite in south Norway with the exception of an anomalous point in sample 05061811.

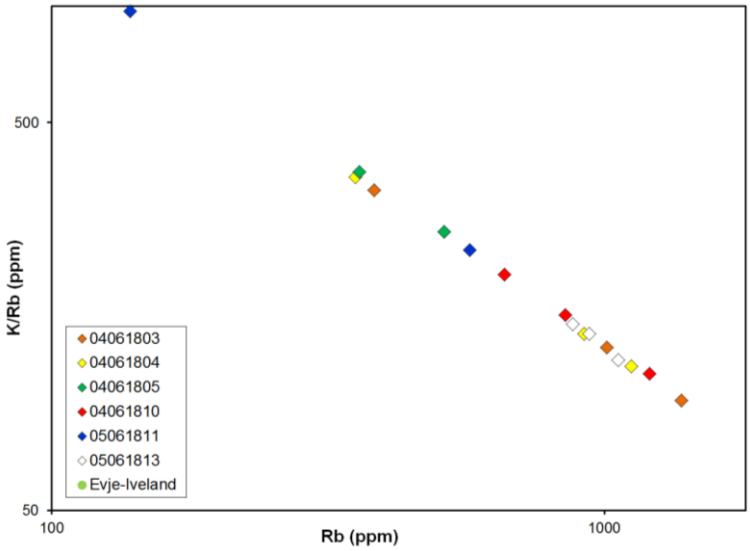

Fig 32. K/Rb ratio vs Rb plot as in Fig 31, only distinguishing the various Spro pegmatite feldspar samples.

Fig 32 displays the same data from Fig 31, only focused on the Spro pegmatite's k-feldspars. There were three-point analyses for each of the six identified k-feldspars within the Spro pegmatite samples. The K/Rb ratios range from 96 to 372 ppm and the Rb values from ~354 to ~1378 ppm with the exception of one point from sample 05061811 which display a much more primitive character. The samples show variability/spread and do not display clear evolution/fractionation trends. Samples 05061811 and 04061805 are the most primitive in average; while samples 05061813 and 04061810 are the most evolved; and samples 04061803 and 04061804 have the largest reach and display variable values.

4.4.2 Micas

Mica minerals represent one of the most abundant minerals in the Earth's crust (Melka, 2009) and the third most common component of granitic pegmatites, after feldspar and quartz (Černý & Burt, 1984) (Rosing-Schow *et al.*, 2018).

Micaceous minerals present great chemical variability due to their complex crystal structure as trioctahedral micas may incorporate a large number of elements of different ionic sizes and charges by a variety of isomorphic substitutions leading to a large and diverse mineral group (Tischendorf, 2001 & 2007).
Per Rieder *et al.*, The simplified formula can be written as **X Y**2-3 □ 1–0 **Z**4 **O**10 **W**2, where:
X is commonly Cs, K, Na, NH4, Rb, Ba, Ca;
Y is commonly Li, Fe (di- or trivalent), Mg, Mn(di- or trivalent), Zn, Al, Cr, V, Ti;
□ represents a vacancy;
Z is commonly Be, Al, B, Fe (trivalent), Si; and
W is commonly Cl, F, OH, O (oxy-micas), S.

Also according to Rieder *et al.*, (1998) the micas classification is based on the chemical composition and embodies generalizations derived from crystal-structure determinations as to the inclusion of physical determinative properties as classification criteria were avoided because these properties cannot unambiguously differentiate members of the micas.

Micas are important carriers of many minor and trace elements, including Li, F, Rb, Cs, Sn, Zn, Sc, Nb, Ta (Deer *et al.*, 2003), and thus their chemical composition is an important factor in classification and genesis studies of pegmatites as their chemistry and species are characteristic for different types of pegmatites and for different stages of the evolution of pegmatite melts (Černý & Burt 1984; Neiva, 2013, Marchal *et al.*, 2014) (Rosing-Schow *et al.*, 2018).

During fieldwork, several samples were collected and a total of 12 samples (placed in 3 casts) were analysed through EMPA. Most samples were collected from the loose mine remnants beach at the western shore of Nesodden, but samples 05061805, 05061806, 05061807 and 05061808 were collected from the western wall of the mine cave, towards the pegmatite core. The overall information and description of the mica's samples is presented in table 8.

Fig 33. Mica aggregates surrounding quartz.

Table 8. Textural characteristics of investigated mica samples.

Sample nr.	Cast nr.	Location	General texture	Associated Minerals	Classification	Distinctive chemical features
05061805	19	Near core (3rd) 10 cm from contact Cave western wall	Dark grey, large (>30cm) mica agglomerate	Quartz	Ferroan Muscovite	Quite primitive
05061806	19	Near core (2nd) 30 cm from contact Cave western wall (2nd hole)	Dark grey, large (>30cm) mica agglomerate	Quartz	Ferroan Muscovite	Quite primitive
05061807	19	Near core (1st) 1 m from contact Cave western wall	Dark grey, large (>30cm) mica agglomerate	Quartz	Ferroan Muscovite	2nd most evolved
05061808	19	By core Cave adjt side ceiling	Dark grey, large (>30cm) mica agglomerate	Quartz	Ferroan Muscovite	Most evolved
04061814	20	Loose	Dark olive green fine mica	-	Ferroan Muscovite	
04061815	20	Loose	Dark olive green fine mica	-	Ferroan Muscovite	
04061816	20	Loose	Wavy greenish and finer mica	-	Ferroan Muscovite	
04061818	20	Loose	Coarse yellowish mica	Albite	Ferroan Muscovite	
04061817	12	Loose	Coarse dark greyish-green mica	Albite	Ferroan Muscovite	
04061819	12	Loose	Fine yellow-green mica	Albite	Muscovite	Only Pure Muscovite Most Primitive
04061820	12	Loose	Dark grey coarse mica in albite vein 1	Albite and Fluorite	Ferroan Muscovite	
04061821	12	Loose	Dark grey coarse mica in albite vein 2	Albite and Fluorite	Ferroan Muscovite	

The Spro pegmatite exhibits many and large mica aggregates with a strong olive green to grey coloration easily recognisable at the former mine cave and at the quarry wall. The micas aggregates' dimensions can reach nearly 50 cm and display the common flaky morphology with flakes up to ~7 cm long. Many mica aggregates occur surrounding large quartz (see Fig 33).

The mica analyses from the Spro pegmatite are provided in Table 9 and the complete analysis list can be found in Appendix 8.9. The mica's mineral formula was calculated based on unpublished lecture notes from John Brady, Smith College MA, USA. Nomenclature follows the guidelines of Fleet *et al.*, (2003). The studied micas have 0.58 apfu Fe and 0.1 apfu Mg on average. Most samples are classified as Ferreous Muscovite with mgli average values of 0.11 and feal average values of -2.73, while the one exception, sample 04061819 which has 0.06 and -3.34 for mgli and feal content respectively and is classified as pure muscovite as shown in Fig 34.

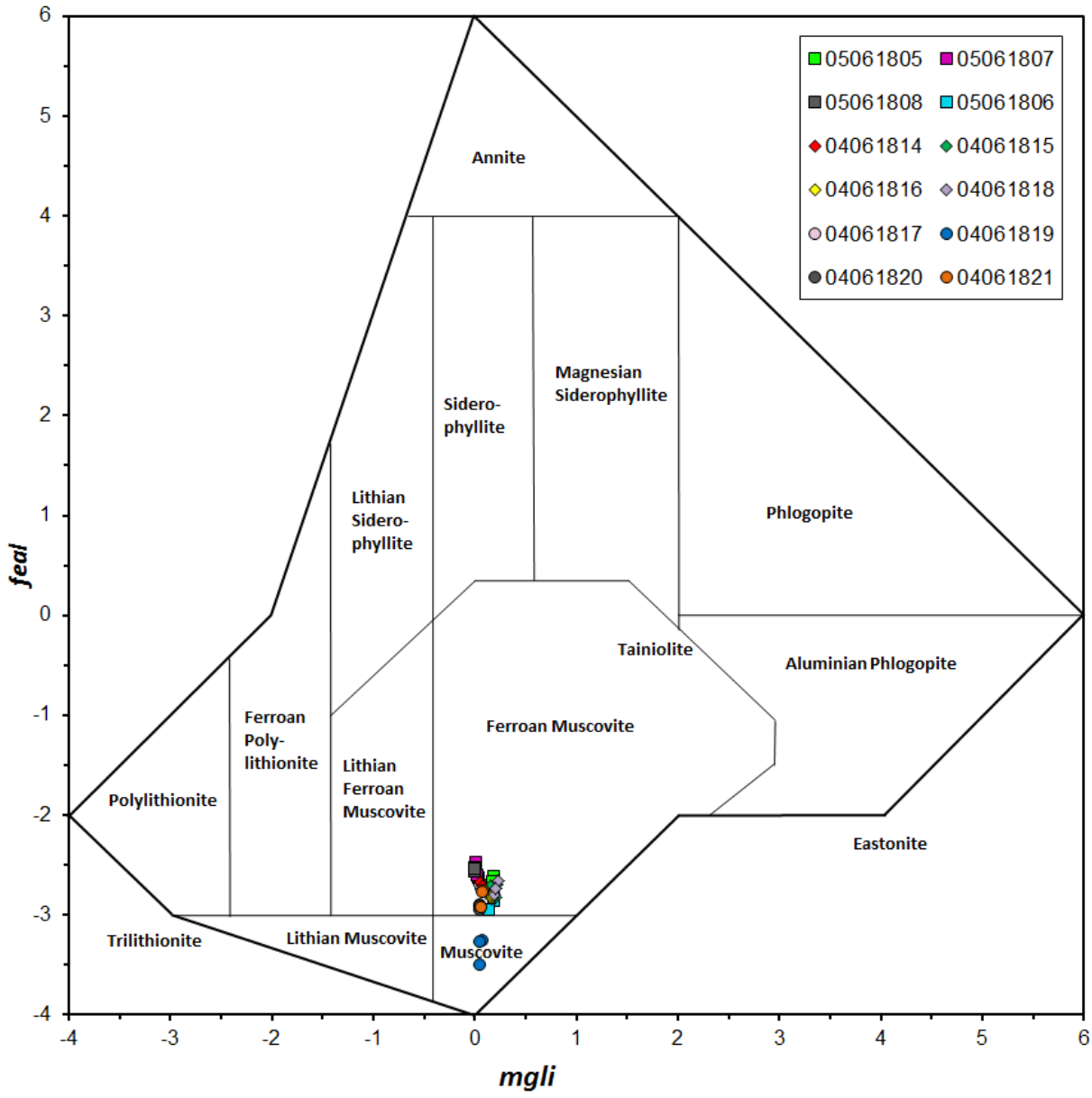

Fig 34. Mica classification diagram after Tischendorf *et al.* (2001). The Spro micas shown as squares were collected at the pegmatite cave wheres circles and diamonds were found as loose samples.

Table 9. Average EMPA results for the Spro pegmatite mica samples.

Sample	05061805	05061807	05061808	05061806	04061814	04061815	04061816	04061818	04061817	04061819	04061820	04061821
Location	Contact	Core	Core	Contact	Loose	Loose	Loose	Loose	Loose	Loose	Loose	Loose
n	3	3	3	3	3	3	3	3	3	3	3	3
SiO_2 (wt%)	46.1(5)	45.7(1)	45.7(4)	46.5(3)	46(1)	46.6(3)	46.2(2)	46.3(5)	46.3(4)	46.6(4)	46.7(2)	46.2(3)
FeO	5.0(2)	6.3(6)	6.3(2)	4(1)	5.7(2)	4.9(4)	4.7(2)	4.8(1)	5.7(1)	2.9(9)	4.7(1)	5.2(3)
MnO	0.06(2)	0.1(1)	0.23(7)	0.07(2)	0.08(2)	0.06(2)	0.05(1)	0.04(2)	0.08(0)	0.04(2)	0.11(8)	0.07(2)
CaO	-	-	-	-	-	-	-	-	-	-	-	-
Al_2O_3	30.3(4)	30.4(2)	30.3(1)	31.0(9)	30.5(1)	30.5(8)	31.1(2)	30.3(8)	30.7(3)	33(1)	31.6(2)	30.8(5)
MgO	0.91(6)	0.13(7)	0.03(2)	0.8(2)	0.3(1)	0.9(2)	0.80(3)	1.0(1)	0.32(6)	0.2(1)	0.26(3)	0.40(7)
Cl	-	0.02(1)	0.01(0)	-	-	-	0.02(1)	0.01(1)	-	-	-	0.01(0)
K_2O	10.4(6)	10.4(3)	10.3(5)	10.9(1)	10.6(1)	10.7(4)	10.7(1)	10.6(4)	9.8(2)	10.4(1)	10.3(1)	9.6(5)
TiO_2	0.58(9)	0.14(0)	0.17(2)	0.5(3)	0.12(1)	0.17(9)	0.15(1)	0.2(2)	0.22(4)	-	0.11(2)	-
F	0.24(6)	0.6(1)	0.5(4)	0.2(2)	0.48(5)	0.3(1)	0.4(1)	0.4(1)	0.4(1)	0.16(4)	1.4(2)	1.1(4)
Na_2O	0.24(6)	0.4(1)	0.4(1)	0.2(1)	0.38(5)	0.34(7)	0.3(1)	0.24(5)	0.17(7)	0.09(3)	0.30(2)	0.16(5)
Sc_2O_3	0.01(1)	0.01(1)	-	-	-	-	-	0.01(1)	-	-	-	-
Rb_2O	0.12(5)	0.23(1)	0.23(1)	0.13(4)	0.20(2)	0.24(2)	0.20(5)	0.1(1)	0.14(9)	-	0.10(6)	0.1(1)
Cs_2O	-	0.04(1)	0.04(1)	-	0.07(7)	0.06(2)	-	-	-	-	-	0.04(3)
H_2O*	4.23(7)	4.01(7)	4.0(1)	4.2(1)	4.12(8)	4.2(1)	4.17(7)	4.15(3)	4.15(9)	4.36(4)	3.7(1)	3.8(1)
-O=F	0.10(3)	0.26(4)	0.2(1)	-	0.20(2)	0.15(6)	0.17(5)	0.17(7)	0.17(5)	0.07(2)	0.5(1)	0.4(1)
Total	98.29	98.74	98.41	98.50	98.75	99.12	98.96	98.32	98.15	97.82	99.78	97.88
Si (apfu)	6.37	6.36	6.36	6.37	6.41	6.40	6.35	6.40	6.40	6.31	6.39	6.41
Al	1.63	1.64	1.64	1.63	1.59	1.60	1.65	1.60	1.60	1.69	1.61	1.59
Z	8.00	8.00	8.00	8.00	8.00	8.00	8.00	8.00	8.00	8.00	8.00	8.00
Al	3.30	3.34	3.34	3.38	3.37	3.33	3.38	3.33	3.41	3.68	3.49	3.45
Ti	0.06	0.01	0.02	0.05	0.01	0.02	0.02	0.03	0.02	-	0.01	0.02
Fe	0.58	0.74	0.74	0.46	0.66	0.57	0.54	0.56	0.67	0.33	0.54	0.61
Mn	0.01	0.02	0.03	0.01	0.01	0.01	0.01	-	0.01	-	0.01	0.01
Mg	0.19	0.03	0.01	0.17	0.06	0.19	0.16	0.21	0.07	0.06	0.05	0.08
Y	4.14	4.13	4.14	4.07	4.11	4.11	4.11	4.13	4.17	4.08	4.10	4.16
Na	0.07	0.11	0.12	0.07	0.10	0.09	0.10	0.06	0.05	0.02	0.08	0.04
Ca	-	-	-	-	-	-	-	-	-	-	-	-
K	1.8	1.86	1.84	1.91	1.87	1.88	1.89	1.88	1.74	1.81	1.80	1.71
Rb	0.01	0.02	0.02	0.01	0.02	0.02	0.02	0.02	0.01	-	0.01	0.01
Cs	-	-	-	-	-	-	-	-	-	-	-	-
Sc	-	-	-	-	-	-	-	-	-	-	-	-
X	1.90	1.99	1.99	2.00	1.99	2.00	2.01	1.96	1.80	1.84	1.89	1.77
F	0.11	0.27	0.23	0.10	0.21	0.15	0.17	1.18	0.18	0.07	0.60	0.48
Cl	-	0.01	-	-	-	-	-	-	-	-	-	-
OH	3.89	3.72	3.77	3.90	3.79	3.85	3.82	3.82	3.82	3.93	3.40	3.52
W	4.00	4.00	4.00	4.00	4.00	4.00	4.00	4.00	4.00	4.00	4.00	4.00
mgli	0.19	0.03	0.01	0.17	0.06	0.19	0.16	0.21	0.07	0.06	0.05	0.08
feal	-2.66	-2.58	-2.55	-2.86	-2.69	-2.74	-2.82	-2.73	-2.71	-3.34	-2.92	-2.82

* H_2O: the H_2O is estimated by fully occupying the F–OH site;.- = under detection limit; Data in parenthesis indicates double standard deviation.

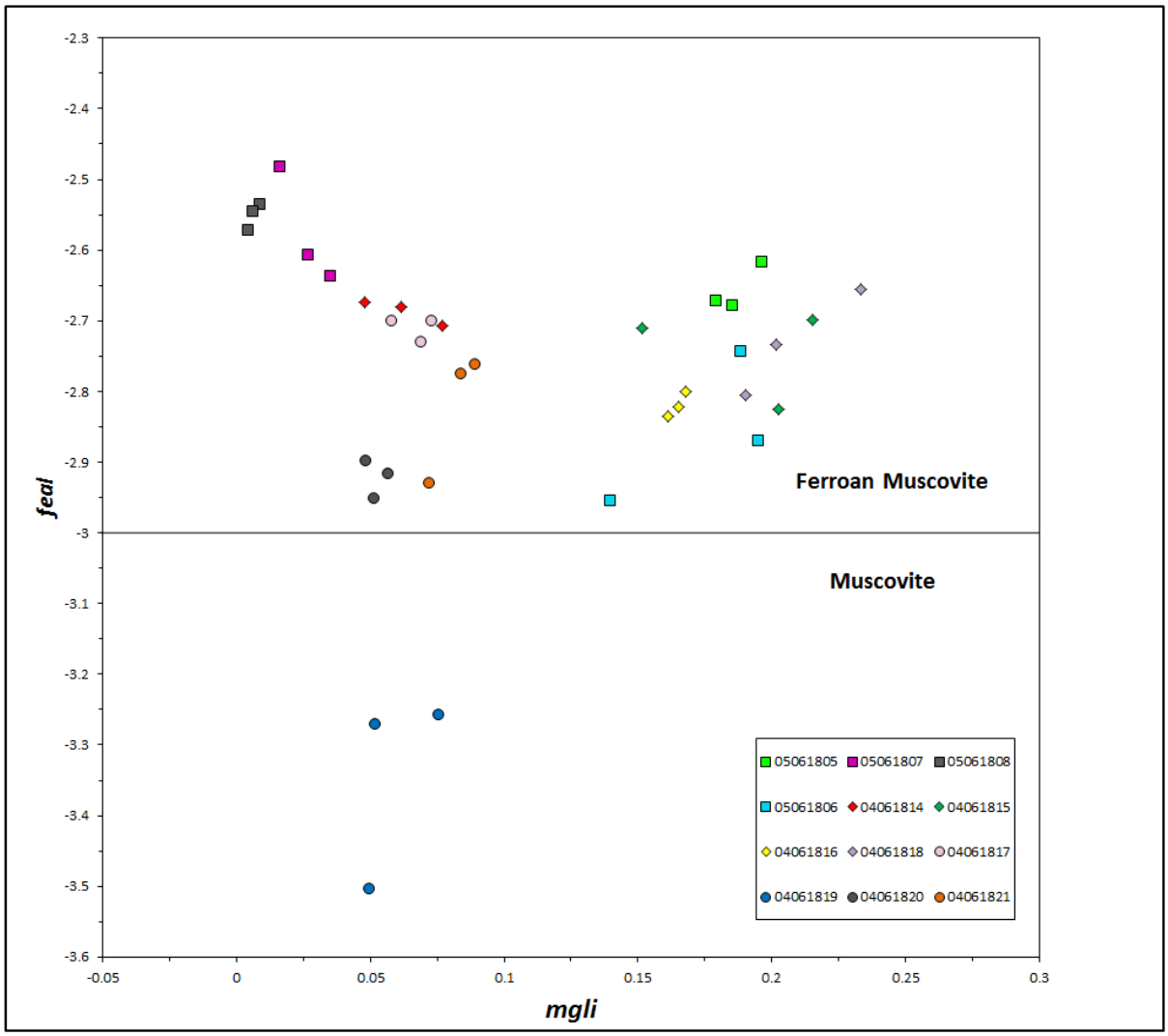

Fig 35. Chemical classification of micas from the Spro Pegmatite plotted according to Tischendorf *et al.*, (2001); Detailed view of Fig 34.

The overall element contents are fairly similar throughout the mica samples, only displaying subtle differences. The Ti content is generally low (0.01 to 0.03 apfu) and similar for most analyses except samples 05061805 and 5061806 having the highest values of 0.6 and 0.5 apfu, respectively. The Fe content is also quite constant above 0.45 apfu for all samples with the exception of sample 04061819 which has a Fe content of 0.3335 apfu. The Mn contents also cluster throughout the samples with the exception of samples 05061807 and 05061808 with values of 0.0161 and 0.0277 apfu respectively. All other samples have Mn contents below 0.0125 apfu. The Mg content is one of the most variable throughout the analysis and can be divided into three groups: 1) Mg content below 0.03 apfu on samples 05061807 and 05061808 especially with a content of 0.0063; 2) Mg content between 0.05 and 0.085 apfu for five samples; and 3) Mg content above 0.16 also for five samples where sample 04061818 displays the highest content with 0.2085 apfu. The Na content also displays variability with the lowest values recorded on sample 04061820 with 0.024 apfu while the highest content is nearly 0.12 apfu found on sample 05061808. The F content is fairly constant between 0.1 and 0.3 apfu while sample 04061819 displays the lowest F content just below 0.07 apfu and samples 04061820 and 04061821 record the highest F contents with 0.6 and 0.5 apfu respectively. The EMPA data averages for each sample can be found on Table 9 while the full analysis data is displayed on Appendix 8.9.

Many plots were created from the acquired EMPA data to further investigate the distinctive features and chemical characteristics between the various micas from the Spro pegmatite. In addition, these data was plotted along with literature data to compare the micas from Spro and other Sveconorwegian pegmatites.

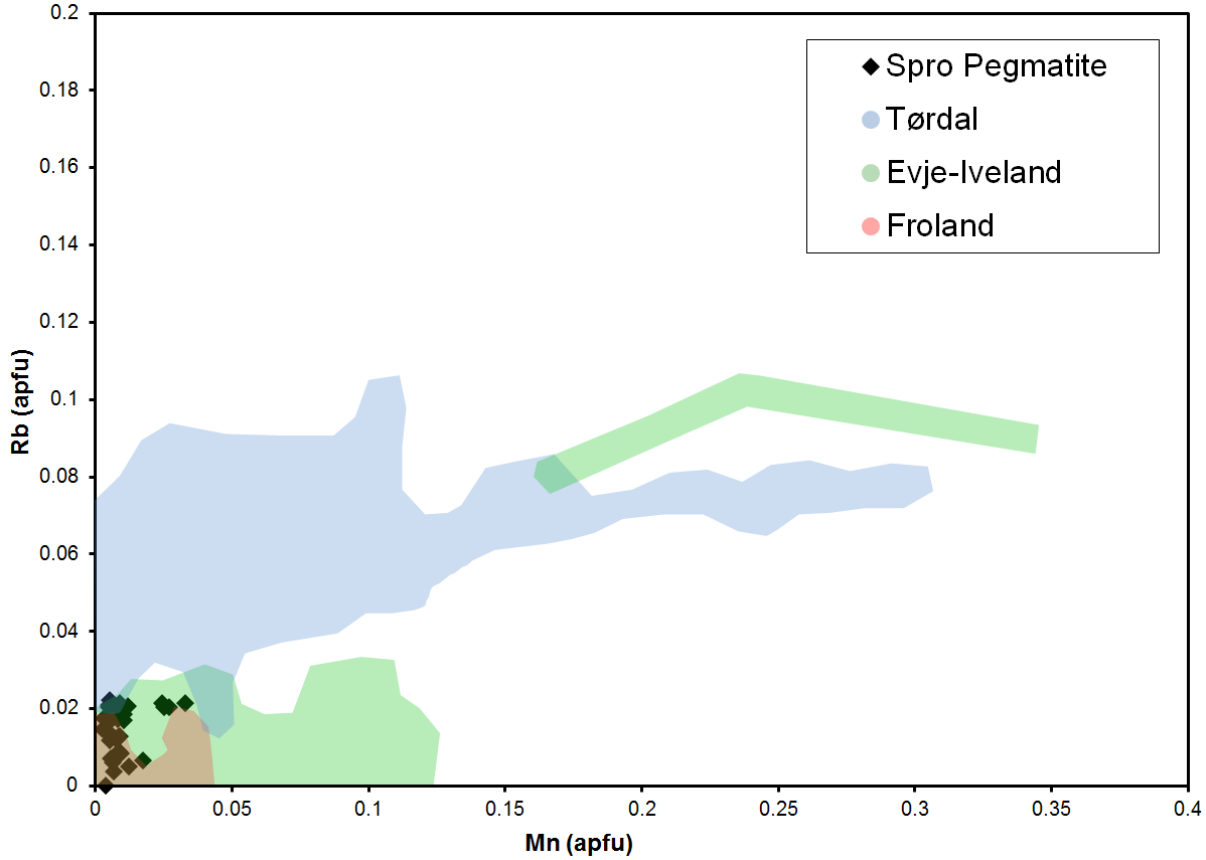

Fig 36. Rb and Mn content of the micas from the Spro pegmatite (black points) in comparison to mica data from Tørdal pegmatite field (blue shade area), Evje-Iveland pegmatite field (green shade area) and Froland pegmatite field (red shade area) from Rosing-Schow *et al*., (2018).

The Rb vs Mn apfu plot shows that the Spro pegmatite micas are both Rb and Mn poor compared to micas from other Sveconorwegian pegmatites (reference), with Rb values ranging between 0 and 0.02 apfu and Mn values ranging from 0.0 to 0.03 apfu. These values are much smaller than the Evje-Iveland and Tørdal pegmatites' which both surpass 0.10 apfu concentrations for Rb and 0.30 apfu for Mn given by Rosing-Schow *et al*., (2018). The Froland pegmatite values are the closest to the Spro pegmatites' as seen in Fig 36 with Rb and Mn values below 0.02 and 0.05 apfu respectively.

The data from the micas suggests that the Froland pegmatite is the most primitive, followed by the Spro while the Tørdal and Evje-Iveland pegmatites are significantly more evolved.

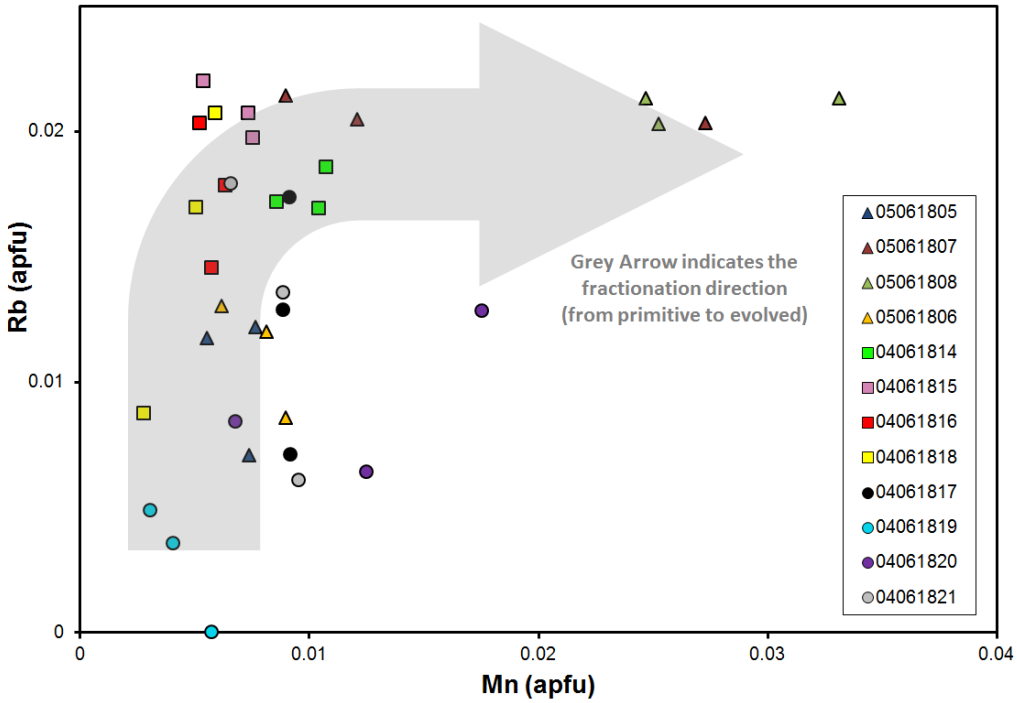

Fig 37. Rb and Mn content as in fig 36. focused on the Spro pegmatite mica samples, displaying the fractionation evolution of the Spro micas.

Fig 37 displays the same data as Fig 36 only focused on the Spro pegmatite micas. The data shows that sample 04061819 (previously classified as the only pure muscovite as shown in Fig 35) is the most primitive mica. The micas collected from the mine cave (05061805, 05061807, 05061808 and 05061806) include the two most evolved micas, samples 05061808 and 05061807 respectively. The other two micas from the cave (samples 05061805 and 05061806) display similar Rb and Mn concentrations and sit along the primitive micas.

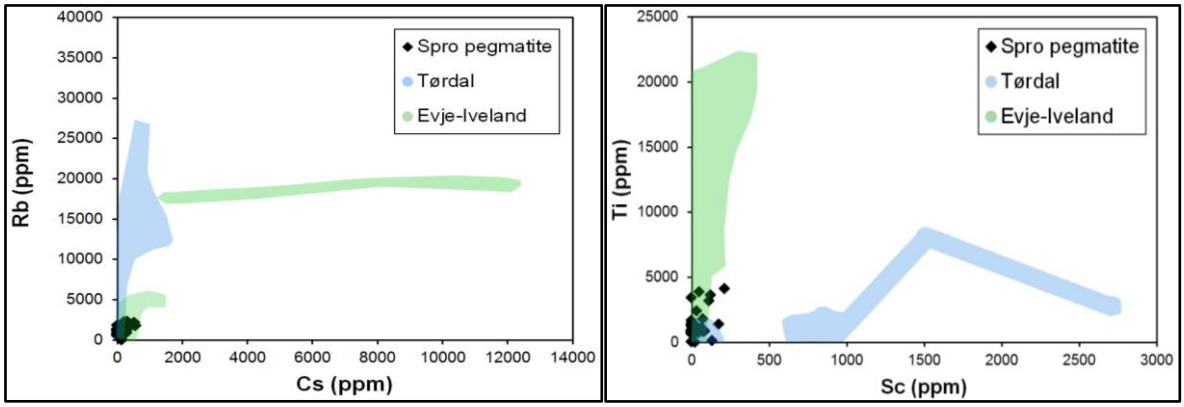

Figs 38 and 39. Rb, Cs, Ti and Sc content of the micas from the Spro pegmatite (black points) in comparison to mica data from Tørdal pegmatite field (blue shade area) and Evje-Iveland pegmatite field (green shade area) and from Rosing-Schow *et al*., (2018).

The plots from Figs 38 and 39 indicate that the Spro pegmatite micas are Rb, Cs, Ti and Sc poor with ppm concentrations ranging from 0 to 2292.4, 548.0, 4116.8 and 211.8 ppm respectively. Evje-Iveland and Tørdal micas are then significantly more enriched in all Rb, Cs, Ti and Sc than the Spro pegmatite. The Evje-Iveland micas are most enriched in Cs and Ti while the Tørdal micas are most enriched in Rb and Sc. The ppm values were acquired through conversions from the EMPA data.

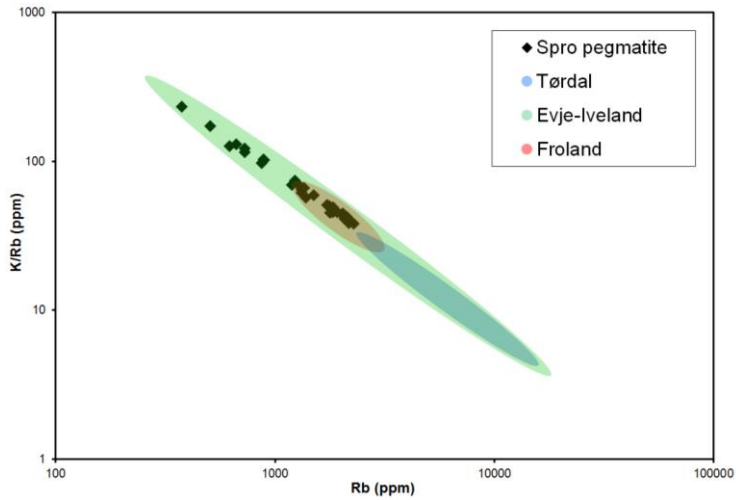

Fig 40. K/Rb ratio vs Rb in mica from Spro pegmatite (black points in comparison to mica data from Tørdal pegmatite field (blue shade area), Evje-Iveland pegmatite field (green shade area) and Froland pegmatite field (red shade area) from Rosing-Schow *et al.*, (2018).

Similarly to the feldspars, a K/Rb ratio vs Rb plot was used to evaluate the micas fractionation level. The ppm values are calculated from the oxides wt.% measurements acquired by EMPA. The Spro pegmatite micas data was plotted against data found in the literature from also Sveconorwegian pegmatites in Tørdal, Eavje-Iveland and Froland. The data indicates that the Froland pegmatite is the most primitive and has the smallest spread. The Tørdal is more evolved with a large spread and the Eavje-Iveland is the most evolved and has the highest spread.

The plot results show Spro micas' K/Rb ratios (ppm) ranging from 239,7 to 39,4 which in comparison to other mica analysis is closer to the Froland pegmatites which has K/Rb rations ranging from 85 to 23. In addition, the Spro pegmatite displays a spread similar to the Tørdal pegmatite (only more primitive with larger ratios) and smaller than the Evje-Iveland pegmatite which has the largest spread.

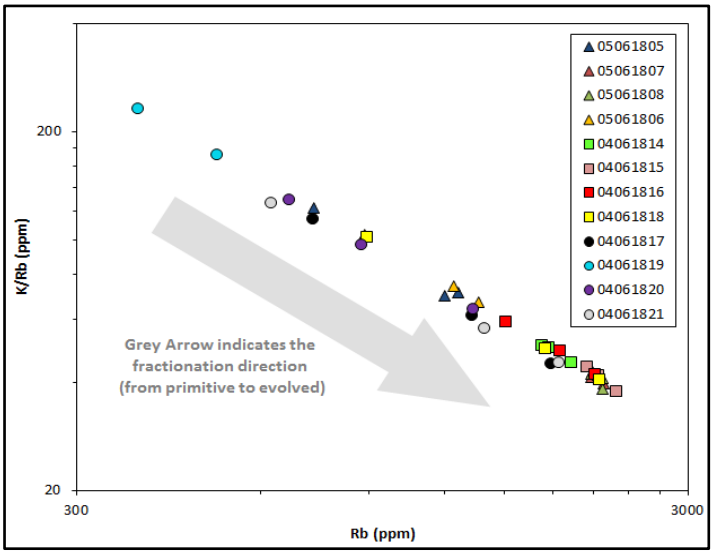

Fig 41. K/Rb ratio vs Rb as in fig 40 focused on the Spro pegmatite mica samples.

Fig 41 displays the same data of fig 40 focused on the analysed Spro pegmatite samples. The plot reinforces the results observed in fig 35 and points sample 04061819 as the most primitive mica and the samples 04061815, 05061807 and 05061808 as the most evolved.

4.4.3 Tourmaline

The black tourmalines occurring in the Spro pegmatite present variable morphology, size and inclusion inventory. However, all tourmalines have one thing in common; they are always spatially associated with sugary albite, greenish muscovite, and sometimes topaz, beryl, and fluorite. This mineral paragenesis commonly forms vein-like structures that crosscut and partially replace already solidified parts of the major pegmatite body suggesting that these minerals formed last. Within these vein-like structures tourmaline crystals are commonly aligned. The tourmalines vary in size from <1 mm to 5 cm and exhibit mostly subhedral textural types, mostly due to fragmentation of former euhedral crystals due to melt movement. Perpendicular to the *c*-axis, the Spro tourmalines usually display a "rounded-triangular" shape while when seen parallel to the *c*-axis they are in elongated, tabular or columnar needle-like shapes. For this study we collected different textural types of tourmalines from the Spro pegmatite in order to study if there is also a chemical variation among them. We included one sample from the mineral collection of the Natural History Museum of Oslo (20160), four samples collected by the former curator of the NHM mineral collection Gunnar Raade (690a, 690b, 690c) and one collected by Axel Müller during previous fieldwork (18081715). These samples are described more in detail as follows (see Table 10) applying optical microscopy and scanning electron microscopy.

Table 10. Textural characteristics of investigated tourmaline samples.

Sample number	**General texture**	**Tourmaline size**	**Colour in hand specimen**	**Colour in optical microscopy**	**Inclusion inventory**	**Distinctive chemical features**
690a	Fractured segment of a larger crystal	3 cm in length and 2 cm in diameter	black	Dark blue, lighter at the edges	Fluorite, muscovite, pyrite, quartz	Highest Na and Fe Lowest Ti
690b	Aligned, fractured needle-like crystals occurring aggregates	up to 2 cm in length, 0.5-2 mm in diameter	Black	Dark blue, lighter at the edges	Muscovite, fluorite, quartz, ferrosillite, xenotime-(Y), monazite-(Ce), Unidentified Nb-oxide	Lowest Fe and Na
690c	Aligned, fractured fine-grained needle-like tourmaline mass with sugary albite matrix forming a vein-like structure	Up to 5 mm in length	Black	Dark blue	Zircon, fluorite, muscovite, albite, apatite, Almandine garnet, quartz, Bastnäsite-(Ce)-group, microlite group, Kanosite-(Y), Pb-oxide, Pb-sulfide (galena), pyrochlore group, betafite group	Highest Mg, Ca,Na and Ti Lowest F Zoned Ti and Mg
20160	Large crystal fragments embedded in quartz and sugary albite forming a vein-like structure	Up to 2 cm in size	Black	Dark blue, lighter at the edges	Fluorite, pyrite, muscovite, quartz, iron-oxide, xenotime-(Y)	Lowest Ti
18081715	Clusters of euhedral wedge-shaped crystals embedded in a sugary albite vein	Up to 1 cm in length	Dark olive green	Dark blue	Zircon, albite, muscovite, quartz, sphalerie, rutile, fluorite, Euxenite-(Y), Bastnäsite-(Ce)-group, Kanosite-(Y), Thorite family	Lowest Mg Zoned Fe, Mn and Li

690a

This sample consists in a single, large (~1.5 cm - diameter) tourmaline crystal mostly surrounded by quartz, next to light green muscovite and dominant K-feldspar.

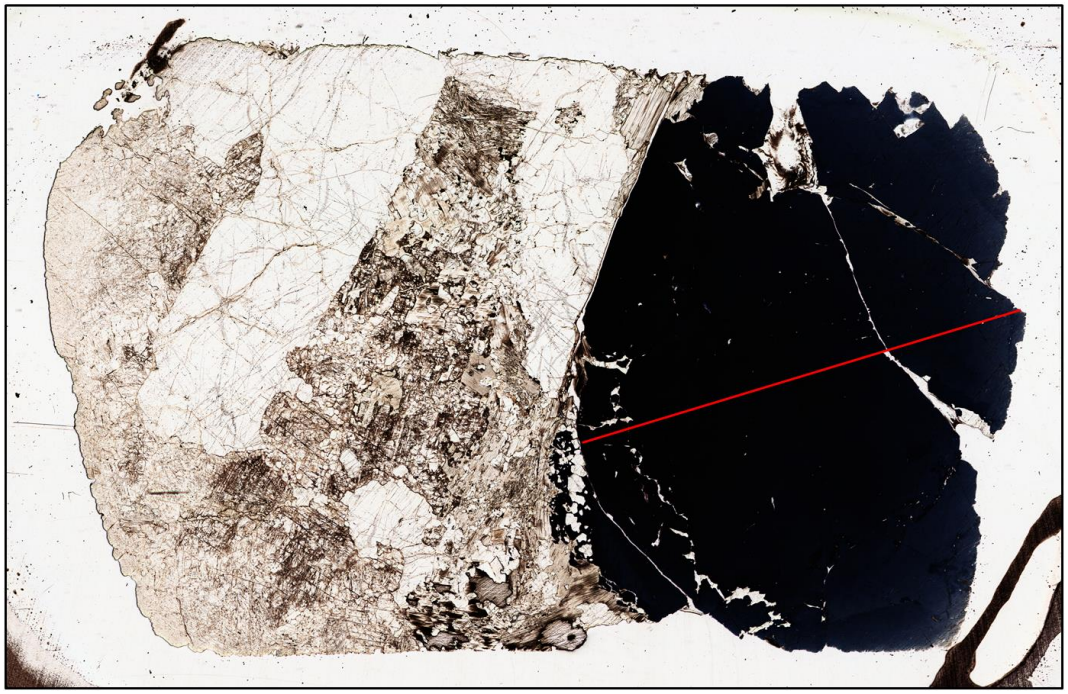

Fig 42. Tourmaline sample 690a thin section scan. Red line indicates the profile targeted for EMPA.

The outermost growth zone contains drop-like quartz micro inclusions (~20 µm). Quartz is also present in the tourmaline crystal through fractures along with fluorite as shown in Fig 43. Fluorite is the major inclusion and besides occurring in fractures it also occurs commonly as micro inclusions throughout the tourmaline, and in both large and small cracks (from <10 µm to ~50 µm). The colour of the tourmaline in the hand specimen in a lustery black and is dark blue (almost black) but lighter towards the edge in thin section. The muscovite flakes, which fill the interstices of K-feldspar, seem to be partially replaced by K-feldspar (The opposite is usually the case).

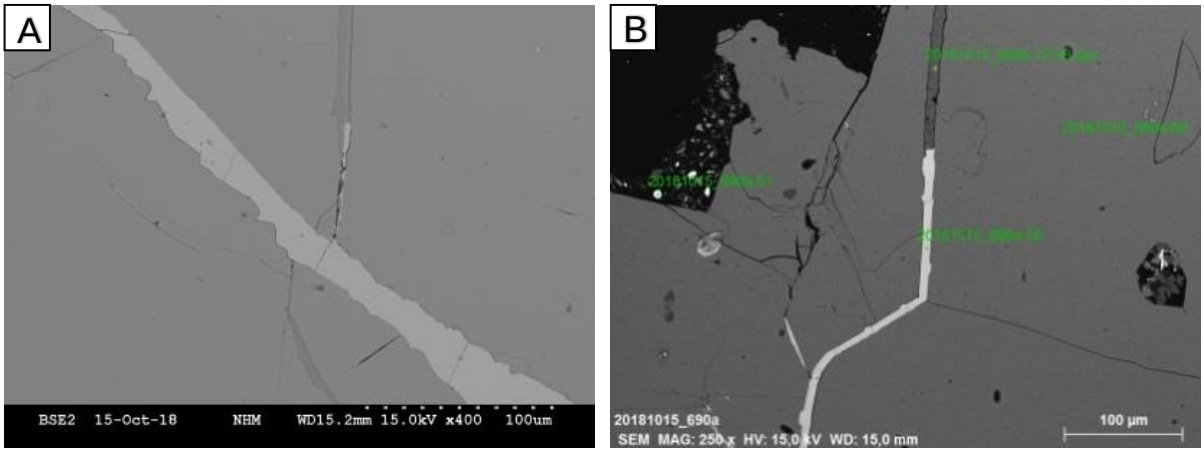

Fig 43. Tourmaline inclusions in sample 690a. A) Fluorite inclusions inside fracture; B) Fluorite and quartz inclusions inside fracture.

690b

This sample contains various tourmalines occurring in corridors within albite veins surrounded by quartz, K-feldspar and some muscovite. The tourmalines exhibit a tabular shape in the hand specimen but appear mostly as large triangular euhedral prisms in thin section, because they are aligned and cut perpendicular to the *c*-axis. There are also present tabular elongated prismatic crystals horizontally orientated displaying lighter colour and dense aggregates of tiny minerals prisms. There are a few topaz occurrences as fractured and included grains in the thin section.

Fig 44. Tourmaline sample 690b thin section scan. Red lines indicate the profiles targeted for EMPA.

The tourmalines in this sample contain fluorite inclusions (from <20 µm to ~60 µm) filling up micro cracks (as point 6 in Fig 45-A) and cavities within or around the tourmaline crystals and large (>500 µm) fluorite grains. There are some rare-earth minerals (e.g. xenotime-(Y), monazite-(Ce)) found as inclusions in both tourmaline and quartz , while the main inclusions, abundant throughout the sample consist in fluorite. The sample also contains three large fluorite grains with dimensions over 500 µm (Fig 45-B). In addition the sample also contains three fractured topaz grains with abundant muscovite, quartz and fluorite inclusions.

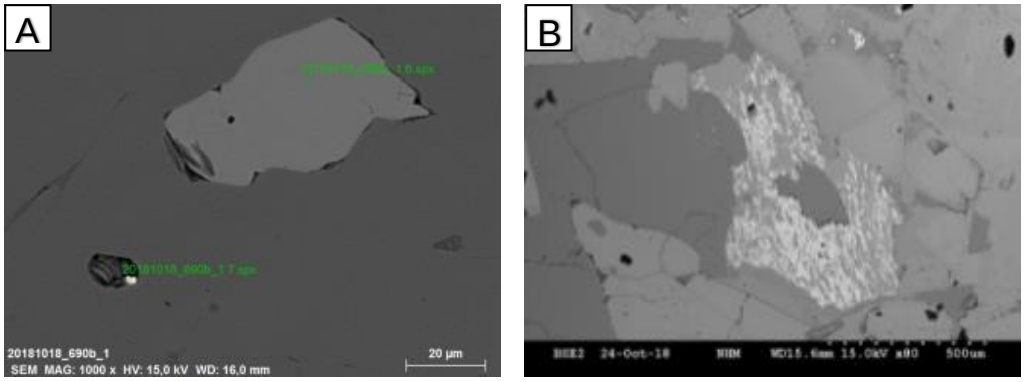

Fig 45. Tourmaline inclusions in sample 690b. A) Fluorite micro inclusions inside crack; B) Large fluorite aggregate.

690c

The hand specimen sample contains fine grained tourmalines forming tiny crystals and few tabular elongated (up to 2.5 cm) aggregated within fine-grained (sugary) albite veins, right next and parallel to a 1 to 2 cm wide muscovite band. Despite tourmaline, albite and muscovite being the most abundant minerals, the hand specimen also contains quartz and a 1 cm large fluorite crystal. The thin section comprises three corridors with dense aggregates of tiny (50-100 µm) "rounded-triangular" tourmalines, some large (reaching 2.5 mm) very included crystals and a few tabular, elongated crystals parallel to the c-axis. The tourmalines are surrounded by an albite vein, muscovite and a ~1.5 cm k-feldspar grain.

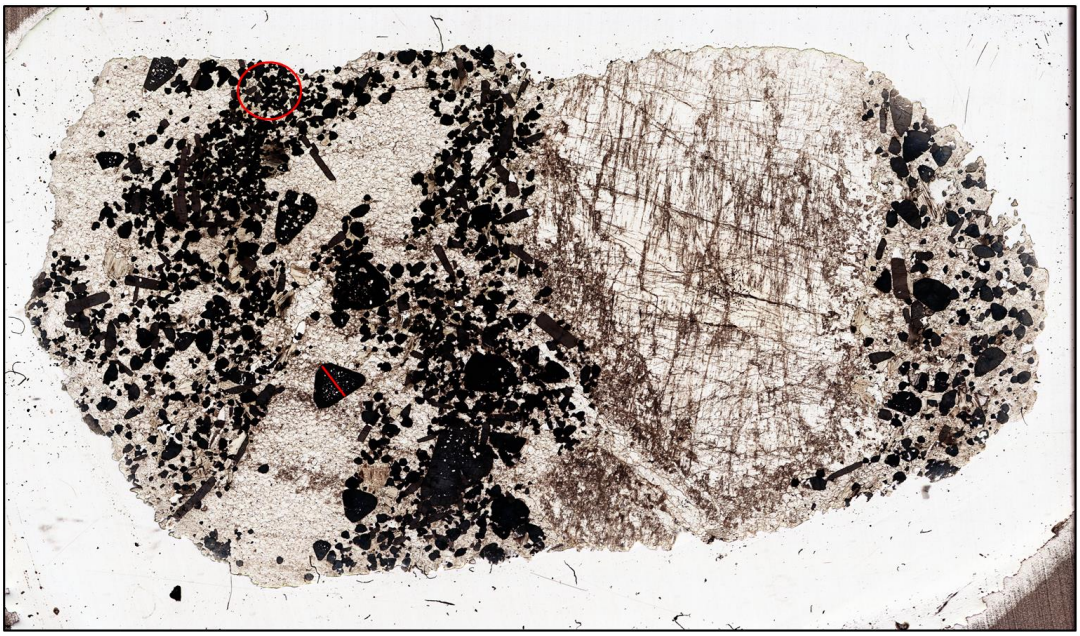

Fig 46. Tourmaline sample 690b thin section scan. Red lines indicate the profiles and cluster targeted for EMPA.

The larger inclusions (up to ~250 µm) consist mostly of zircon, albite and mica. The zircon crystals (as seen in Fig 47-B) range in dimensions form <5 µm to nearly 70 µm and there is also an aggregate with dimensions up to 250 µm. The zircon crystals grow mostly inside apparent cavities within or around the tourmalines and feldspars usually 'connected' by cracks or fractures. In addition, almandine and Pb-sulfide (galena) inclusions shown in are also found within the tourmaline crystals. There is also a wider and more diverse array of REE inclusions throughout the many tourmalines (see table 10).

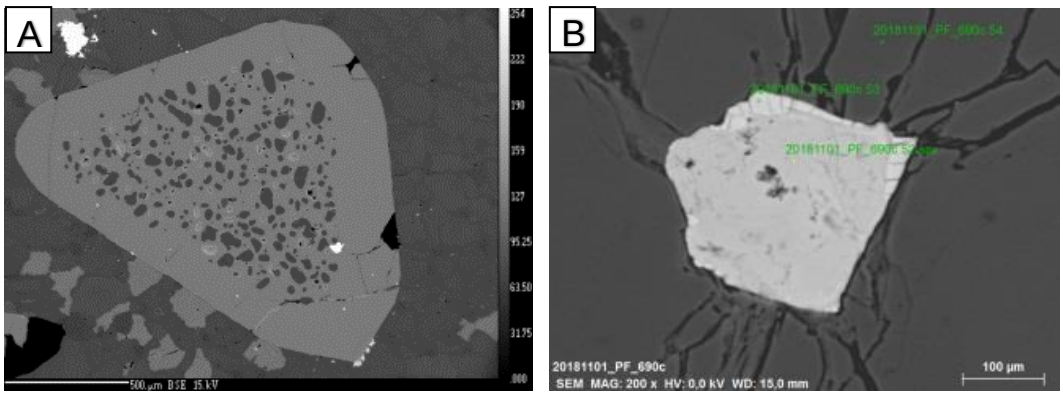

Fig 47. Tourmaline inclusions in sample 690c. A) Inclusion rich tourmaline crystal; B) Zircon inclusion inside fracture.

20160

This hand specimen sample is very coarse grained with tourmalines with dimensions up to 2cm forming along with sugary a vein-type structure up to 4 cm wide. The vein is surrounded by larger (>5 cm) aggregates of mica and quartz. The thin section contains part of two apparent large, subhedral tourmaline crystals. The tourmalines colour in thin section is dark blue and lighter towards the edges. There are also smaller subhedral tourmalines present at the contact of quartz and K-feldspar crystal as seen in Fig 48.

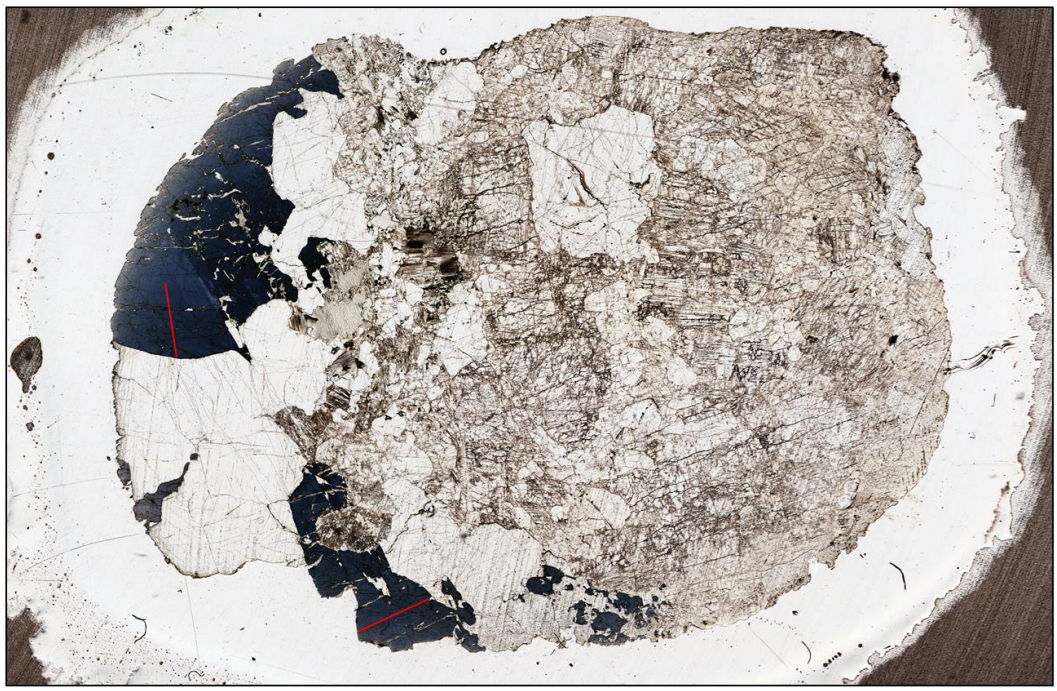

Fig 48. Tourmaline sample 20160 thin section scan. Red lines indicate the profiles targeted for EMPA.

The plenteous inclusions of approximately ~30 µm (as exemplified in Fig 49-A) include mostly on quartz, muscovite, pyrite and xenotime-(Y). Muscovite fragments and inclusions are abundant throughout the tourmalines as shown in Fig 49-B. and pyrite is significantly more abundant in this sample being commonly found inside muscovite inclusions. Contrary to the other samples, there is only one REE (xenotime-(Y)) found in tourmaline and fluorite is less abundant compared to the other samples.

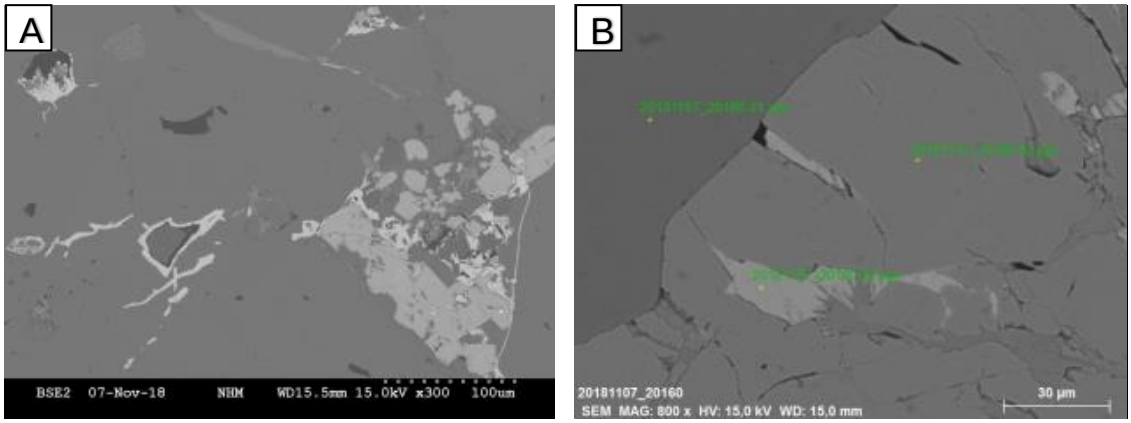

Fig 49. Tourmaline inclusions in sample 20160. A) Quartz, muscovite and pyrite irregular inclusions; B) Muscovite inclusions.

18081715

The hand specimen comprises wedge-shaped (up to 1 cm long) and tiny (<3 mm) tourmalines crystal aggregates in sugary albite with muscovite and fluorite occurrences. The tourmalines form corridors along the albite veins, which are surrounded by quartz, muscovite and k-feldspar. In the thin section, the sample consists in wedge-shaped, euhedral to subhedral, tourmaline crystals of various sizes and orientations. The tourmalines, dark blue in thin section, are located within replacement zone albite next to quartz crystals.

Fig 50. Tourmaline sample 18081715 thin section scan. Red lines indicate the profiles targeted for EMPA

The tourmaline crystals contain large inclusions (with dimensions surpassing 500 μm) as seen in Fig 51-B. This inclusions consist of zircon, muscovite, albite and REE such as kainosite (see table 10). In this sample quartz seems to be intergrown at the edges of the tourmaline crystals. Fluorite and albite are the most common inclusions found in irregular shapes, but there are large cube-shaped REE occurrences both inside (fig. 51-B) and outside the tourmaline crystals.

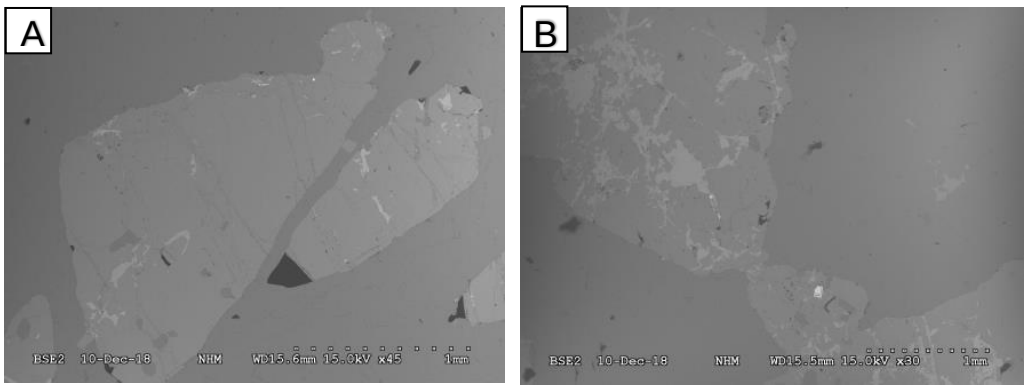

Fig 51. Tourmaline inclusions in sample 18081715. A) Small wedge shape tourmalines with fluorite inclusions; B) Tourmaline with abundant fluorite inclusions and REE.

Table 11. Average EMPA results for the Spro pegmatite tourmalines.

Sample	**690c**	**690b**	**690a**	**20160**	**18081715**
n	**17**	**16**	**16**	**16**	**16**
SiO_2 (Wt %)	34.6(5)	34.5(5)	34.9(4)	34.7(2)	34.4(5)
Al_2O_3	31.7(8)	32(1)	32.0(5)	32.9(1)	32.4(4)
TiO_2	0.3(2)	0.13(3)	0.07(2)	0.04(1)	0.14(4)
FeO	16.7(5)	15.4(7)	16.7(4)	16.0(2)	15.8(7)
Fe_20_3	-	-	-	-	-
MgO	0.3(3)	0.16(4)	0.08(3)	0.11(7)	-
MnO	0.36(4)	0.3(1)	0.25(5)	0.19(2)	0.3(1)
Na_2O	2.4(1)	2.2(1)	2.42(9)	2.34(5)	2.3(1)
B_2O_3	3.00	3.00	3.00	3.00	3.00
CaO	0.19(8)	0.11(4)	0.11(5)	0.12(3)	0.12(5)
Li_2O	-	-	-	-	-
H_2O	-	-	-	-	-
K_2O	0.07(2)	0.07(2)	0.08(2)	0.072(9)	0.07(1)
F	0.7(2)	0.9(2)	1.0(1)	0.8(1)	1.0(2)
Total	87.32	96.66	87.61	87.27	86.53
^{T}Si (apfu)	5.90	5.91	5.94	5.89	5.90
^{T}Al	0.10	0.09	0.06	0.11	0.10
T-site					
^{B}B	3.00	3.00	3.00	3.00	3.00
B-site					
^{Z}Al	6.00	6.00	6.00	6.00	6.00
Z-site					
^{Y}Al	0.27	0.41	0.34	0.48	0.43
^{Y}Mg	0.09	0.04	0.02	0.03	0.02
^{Y}Ti	0.04	0.01	0.01	0.01	0.01
$^{Y}Fe^{2+}$	2.38	2.21	2.37	2.28	2.27
$^{Y}Fe^{3+}$	-	-	-	-	-
^{Y}Mn	0.05	0.05	0.03	0.02	0.05
^{Y}Li	0.13	0.19	0.17	0.09	0.16
Y-site					
^{X}Ca	0.03	0.02	0.02	0.02	0.02
^{X}Na	0.79	0.76	0.79	0.77	0.78
^{X}K	0.01	0.01	0.01	0.01	0.01
X-site					
^{W}F	0.40	0.53	0.53	0.47	0.54
^{W}OH	3.59	3.46	3.46	3.52	3.45
W-site					

Data in parenthesis indicates double standard deviation; - = under detection limit.

Chemistry of tourmalines

Representative analyses of tourmalines from the Spro pegmatite are provided in Table 11. The complete list of tourmaline analyses is given in Appendix 8.7. Structural formulae and site allocation of tourmaline were calculated using an unpublished spreadsheet by Ben Williamson from the Camborne School of Mines, University of Exeter, UK calculating B_2O_3, H_2O and Li_2O by stoichiometry for B = 3 apfu, OH + F = 4 apfu and Li = 15-total (T + Z + Y) and normalizing to 31 anions. Nomenclature follows the guidelines of Henry *et al.*, (2011). All investigated tourmalines are Fe rich (16.178 wt% FeO) with 2.366 wt% NaO and classified as schorl with Fe/(Fe+Mn) ratios of 0.981627 in average and Ca/(Ca-Na) ratios of 0.969458 in average as shown in Fig 53.

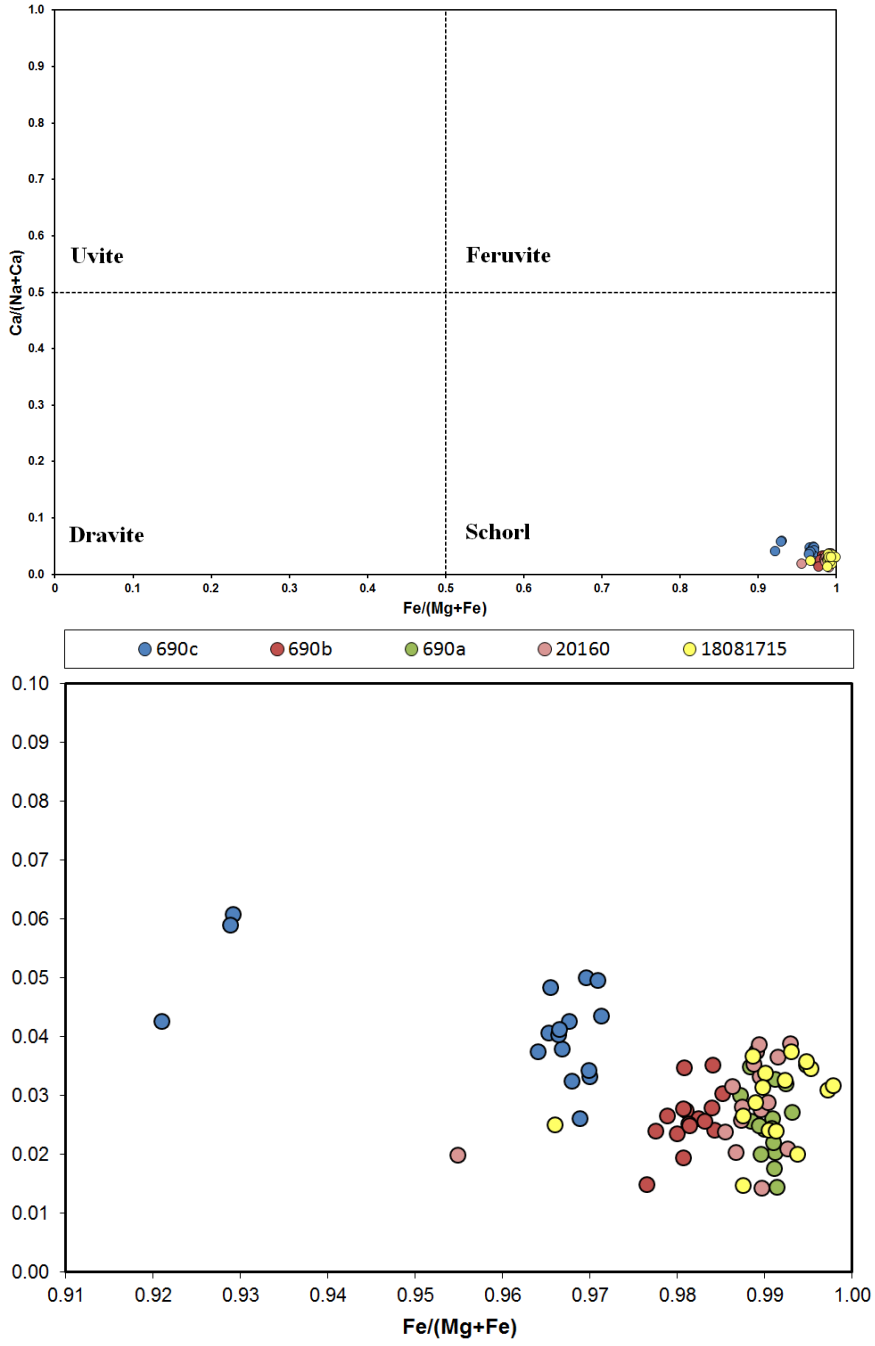

Figs 52 and 53. Tourmaline classification plot adapted from Taghipour and Mackizadeh (2014) and respective 'highlight' on Spro samples' values.

The data of samples 690a, 690b, 690c, 20160 and 18081715 generally cluster in the schorl field. However they have minor differences in element content highlighted by sample 690c which has distinctively higher Mg and Ti than the other samples as seen in plot F) (Fig 54). The Fe and Na contents have little variation throughout the samples but 690b has the lowest average while 690a and 690c have slightly higher Na and Fe content. Sample 690c displays a higher discrepancy from the other samples in Mg content with 0.10 apfu while all other samples cluster between 0.02 and 0.04 apfu. The Ca and Ti contents show similar trends with most samples aggregating while sample 690c once again exhibits the highest values. The other samples have about 0.02 apfu Ca whereas sample 690c 0.04 apfu Ca. Samples 690a and 20160 have lowest average Ti content between 0.005 and 0.01apfu and sample 690c has the distinctively higher values at 0.0411 apfu. The F content is similar for all the samples in general but sample 690c displays slightly lower content. These trends are recognizable in the plots present in Fig 54. The average chemical compositions of the Spro pegmatite tourmaline samples was acquired by EMPA and is shown in table 11. The full EMPA data in can be found in Appendix 8.7.

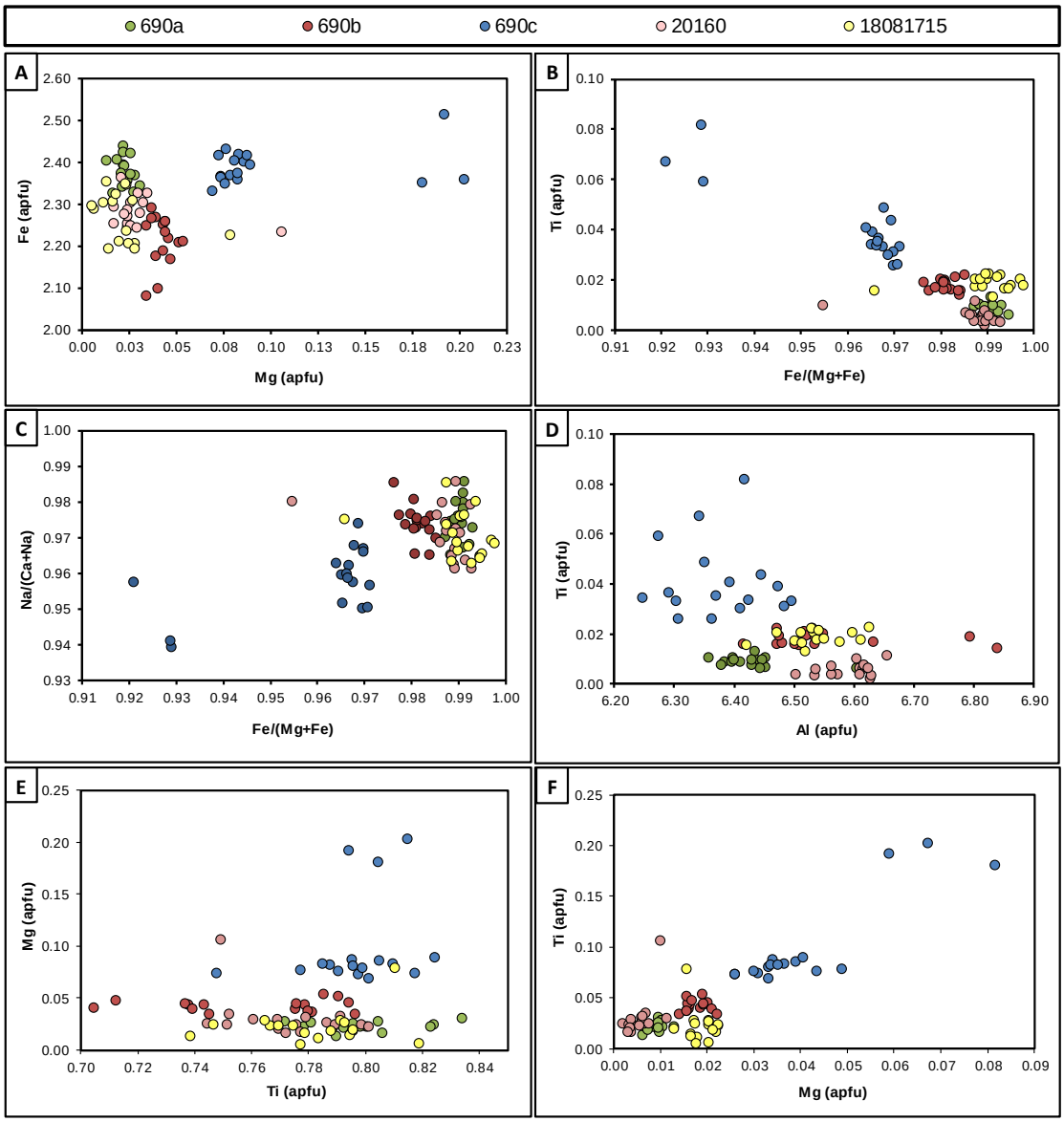

Fig 54. Tourmaline chemical composition (apfu) characterization plots. A) Fe vs Mg exhibiting sample 690c high Mg content; B) Ti vs Fe/(Mg+Fe) displaying sample 690 c high Ti and Mg contents; C) Na/(Ca+Na) vs Fe/(Mg+Fe); D) Ti vs Al; E) Mg vs Ti; and F) Ti vs Mg.

EPMA element profiles were performed on three crystals of samples 18081715, 690c and 690b in order to reveal the crystal-internal variation of the measured elements (Fig 55). The element profiles analysed for Ti, Fe, Mg, Mn and Li indicate significant differences in the distribution and concentration for the studied samples.

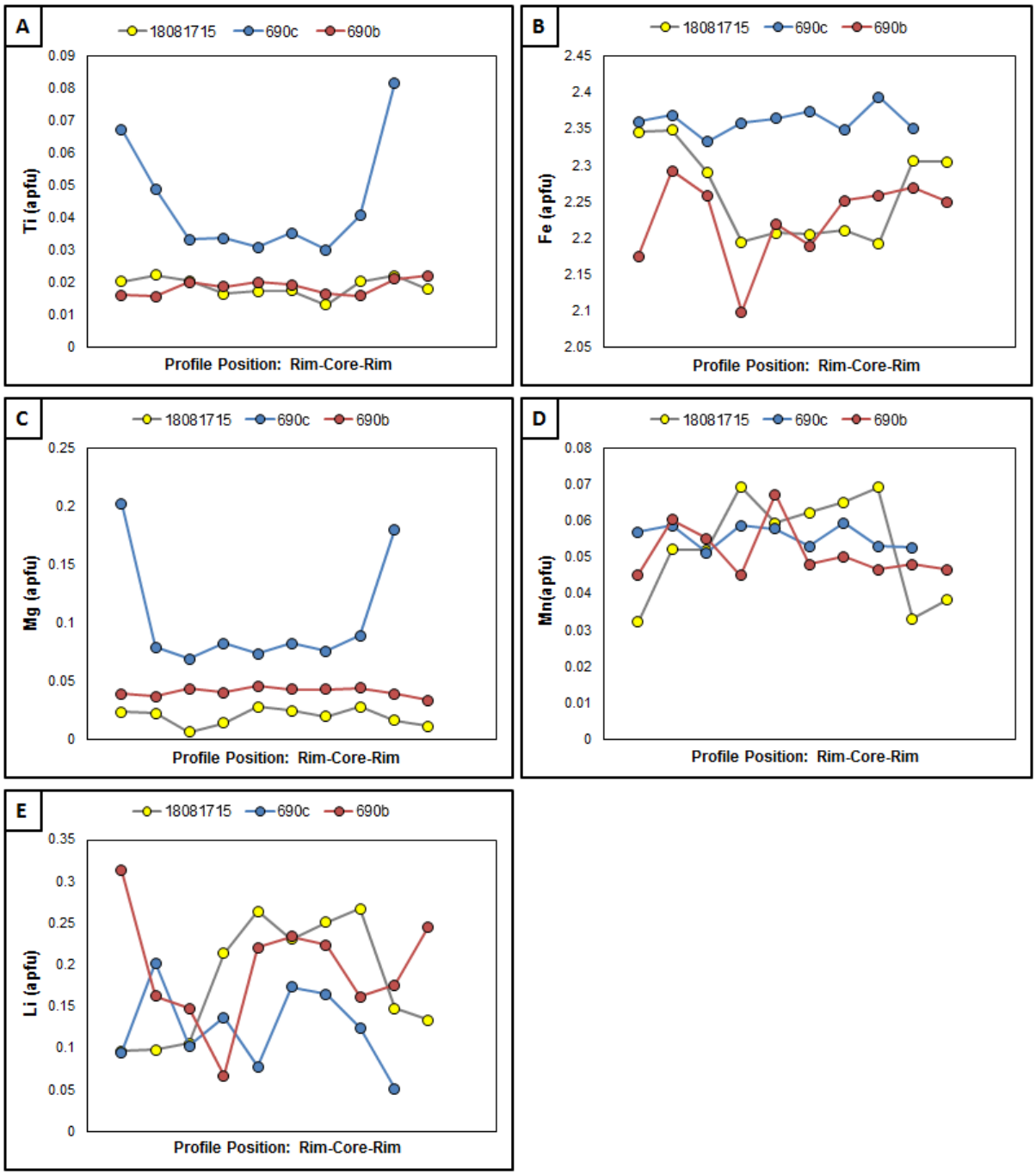

Fig 55. Concentrations (apfu) of Ti, Fe, Mg, Mn and Li (plots A, B, C, D and E respectively) from EMPA across selected tourmaline grains in samples 18081715, 690c and 690b. The vertical axis indicates the element concentration (apfu) and the horizontal axis the position of the analysed points across the grain in a straight line for samples 18081715, 690c and 690 b respectively. The samples 18081715, 690b have 10 analysed points across the grains and sample 690c has 9 analysed points.

Tourmaline of sample 690c displays higher Ti, Mg and Fe values while also displaying zoning in Ti and Mg as both have higher concentration at the rims. In sample 690c the Ti values at the rims reach 0.07 apfu and 0.08 apfu, while in the inclusion-rich core, the values are fairly stable and below 0.04 apfu. In samples 18081715 and 690b the Ti values are constant below 0.025 across the crystals. The Mg values display a similar trend as in sample 690c reaching 0.20 apfu and 0.18 apfu at the rims and remaining constant below 0.100 apfu in the core. For samples 18081715 and 690b, the Mg values in sample 690b are slightly higher than in 18081715but in both samples remain constant throughout the grains (<0.05 apfu). Regarding Fe, sample 690c differs from samples 18081715 and 690b as it displays higher and more conistent values (2.30 to 2.40 apfu) while the other samples have lower and more variant values. Sample 18081715 exhibits some Fe zonation as its concentration is higher at the rims and lower in the core.

The Mn profiles indicate more similar values for all three samples. However, similar to Fe sample 690c exhibits more constant values while 18081715 and 690b display more variation of Fe. Sample 18081715 show Mn zonation with lower concentration at the rims and higher concentrations in the core. The Li profiles display the most random distribution for all three samples but it is still possible to observe that sample 690c does not vary as much as samples 18081715 and 690b. Sample 18081715 exhibits a slight Li enrichment at the crystal margin. The random distribution is understandable as Li is a very small, monovalent ion which forms weak bonds and is more prone to post-crystallization diffusion within the crystal lattice.

The analytical results clearly indicate that the tourmalines of sample 690c form a different tourmaline generation. Considering the textural relationship this generation is younger than the other investigated tourmalines. This matter is further discussed and analysed in Section 5.4.2.

Tourmaline B-isotopic analysis

The occurrence of tourmalines in the Spro pegmatite, which is unusual in most Sveconorwegian pegmatites, brings the possibility to study the melt nature, evolution and emplacement conditions. This study dives into the B-isotope chemical compositions and variations within the tourmaline samples 690a, 690b and 690c to unveil the melt's source and characteristics. The data from tourmaline B-isotopic studies is shown in table 12 and 13, while Fig 56 displays the studied samples and the position of the points taken for analysis. The full data for the tourmaline B-isotopic studies through secondary ion mass spectrometry conducted at the GFZ German Research Centre for Geosciences in Potsdam, Germany is presented in Appendix 8.16.

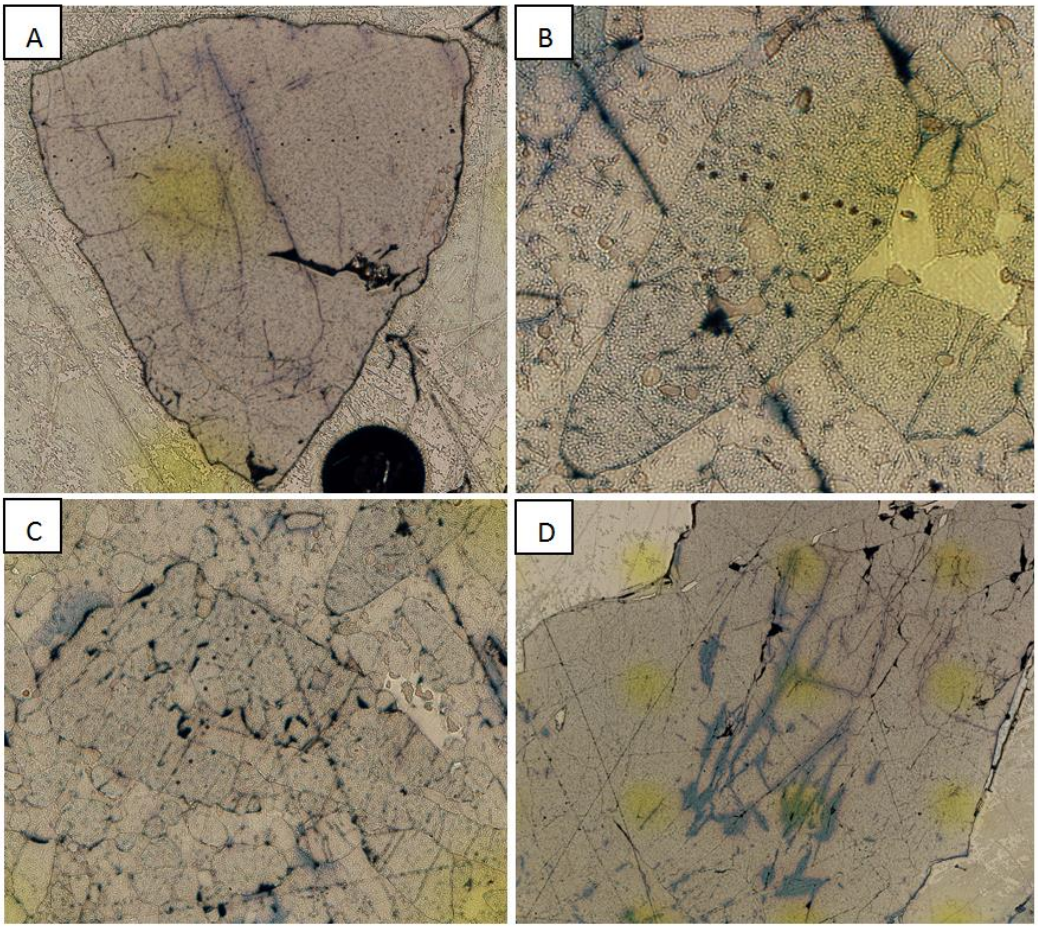

Fig 56. Tourmaline samples analysed through SIMS. A) 690b; B) 690c-1; C) 690c-2; and D) 690a.

The analysed samples exhibit very minor isotopic variation within each grain and do not display isotopic zoning. Overall the tourmalines can be distinguished in two groups. Samples 690a and 690b have average $\delta^{11}B$ values of -12.6 (± 0.4) and -12.5 (± 0.4) respectively, while sample 690c grains 1 and 2 have $\delta^{11}B$ values of -13.8 (± 0.2) and -13.5 (± 0.2). Samples 690a and 690b have less isotopic variation. The 690c sample tourmalines which are smaller, texturally and more chemically distinct, are also slightly isotopically lighter than samples 690a and 690b.

Figure 57 illustrates the B-isotope compositions for the Spro tourmaline in comparison with global boron reservoirs, marine and continental rocks.

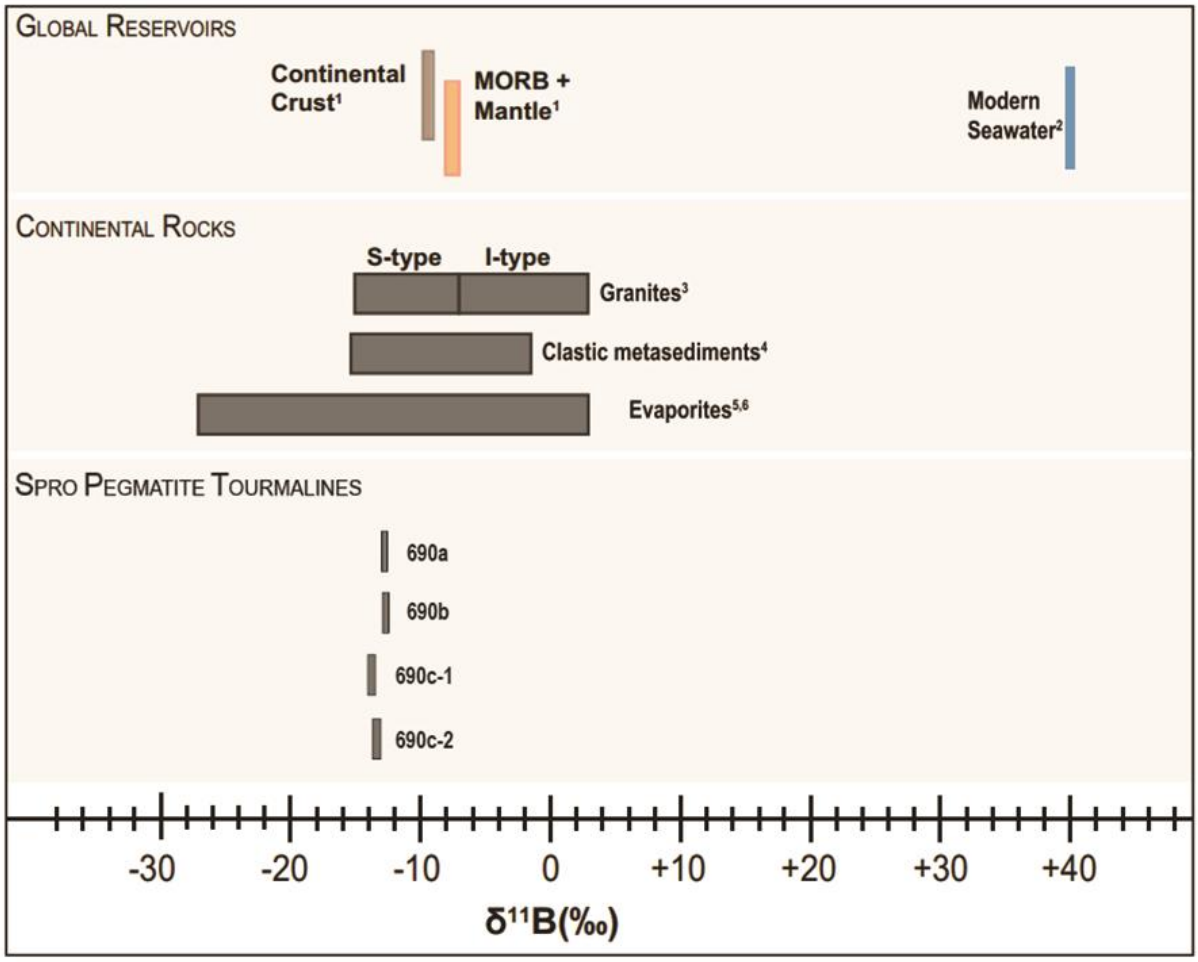

Fig 57. Spro pegmatite tourmalines' B-isotope compositions in comparison with marine rocks, continental rocks and global boron reservoirs (from bottom to top) adapted from Trumbull *et al.,* (2018). Data sources: 1: Marschall (2018), 2: Palmer and Slack (1989), 3: Trumbull and Slack (2018), 4: Trumbull *et al.,* (2011), 5, 6: Palmer and Slack (1989), Kasemann *et al.* (2004).

All the analysed tourmalines exhibit B isotopic compositions between -11 and -13 $\delta^{11}B$. This range falls within th S-type granite range, which also is indicative of peraluminous rocks and reworked crustal rocks.

Table 12. Summary of SIMS analysis from standard sample tourmalines adapted from Trumbull *et al.*, (2013). All the samples were measured on 18/02/2019.

Standard Sample	**$^{11}B/^{10}B$**	**1 s.d. (‰)**	**IMF**	**$\delta^{11}B$(‰)**
Schorl ($^{11}B/^{10}B$ = 3.9931 and $\delta^{11}B$ = -12.5)				
Sch@1	3.912	0.012	0.980	-11.8
Sch@2	3.911	0.010	0.979	-11.9
Sch@3	3.910	0.011	0.979	-12.1
Sch@4	3.911	0.013	0.979	-12.0
Sch@5	3.911	0.010	0.980	-11.8
Sch@6	3.911	0.012	0.979	-11.9
Sch@7	3.912	0.013	0.980	-11.8
Sch@8	3.911	0.010	0.979	-12.0
Sch@9	3.911	0.010	0.980	-11.8
Sch@10	3.912	0.010	0.980	-11.6
Sch@11	3.910	0.011	0.979	-12.1
Sch@12	3.911	0.010	0.979	-11.9
Sch@13	3.911	0.010	0.979	-12.0
Sch@14	3.911	0.009	0.979	-11.9
Sch@15	3.910	0.007	0.979	-12.1
Mean	3.911		0.980	-11.9
Repeatability in per mil	0.14			
Dravite ($^{11}B/^{10}B$ = 4.0169 and $\delta^{11}B$ = -6.6)				
dra@1	3.929	0.011	0.978	-7.3
dra@2	3.929	0.020	0.978	-7.4
dra@3	3.928	0.010	0.978	-7.6
dra@4	3.928	0.011	0.978	-7.7
dra@5	3.928	0.012	0.978	-7.6
dra@6	3.928	0.014	0.978	-7.5
dra@7	3.929	0.016	0.978	-7.4
dra@8	3.930	0.012	0.978	-7.1
dra@9	3.929	0.012	0.978	-7.4
dra@10	3.928	0.013	0.978	-7.6
Mean	3.929		0.978	-7.5
Repeatability in per mil	0.18			

Table 13. Average SIMS analysis values for the Spro pegmatite tourmalines adapted from Trumbull *et al*., (2008).

Samples	**$^{11}B/^{10}B$**	**$\delta^{11}B$ (corrected)**	**n**	**1σ(‰)**
690a	3.993	-12.6	15	0.13
690b	3.993	-12.5	8	0.12
690c (grain 1)	3.988	-13.8	8	0.13
690c (grain 2)	3.989	-13.5	10	0.13

5. Discussion

The study area is located on the west coast of the Nesodden peninsula, an area with a complex tectonic history, which was subjected to high-grade metamorphism during the Sveconorwegian orogeny (1050 Ma according to Pózer Bue, 2008). The Spro pegmatite, the object of this study, is emplaced within a major shear zone, which transects the Proterozoic Spro granite (exhibiting various deformation degrees) and amphibole gneisses. The Spro pegmatite belongs to the petrogenetic NYF pegmatite family. In contrast to other pegmatites of this family, this study revealed it does not display internal mineralogical zoning. Besides this structural observation several factors contributed to the motivation behind this study: The unusual accessory mineral assemblage that is particularly rich in tourmaline, topaz, beryl, fluorite, and samarskite-(Y) which makes the Spro pegmatite unique comparing to other pegmatites from the Sveconorwegian region; the Spro pegmatite emplacement within a shear zone and their relation; and the Spro pegmatite occurrence as an isolated body rather than in a pegmatite field.

To further analyse and understand the genesis of the Spro pegmatite, the following goals where targeted:

5.1 Geological interpretation of the study area in terms of pegmatite formation

The regional geological map (Fig 58) was created following several days of fieldwork as described in Section 3.1. The Spro pegmatite sits on a major shear zone which marks more or less the lithological border between the Spro granite and amphibole gneisses. The variably deformed Spro granite (described in Section 4.4.1), is the dominant rock unit in the studied area. According to Pózer Bue (2008), the Spro granite crystallized between 1542 and 1493 Ma. As previously mentioned, this granite shows different degrees of deformation (foliation) and contains meter-sized shear-lenses of amphibole gneisses in particular towards the shear zone where the Spro pegmatite sits. The protolith age of the amphibole gneisses is estimated between 1600 and 1900 Ma (Versteeve, 1975; Skiold, 1976; Jacobsen and Heier, 1978; Pedersen *et al.*, 1978). The amphibole gneisses, which are chemically and, thus, genetically related to the Spro granite, were deformed under amphibolite facies conditions together with the Spro granite during the Sveconorwegian orogeny (1050 Ma) (Magnusson, 1960; Graversen, 1984; Swensson, 1990; Pózer Bue, 2008). More or less simultaneously, a major shear zone developed in the Spro area. It resulted in local intense deformation and foliation up to mylonitization of the host rocks and the emplacement of the Spro pegmatite melt at 1035 ± 2.2 Ma along the fault (Rosing-Schow, 2019).

The lack of internal zoning of the Spro pegmatite is probably due to ongoing shearing during emplacement and crystallization of the pegmatite melt, disturbing the formation of distinct mineralogical zones. Despite the fact that shearing might have affected its internal zoning, the pegmatite does not exhibit major signs of deformation.

According to Brown and Solar (1998), deforming orogenic belts are non-equilibrium systems that generate feedback relations expressed as interactions between deformation, metamorphism and melting in order to self-organize. Melt formation and migration is a possible consequence of these feedback relations in order to accommodate strain (Brown, 1995).

It is suggested by Brown and Solar (1998) that in the case of crust derived granitic melts, the feedback relation is most effective during the late prograde and peak temperature stage of the P-T evolution in thickened orogenic belts.

Brown and Solar (1998) stated that crystallization of granitic (pegmatitic) melts can take place synchronously with deformation suggesting two alternative scenarios that are not mutually exclusive but represent different perspectives on the shear zone feedback relations.

On one hand, the anatexis of crustal rocks during orogenic deformation may generate granitic melts. These melts make the zones above it rheologically weaker than the surrounding crustal rocks, inducing strain localization and inducing the development of the shear zones (Brown and Solar, 1998). On the other hand, the developed shear zones may induce melt migration and ascent which may result in the emplacement of granitic or pegmatite bodies (Brown and Solar, 1998).

It is suggested that the granitic pegmatite melt was generated within the shear zone during this stage. It is most likely that water was present within the shear zone as shear zone are preferred zones in the crust where hydrothermal fluids move along. That might have facilitated the partial melting of the host rocks (water decreased the melting temperature) in the high-stress zones of the fault which created the melt of the Spro pegmatite (see also discussion below). During the crystallization and transition to the retrograde stage water escape from the pegmatite formed retrograde muscovite along foliation planes in the amphibole gneiss (muscovite-bearing amphibole gneiss) close to the pegmatite as observed in the field.

The partial melting of the crustal rock (pegmatite) protolith is a crucial event in this sequence. In the water-present, high-stress Spro scenario the melting temperature of crustal rocks such as metapelites, metagreywackes, and granites may begin to partially melt in metamorphic conditions with temperatures over 650 $^{\circ}$C, and the resultant melt is granitic in composition (e.g. Sawyer *et al.,* 2011). According to Grujic and Mancktelow (1998), high-grade shear zones are commonly associated with partial melting and migmatite development, with leucosome material concentrated in the zones themselves and in the area around. Small-scale (up to 10 meters) leucosomes in the amphibolite gneisses are found in various areas of the studied region's shore (see Fig 58). This indicates a general high-temperature environment close to partial melting (anatectic) conditions in the vicinity of the shear zone. As discussed in the following sections, the pegmatite protolith is inferred to have a magmatic nature, more specifically of peraluminous, A-type granitic composition. According to Thompson and Collonny (1995) melting of continental crust can occur generally in three ways: 1) H_2O supply to rocks at temperatures above their H_2O-saturated solidi; 2) by dehydration-melting reactions from decompression; 3) by increasing the heat supply through the Moho or base of thickened crust. In this Spro case, the more adequate process is the first, explained by the presence of H_2O due to the many indications referred to in this study. This theory is also supported by Thompson and Collonny (1995) that defend that H_2O is required to generate melts at the temperatures of crustal orogenes. Sawyer *et al.* (2011) also indicate that the occurrence and the quantity of melt produced depend on the availability of H_2O as free fluid in the pores and grain boundaries of the rock. Sawyer *et al.* (2011) also state that regions where water-fluxed partial melting of crustal rocks has occurred can be adjacent to major crustal-scale shear zones, as these can provide the pathways for the H_2O circulation. Additionally, Swensson (1990) indicated that throughout the Nesodden peninsula there is evidence of repeated hydrothermal fluid influxes along planes of weakness (predominantly

faults). With repeated reactivation during the orogenic cycle, these can act and create pathways for hydrothermal fluids.

The Spro pegmatite formation may then be explained by a sequence of feedback relations in response for a non-equilibrium state during orogenic activity. Deformation and partial melting (anatexis) of the Spro pegmatite protolith generated a granitic melt along a major shear zone during the regional (Nesodden area) late peak-metamorphic stage of the Sveconorwegian orogeny. The development of the shear zone is seen as a pivotal event to the melt formation, creating pathways for hydrothermal fluids circulation which lowered the host rock's melting temperature. Consequently, melt migration out of the source and ascent, preferentially along the low-strain (pressure shadows or pull-apart) zones of the fault, is induced to help the system accommodate strain. Following the ascent and beginning crystallization of the melt favoured the immiscible melt formation expressed as tourmaline-topaz-rich sugary albite zones (see discussion below). Albite zones are a common feature of chemically evolved NYF pegmatites that draws much attention for the diverse and evolve mineralogy, often hosting REE and gemstones (Müller *et al.*, 2018). Water escape from the crystallizing pegmatite, retrograde metamorphism and probably also extrinsic hydrothermal fluid are responsible for retrograde mica formation along foliation planes in the neighbouring host rocks.

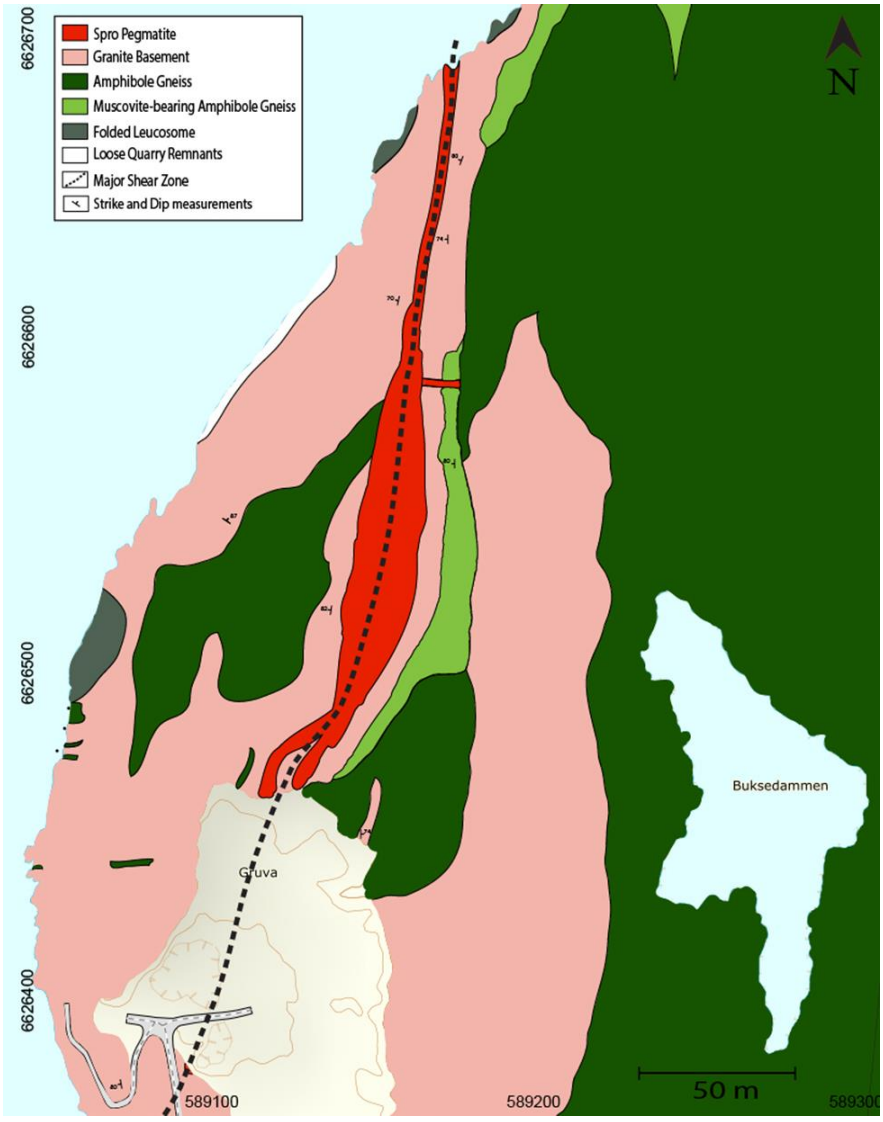

Fig 58. Regional map of the Spro area, main rock units and features.

5.2 Whole rock geochemical data:

The geochemical bulk rock data based on SiO_2 wt% (> 60%) and TiO_2 wt% (<0.7%) as well as Zr/Ti ratio below 0.1 and Ni content below 30 ppm (Fig 20 and 21), indicate that all the studied rock units are all igneous in origin. This knowledge is concordant with previous characterizations of the Spro area geology dominated by Precambrian granitic and gneissic units (e.g. Bugge, 1955; Swensson, 1990; Pózer Bue, 2008). The (A/NK) vs (A/CNK) plot with both ratios above 1.25 for all samples as seen in Fig 23, determined a peraluminous character for all the rock units exposed in the study area. The 10000*Ga/Al and K_2O+Na_2O/CaO ratios indicate that the granites and pegmatite body have a transitional A- to I-type granite affinity. The amphibole gneisses represent highly metamorphosed igneous rocks and have M-, I- and S-type granite affinity according to Whalen *et al.* (1987). This indicates that the rocks were theoretically emplaced in an anorogenetic environment characterized by decompression post-orogeny or during rifting. This might be true for the formation of the Spro granite (1542-1493 Ma according to Pózer Bue (2008)), for which the orogenic setting is basically unknown. However, the Spro pegmatite was emplaced much later in syn- to late-kinematic conditions in respect to the Sveconorwegian orogeny (1035 according to Rosing-Schow (2019)) and has inherited the A-type signature from its melt source. The analysed geochemical nature of the pegmatite samples supports the hypothesis that the protolith was a peraluminous granitic rock, which also supported by the other findings of this study (e.g. B-isotope analysis).

The chondrite-normalized REE plot (fig 27) after Anders and Grevesse (1989) indicates that the pegmatite samples are significantly depleted of LREE but display a trend of enrichment in HREE. The opposite is observed in the host rocks, which are enriched in LREE and become more depleted in HREE. According to Rudnick and Gao (2004) large negative Eu anomalies and enrichment in light rare earth elements are associated with the upper crust compared to the lower crust. Both factors are highly associated with partial melting. The Eu anomaly seen in Fig 27 and examined in Section 4.3 also indicates that the undeformed and slightly deformed Spro granite present in the studied area is significantly but not very fractionated. This information supports the idea that the granites have a continental/cratonic anorogenic origin. The very deformed Spro granite (sample 04061802) which has a much stronger negative Eu anomaly (0.111) is the most fractionated analysed rock and probably represents a more fractionated melt batch of the Spro pluton. The bulk pegmatite sample displays a relatively small Eu anomaly of 0.486 in comparison to the more evolved albite zone bulk composition which has a 0.170 negative Eu anomaly.

The incompatible element signature adapted from Rudnick and Gao (2004) and the REE patterns (Figs 26 and 27) suggest that the pegmatite does not have a genetic relationship with the granitic nor the amphibole host rocks. The amphibole gneisses and Spro granite do have very similar signatures from which is possible to infer that they are chemically related, meaning that the Spro granite represents a melting product of the amphibole gneisses. Considering the crystallization age of the Spro granite between 1542 and 1493 Ma (reference), an older second anatectic event might have occurred in the same area at that time.

To further understand the evolution of the Spro pegmatite melt, whole rock chemistries from the primary stage I and the albite stage II were analysed separately. The data from whole rock chemistry and mineral chemical compositions indicate that the primary pegmatite melt was enriched in most major elements. The late and more fractionated melt of the albite stage II had a melt slightly richer in SiO_2, which may translate to significant compositions variations.
Regarding REE, the bulk pegmatite is more enriched than the albite zones in every REE with the exception of Sm. In comparison to the host rocks which have similar patterns, both pegmatite samples display more depletion of HREE. The host rocks are then slightly depleted in LREE and the pegmatite samples enriched in those. Niobium and Ta, which are usually extremely immobile (Linnen, 1998), become more mobile with increasing F in solutions and melts (Zaraisky *et al.*, 2010) and as a result may have been taken up by the F-rich albite zone-forming melt.

In summary, the geochemical data support the previous hypothesis defending that the Spro pegmatite melt derived from a fairly evolved, granitic peraluminous crustal source emplaced in a continental and probably anorogenic setting.

5.3 The mineralogy and its paragenetic-sequential relationships

Previous work on the Spro pegmatite conducted by Raade (1965) and by the Geologisk Museums Venner (1991a-b, 1993 a-b) established the mineral diversity of the Spro pegmatite (Table 3). In this study, the paragenetic relationship of these minerals has been determined for the mineralogical and genetic characterization of the pegmatite body. In addition, it is also used to infer the conditions during melt emplacement and mineral growth. The evolution of the chemistry mineral with progressing crystallization can be utilized to describe changes in the melt composition.

The pegmatite body displays three distinct crystallization stages: 1) the primary and older stage, represented by the coarse-grained to megacrystic major minerals microline, muscovite, quartz and oligoclase-albite as well as accessory monazite-(Ce), thorite, samarskite-(Y), columbite-(Fe), euxenite-(Y) and possibly beryl (Raade, 1965); 2) the younger stage comprised by irregular cross-cutting veins (mm- to 20 cm in width) of fine-grained sugary albite, containing corridors of tourmaline as well as green muscovite, fluorite, topaz, beryl, microlite group minerals, apatite, and calcite; and 3) an alteration stage with alteration of pre-existing minerals, such as topaz to yellow muscovite, beryl to bertrandite, and galena to hydrocerussite. These are described in the following table 14.

Table 14. Spro pegmatite paragenetic sequence for major minerals and most common accessories.

Mineral	Primary stage I	Late stage II (Albite Zone)	Alteration stage III
Quartz			
Grey Muscovite			
Microline			
OligoclaseAlbite			
Samarskite-(Y)			
Euxenite-(Y)			
Sulphides*			
Sugary Albite			
Tourmaline			
Beryl			
Topaz			
Fluorite			
Calcite			
Green muscovite			
Bertrandite			
Hydrocerussite			
Yellow muscovite			

*Sulphides include chalcopyrite and galena

During the primary stage, the major pegmatite minerals quartz, muscovite, oligoclase-albite and microcline crystalized more or less simultaneously. However, the proportion of these minerals changes with progressing crystallization (muscovite and microcline become more abundant towards the pegmatite core) and so does their trace element chemistry. The chemistry of the plagioclase changes from oligoclase ($Ab_{87.1}$) to pure albite composition ($Ab_{98.6}$) towards the core as indicated in table 6, Section 4.4.1. The microline samples display less chemical variation, but contain less K and more Na towards the core, from $Ab_{5.4}$-An_0-$Or_{94.6\ to}$ $Ab_{6.08}$-An_0-$Or_{93.92}$. The Spro pegmatite micas become richer in Fe (from 0.46 to 0.74

apfu) and Na (from 0.07 to 0.12 apfu) towards the core. Mica sample 04061819 displays distinctive chemical composition and is regarded as the only mica sample representing the alteration stage III which is further discussed in the following section. During this primary stage, samarskite-(Y) and euxenite-(Y) crystallized within megacrystic feldspars and followed by sulphides including chalcopyrite and galena.

The late albite stage is comprised by sugary albite veins (up to 20 cm thick) which cross-cut the primary stage minerals throughout the pegmatite body (Fig 10). These late and chemically more evolved veins (also called albite zones) are suspected to have formed when the first stage minerals were more or less solidified. They represent restitic pegmatite melt enriched in incompatible elements that moved through fractures in the semi-solid pegmatite as their irregular, batchy structures imply. The chemistry of this restitic melt favoured the formation of B-, F-, Be-rich accessory minerals such as tourmaline, beryl, topaz, fluorite and calcite in the pegmatite.

Finally, a posterior alteration stage took place with topaz altering to muscovite, beryl recrystallization and alteration to bertrandite, and galena altering to hydrocerussite. The intense serizitisation of the pegmatitic feldspars (seen in petrography) may be also related to this stage.

The Spro pegmatite is inferred to belong in the NYF petrogenetic pegmatite family. This classification is achieved by the pegmatite's distinctive enrichment in Nb. The presence of in Y and F is indicated by samarskite-(Y), euxenite-(Y), topaz and fluorite, respectively. As previously mentioned in this study, NYF pegmatites usually exhibit a chemical affinity to A-type granites (Eby, 1990; Černý and Ercit, 2005; Martin and De Vito, 2005). This classification is further supported in this study as the Spro pegmatite protolith has an A-type granite chemical signature. According to the classification of pegmatite classes by Černý and Ercit (2005) the Spro pegmatite's belongs to the muscovite-rare-element class and MSREL-REE subclass with samarskite-(Y) and euxenite-(Y) as distinct indicator minerals.

To better understand and describe the pegmatite intrusion, it is important to estimate pressure and temperature conditions during emplacement. Åreback and Andersson (2002) indicate that the observed mineral assemblages might have been equilibrated during thermal peak and therefore yield information on the physical conditions of the intrusion. The absence of high pressure minerals (e.g. cordierite, spinel, corundum) in the Spro host rocks, the observed amphibolite facies in the metamorphosed host rocks and the tectonic history of the region (from the literature), suggest an intra-continental orogenic setting with pressures of up to 6 kbar which corresponds to crustal depth of up to 25 km (e.g. Hensen, 1987). The observed leucosomes (partial melting) in the amphibole gneiss indicate a high temperature environment of at least 650 °C. Simons and Webber (2008) conducted experimental studies of volatile-, flux-rich melts and fluid inclusions. The regional tectonic history, estimated metamorphic conditions, observed mineral assemblages and T-P relationships from such studies (e.g. Simmons and Webber, 2008) suggest initial pegmatite emplacement conditions around 2-6 kbar and approximately 650 °C. However, the formation of F-enriched (topaz, fluorite) albite during the later crystallization stage of the pegmatite suggests a much lower temperature of this final crystallization stage of the pegmatite as discussed below.

5.4 Chemistry of major and accessory minerals for the geochemical and mineralogical classification of the Spro pegmatite and to better understand conditions of pegmatite formation

The chemistry of major minerals feldspars and muscovite, as well as the accessory mineral tourmaline was thoroughly studied to better understand the melt's conditions and evolution. An early assumption in this study regards the minerals as younger/latest to crystalize towards the core of the pegmatite body, and is further supported in the following sections.

5.4.1 Major minerals: Feldspars and Micas

The feldspars of Spro pegmatite, analysed in section 4.4.1, are microcline and plagioclase of oligoclase to albite composition (e.g. Fig 28). The feldspar samples display chemical comsistency, not very variable in general. However, the Ab-rich samples display some chemical variability which is caused by the fact that albite is formed in both the primary stage and the more evolved albite stage (see table 14). As previously mentioned, the primary-stage plagioclase samples display chemistry changes from oligoclase at the pegmatite margin to albite composition towards the core (younger/more evolved). This change forms a continued chemical trend of the plagioclase composition which is characterized by increasing Na while Al and Ca decrease towards the core. Plagioclase of the late albite zones is more homogeneous and has pure albite composition.

The K-feldspars collected from the pegmatite margin towards the core (samples 05061811 and 05061813), display decreasing K/Rb ratios from 372 to 96 ppm and the increasing Rb from ~354 to ~1378 ppm content. This supports the earlier made statement that the crystals of the primary stage crystallized from the pegmatite contact inward. This trend is typical for K-feldspars in granitic pegmatites (Černý et al., 1985) and reflects the chemical evolution of the remaining pegmatite melt during crystallization. The observed increase of 'Ab character' in K-feldspar might be interpreted as decreasing crystallization temperature (Icenhower and London 1996) and concurs with earlier analysis.

The Spro pegmatite mica samples, analysed in section 4.4.2, display more distinct variation in major and trace element chemistry than the feldspar samples, and more evident chemical trends. The distinct K/Rb vs Rb descendant trend seen in Figs 40 and y also concurs with the notion that the samples found closest to the pegmatite core are chemically more evolved and, thus, younger. It is then possible to identify that the oldest and more primitive micas have more variable chemical compositions, while the most evolved are richer in Fe, F, Rb and Na. With progressing crystallization a decrease in Fe in the melt is expected. Iron enters Fe-rich minerals as they commonly have higher crystallization temperatures than other pegmatite-forming minerals. The observed opposite Fe trend may be caused by the absence of major Fe-forming minerals and, thus, Fe became enriched in the remaining melt with progressing crystallization of mica.

Most of the collected micas are classified as ferroan muscovite (Fe content > 0.45 apfu) with only one exception, sample 04061819. This sample plots as the only pure muscovite (see fig 35, Section 4.4.2). It presumably belongs to the alteration stage III (table 14), providing insight into the chemistry of that stage. In comparison to the bulk pegmatite stage micas, this sample is poorer in Fe (0.33 apfu), Na, F, Rb and Y while being richer in Al. The low Rb, F, and Na suggest that the muscovite crystallized from a hydrothermal fluid and post-dates albite stage enriched in Na, F and Rb.

According to Müller *et al.* (2018) the initial stages of pegmatite crystallization can be described by the mineralogy and chemistry of minerals from the border and wall zones of the host pegmatites. Thus, the described chemical composition of major minerals and respective variations allow the interpretation of the melt's evolution. It can be inferred that the primary melt (stage I) started as relatively Ca-rich. The early abundance and consumption of Ca is expected as plagioclase is usually among the first to crystalize in granitic rocks. It can be noted that the presence of ferroan muscovite and absence of biotite indicates that the melt was initially Fe-poor. During progressing crystallization Fe became slightly enriched in the melt because there were no major Fe-bearing minerals. At stage II Fe became so enriched (together with B) that Fe-rich tourmaline (schorl) could crystallize.

The mineral-chemical data of micas such as Rb and Mn content below 0.03 and 0.05 apfu respectively indicate that the Spro pegmatite melt was relatively primitive. In the Sveconorwegia,n "landscape", the Spro pegmatite is still considered quite primitive but not as much as the Froland pegmatites for example, and has an intermediate spread as seen in figs 36 and 40 compared to other Sveconorwegian pegmatites. The occurrence of Al-bearing minerals (tourmaline, topaz and beryl) indicates that the albite veins were Al-rich throughout their crystallization. This is further supported by the presence of crystal-bound water in tourmaline, beryl, and topaz. The nature of the albite veins is further discussed below.

5.4.2 Tourmalines

Also found in the albite veins, the abundant accessory mineral tourmaline is known to grow in both late-magmatic and hydrothermal conditions. In addition, tourmalines are rather rare in Sveconorwegian pegmatites and mostly, known from the Kragerø pegmatites, 120 km SW of Spro (e.g. Kolitsch *et al.*, 2011). Therefore, these are crucial for unveiling the origin of B and nature of the hosting albite veins. Dutrow and Henry (2011) indicate that tourmalines have the ability to adjust their compositions in response to changing chemical environments and *T–P* conditions. In addition, according to Trumbull and Slack (2018), tourmaline zoning provides direct evidence of geochemical changes and can be used to infer melt or fluid compositions.

The tourmaline samples analysed in section 4.4.3 exhibit very homogenous chemical compositions, which already constrains the possible sources and gives insight into the melt evolution. All examined tourmalines are classified as Fe-rich schorl tourmalines (16.2 wt% FeO). According to studies conducted by Kolitsch *et al.* (2011, 2013), schorl is the most common type of tourmaline found in Norway, although the mineral is quite rare in Sveconorwegian pegmatites. Despite the lower Fe content of the albite zone bulk composition compared to those of the bulk pegmatite, there was enough Fe in the albite zone melt (together with Mn and B) to crystallize schorl. The chemical composition of sample 690c which is significantly richer in Mg as well as Ti, distinguishes it from the other Spro tourmaline samples. The more Mg-poor tourmalines mostly likely crystallized prior to the Mg-richer tourmaline 690c which is supported by the textural relationships. As seen in Fig 47-A, tourmaline 690c contains abundant inclusions mostly of quartz whereas the other tourmalines are inclusion-poor. The high abundance of mineral inclusion seems to be a common feature of younger albite stage tourmalines. The same chronological assumption is supported by the slight enrichment of other elements such as Mn, Ca, Ti, Na in sample 690c as the restitic melt crystallized and become more enriched in these elements. In addition, sample 690c displays zoning in Ti and Mg, decreasing from rim to core, which is due to decreasing availability of these elements in the remaining melt. However, the question remains open why the slighter younger tourmalines are slightly richer in the compatible elements Mg and Ti than the older albite-stage tourmalines.

As the major B hosting mineral, tourmaline is a great point of interest in B isotope geochemistry applied to studies of magma- and fluid-related processes including hydrothermal ore formation, crustal metamorphism, anatexis and pluton pegmatite formation (Dutrow and Henry, 2011). Also according to Dutrow and Henry (2011), three primary processes can lead to the formation of tourmaline in igneous rocks:
1) fractional crystallization of igneous melts;
2) partial melting of B-bearing protoliths: Partial melting of B-enriched source rocks has been linked to the development of tourmaline-bearing granitic rocks. In the case of Spro pegmatite that would suggest that melt-melt immiscibility may have taken place (no tourmaline in the primary paragenesis, only in the younger albite stage paragenesis).
3) hydrothermal fluids in association with B-bearing melts: In the later stages of magma crystallization, hydrothermal fluids can be generated and enriched in B due to the partitioning of B into the hydrous fluid at the P–T conditions near the granitic solidus. However, there is no tourmaline-bearing hydrothermal stage associated with the Spro pegmatite.

Scenario 2, which is favoured for this study, can be explained in the following way. In metamorphic environments, formation of tourmaline depends on the initial quantities of B present in the host rocks (protolith) and when that B is released. The tourmaline B isotopic ratio is expected to reflect the conditions of the forming anatectic melt. The study of B-isotopic composition of Spro tourmalines was primarily carried out to better understand the origin of the melt, which could not be solved using the bulk chemistries of the host rocks.

Despite the small data coverage which might indicate an incomplete picture of Spro tourmalines B-isotope composition, the data covers all major textural and chemical types Spro tourmalines. The analysed tourmaline population B-isotopic composition is fairly homogeneous, of approximately -13 δ^{11}B on average. The light B-isotopic composition of the Spro tourmalines is indicative of peraluminous silicate melts from reworked crustal sources. The slightly lighter isotopic composition in sample 690c of -13.65 δ^{11}B in comparison to -12.55 δ^{11}B in samples 690a and 690b is probably caused by crystallization fractionation. These small differences in isotopic composition might just indicate that sample 690c formed at equilibrium with the magma at a slighter later stage than the samples 690a and 690b. This theory is supported by earlier assumptions that considered the tourmalines' chemical composition.

In both the anatexis and crystallization processes, tourmaline will be in contact with a hydrous granitic melt at near-solidus temperatures, so the isotopic shift between tourmaline and melt composition in both events should be nearly the same (Trumbull, 2008). Also according to Trumbull *et al.* (2018) the homogeneous and unzoned B-isotopic composition suggests a single B source. Boron isotope fractionation majorly dependent on two factors: 1) the B coordination (trigonal with heavier composition vs tetrahedral with lighter compositions); and 2) temperature. So, in order to assess the B source, thus the albite zone genesis, these factors must be considered. In this study, the stage II is so far characterized as a hydrous, enriched phase and the fractionation between tourmaline and fluid $\Delta^{11}B_{(tour–fluid)}$ was thoroughly examined by Meyer *et al.* (2008). Despite tourmalines preferences for heavier 11B trigonal coordination, the Spro tourmalines light δ^{11}B suggest tetrahedral coordination. Silicate melts are characterized by a light B-isotopic composition of tetrahedral coordination. It is known from studies (e.g. Meyer *et al.* 2008; Trumbull, 2008) that the fractionation between mediums with the same coordination is small (~2‰). Therefore, the light B-isotopic composition of the Spro tourmalines and the assessed fractionation rates at the referred conditions suggest that the fluid/melt that formed the tourmalines is from partial melting of a peraluminous, granitic

crustal source. It can be inferred that as pegmatite crystallization proceeded, incompatible H_2O, B, F and available Na concentrated resulting in a melt phase separation into enriched hydrous melt batches that crystalized irregularly within the crystallizing primordial pegmatite phase. Consequently, this knowledge suggests that the analysed tourmaline hosting albite veins might be a result of melt-melt immiscibility during pegmatite crystallization rather than post-magmatic metasomatism (Trumbull, 2008).

On another hand, petrographic evidence suggests infiltration of a B-rich fluid from pegmatite to the neighbouring host hock. Tourmaline (very small in size <2 mm) is found in host rock near the shear zone. This amphibolite gneiss (sample *05061804*) cannot be the photolith of the pegmatite, as the REE signatures are very different from that of the Spro pegmatite (Fig 27). The occurrence of tourmaline in the amphibole gneiss indicates that some B of the Spro pegmatite separated into the fluid phase which escaped from the pegmatite during its final crystallization stage. This is supported by Dutrow *et al.* (1999) which suggest that B-rich fluids are known to flux into metamorphic rocks and possibly lead to tourmaline formation. Additionally, van Hinsberg *et al.* (2011) defend that tourmaline forming B may be introduced into metamorphic rocks on the retrograde path. In the Spro case, some B of the pegmatite melt migrated into the neighbouring host rock during retrograde metamorphic stage. It would be necessary to examine the B-isotopic compositions of these host-rock tourmalines to confirm their nature and this hypothesis, which could not be done in this study.

5.5 Historical data on the pegmatite mining and discussion of economic aspects of the pegmatite as a resource of industrial minerals

As explained/referred in the beginning of this study, pegmatite bodies are the sources for many industrial minerals, RRE, and precious gemstones. This leads to an impactful role in many industries, thus making the study and understanding of pegmatite formation very relevant. The feldspar exploration that took place in the Spro pegmatite between 1880 and 1920 was only ceased due to underground water issues. This means that further exploration of the mineral (~700 tonnes/year in Spro) could’ve taken place, which shows the economic potential one pegmatite body. Furthermore, as repeatedly mentioned in this study, the Spro pegmatite occurs as an isolated body contrary to most pegmatites, which are found in pegmatite fields. Pegmatites from the same field, usually display similar characteristics and features, thus increasing the amount of mineral to be exploited and further highlighting the economic potential of pegmatites.

6. Summary and Conclusions

1. Regional Geology and Whole Rock Chemistry Outlook

The investigated Spro pegmatite (1035 Ma), is located within a major shear zone transecting the 1542-1493 Ma old Spro granite and amphibole gneisses (protolith ages ~1600-1900 Ma). The individual occurrence of the Spro pegmatite contrary to most known Sveconorwegian pegmatites is associated with the shear zone in which it is emplaced. It is assessed that the shear zone developed concurrently during the local peak metamorphic stage of the Sveconorwegian orogeny (1050 Ma) due to tectonic movements. The amphibolite facies metamorphism also caused the formation of partial melts preserved as leucosomes in the amphibole gneisses, which indicate combined with analysed mineral assemblages (e.g. absence of high-pressure minerals) P-T conditions of around 2-6 kbar and ~650°C. With development of the shear zone, hydrothermal fluid pathways were formed and the presence of water along the shear zone reduced the pegmatite protolith's melting temperature, influenced crystal growth rate in the resulting pegmatite melt (high water content in granitic melt suppresses the nucleation rate and allows the formation of large crystals) and posterior retrograde reactions in neighbouring host rocks. The ascent of the pegmatitic melt is regarded as a process to accommodate strain.

The geochemical whole rock analyses of the Spro pegmatites and its host rocks provide the following major discoveries. All studied samples of the Spro area have magmatic origin including the amphibole gneisses, and have peraluminous, A-type granite signature, and were theoretically emplaced in an anorogenetic environment characterized by decompression post-orogeny or during rifting. The pegmatite protolith is a peraluminous, anarogenic, A-type granitic rock, but very distinct REE patterns and major element signatures indicate that the pegmatite samples are genetically unrelated to the host rocks. The host rock, in turn, have similar REE and major element patterns, and are genetically related suggesting that the more evolved granite is a product of the amphibole gneiss. It is then inferred that the pegmatite melt was generated by shear-zone-induced partial melting of a granitic, peraluminous B-enriched protolith which is not exposed.

2. Mineralogy, Paragenesis and Geochemical Assessments

The Spro pegmatite belongs to the NYF petrogenetic pegmatite family due to its distinctive enrichment in Nb, presence of Y-bearing minerals such as samarskite-(Y) and euxenite-(Y) as well as F-bearing minerals fluorite and topaz; and to the Muscovite-Rare-Element-REE class based on the occurrence of the major mineral muscovite and accessory samarskite-(Y). The pegmatite body displays three distinct crystallization stages:

1) The primary stage consisted by coarse-grained to megacrystic major minerals microline, muscovite, quartz and oligoclase-albite as well as accessory monazite-(Ce), thorite, samarskite-(Y), columbite-(Fe), and euxenite-(Y).

2) The late-stage albite zones comprising sugary albite, tourmaline, green muscovite, fluorite, topaz, beryl, microlite group minerals, apatite, and calcite;

3) The alteration stage with alteration of pre-existing minerals: topaz to yellow muscovite, beryl to bertrandite, and galena to hydrocerussite.

EMPA of major minerals revealed consistent chemical trends from pegmatite contact to core. Plagioclase (oligoclase to albite) displays increasing Na content with differences up to 0.2 apfu and decreasing Ca content (difference up to 0.04 apfu); K-feldspar displays Rb increase of ~1000 ppm; and mica displays enrichment of Fe, F, Na and Rb (~0.3, 0.16, 0.05 apfu and 62 ppm respectively). These trends indicate that the Spro pegmatite crystallized during the primary stage from the pegmatite contact inward, with the most evolved minerals located at the pegmatite core.

The investigated tourmalines, analysed by EPMA, give better insight into the nature and evolution of the albite zone where it occurs. The tourmalines exhibit homogenous Fe-rich (16.2 wt% FeO) schorl compositions. However, inclusion-rich tourmaline sample 690c, which represents the youngest tourmaline generation of the albite stage, has higher Mg and Ti contents than the other samples. There is a correlation between isotopic compositions (~‰1 lighter) to major-element abundances (Mg, Ti, Ca and Fe), as seen in sample 690c which is also texturally distinct with plenteous inclusions. This supports the idea that sample 690c is slightly younger and crystalized in equilibrium with a slightly more enriched, but isotopically lighter melt. The overall consistent and unzoned average B-isotopic compositions of -13 $\delta^{11}B$, along with a fully magmatic system and low fractionation rates from silicate melts indicate a single crustal peraluminous B source. It is assessed that with progressive pegmatite crystallization, incompatible H_2O, B, F and available Na concentrated and finally separated from the main pegmatite melt phase. The enriched and evolved hydrous albite melt batches crystalized irregularly within the crystallizing primordial pegmatite phase. The chemical and mineralogical consistency of albite zone veins, along progressive mineral enrichment of Na during pegmatite crystallization and the tourmalines low B-isotopic compositions, typical of silicate melts exclude the scenario of stage II formation by metasomatism. Therefore the stage II albite zone is a product of melt-melt immiscibility during pegmatite crystallization.

3. Economic Implications

This study evidences the mineral diversity and economic potential of pegmatite intrusions. As single occurrence rather than a field of pegmatites, formed under unusual circumstances of induced anatexis within a major shear zone, the Spro pegmatite hosted enough feldspar which was exploited for several decades. Considering the shape and position of the Spro pegmatite body, some K-feldspar resources can be expected below its exposed part, presumably 20,000 tons. Albite, quartz, muscovite and REE minerals (smaraskite-(Y), euxenite-(Y)) might be used as by-products. However, because of its isolated location (long transport to nearest processing plant) the Spro pegmatite resources are too small to be economically viable.

Considering the development and findings of this study, some aspects remain available for future studies and further investigation of the Spro pegmatite and its surroundings:

- Analysis of host rock samples for a more precise characterization of the region's tectonic history.
- Further petrologic work for a more precise reconstruction of the regional P-T evolution.
- Analyses of B content and B-isotope compositions of the tourmalines present in the host rock whose compositions can provide further insight into the B-source.

References

ACME Labs (2018) Bureau Veritas Mineral Laboratories. <http://acmelab.com/> accessed 17th October 2018.

Anders, E. and Grevesse, N. (1989) Abundances of the elements: Meteoritic and solar. *Geochimica et Cosmochimica Acta* **53,** 197-214. "Mean C1 Chondr." of Table 1

Åhäll, K.I. and Connelly, J.N. (2008) Long-term convergence along SW Fennoscandia: 330 m.y. of Proterozoic crustal growth. *Precambrian Research* **161,** 452-474.

Andersen, T. and Laajoki, K. (2003) Provenance characteristics of Mesoproterozoic metasedimentary rocks from Telemark, South Norway: a Nd-isotope mass-balance model. *Precambrian Research* **126,** 95- 122.

Andersen, T. *et al.,* (2004) Mid-Proterozoic magmatic arc evolution at the southwest margin of the Baltic shield. *Lithos* **73,** 289-318.

AMMRF (2018) Australian Microscopy & Microanalysis Research Facility <http://ammrf.org.au/> accessed 25th October 2018.

Årebäck, H. and Andersson, U. (2002) Granulite-facies contact metamorphism around the Hakefjorden Norite-Anorthosite Complex, SW Sweden. *Norsk Geologisk Tidsskrift* **82,** 29-44.

Bingen, B. *et al.*, (2001) Correlation of supracrustal sequences and origin of terranes in the Sveconorwegian orogen of SW Scandinavia: SIMS data on zircon in clastic metasediments. *Precambrian Research* **108,** 293-318.

Bingen B. *et al.,* (2005) Timing of continental building in the Sveconorwegian orogen, SW Scandinavia. *Norwegian Journal of Geology* **85,** 87-116.

Bingen B. *et al.,* (2006) Molybdenite Re-Os dating constrains gravitational collapse of the Sveconorwegian orogen, SW Scandinavia. *Lithos* **87,** 328-346.

Bingen B. *et al.,* (2008a) A four-phase model for the Sveconorwegian Orogeny, SW Scandinavia. *Norwegian Journal of Geology* **88,** 43-72.

Bingen B. *et al.,* (2008b) Geochronology of high-grade metamorphism in the Sveconorwegian belt, south Norway: U-Pb, Th-Pb and Re-Os data. *Journal of Norwegian Geology* **88,** 13-42.

Bosi, F. (2018) Tourmaline crystal chemistry. *American Mineralogist* **103,** 298-306. doi: 10.2138/am-2018-6289.

Brewer, T.S. *et al.*, (1998) Contrasting magmatic arcs in the Palaeoproterozoic of the south-western Baltic Shield. *Precambrian Research* ***92,*** 297-315.

Brown, M. (1995) Late-Precambrian geodynamic evolution of the Armorican Segment of the Cadomian Belt (France): Distortion of an active continental margin during south-west directed convergence and subduction of a bathymetric high. *Geologic de la France* **3,** 3-22.

Brown, M. and Solar, G. (1998) Shear-zone systems and melts: Feedback relations and self-organization in orogenic belts. *Journal of Structural Geology* **20,** 211-227. doi: 10.1016/S0191-8141(97)00068-0.

Bugge, A. (1955) Befaring av Spro feltspatforekomst, Nesodden, Akershus. *Norges Geologiske Undersøkelse* Report No.BA 6205, 2

CAMECA (2018) Science and Metrology Solutions <https://www.cameca.com/> accessed 8th February 2019.

Černý, P. (1991a) Fertile granites of Precambrian rare-element pegmatite fields: is geochemistry controlled by tectonic setting or source lithologies? *Precambrain Research* **51,** 429-468.

Černý, P. (1991b) Rare-element granitic pegmatites. Part I: Anatomy and internal evolution of pegmatite deposits. Part 2: Regional to global environments and petrogenesis. *Geoscience Canada* **18,** 49–81.

Černý, P. (1991c) Rare-element granitic pegmatites, Part II. Regional to global environments and petrogenesis. *Geoscience Canada* **18,** 68-81.

Černý, P. and Burt, D.M. (1984) Paragenesis, crystallochemical characteristics, and geochemical evolution of micas in granite pegmatites. *Reviews in Mineralogy* **13,** 257–297.
Černý, P. and Ercit, T.S. (2005) The classification of granitic pegmatites revisited. *Canadian Mineralogist* **43,** 2005-2026. doi: 10.2113/gscanmin.43.6.2005

Černý, P. *et al.,* (1985) Extreme fractionation in rare-element granitic pegmatites: Selected examples of data and mechanism. *Canadian Mineralogist* **23,** 381–421.

Černý, P. *et al.*, (2012) Granitic pegmatites as reflection of their sources. "*Elements" pegmatite issue August 2012, vol. 8*: 289-294. doi: 10.2113/gselements.8.4.289

Chappell, B.W. and White, A.J.R. (1992) I- and S-type granites in the Lachlan Fold Belt. *Earth and Environmental Science Transactions of the Royal Society of Edinburgh* **83** (1-2), 1-26. doi:10.1017/S0263593300007720

Chappell, B.W. and White, A.J.R. (2001) Two Contrasting Granite Types. 25 Years Later. *Australian Journal of Earth Sciences* **48,** 489-499. doi: 10.1046/J1440-0952.2001.00882.x

Collins, W. *et al.,* (1982) Nature and origin of A-type granites with particular reference to SE Australia. *Contributions to Mineralogy and Petrology* **80,** 189-200. doi: 10.1007/BF00374895

Corfu, F. and Laajoki, K. (2008) An uncommon episode of mafic magmatism at 1347 Ma in the Mesoproterozoic Telemark supracrustals, Sveconorwegian orogen - Implications for stratigraphy and tectonic evolution. *Precambrian Research **160,*** 299-307.

Deer, W. A. *et al.*, (2001) Rock Forming Minerals. Volume 4A. Framework Silicates: Feldspars, 2nd Edition, Geological Society of London. *Geological Magazine* **139,** 489 - 492. doi: 10.1017/S0016756802216799.

Deer, W.A. *et al.*, (2003) Sheet silicates: Micas. Rock-forming minerals 2nd Edition, *Geological Society of London,* 758 pp.

Dons, J.A. (1960) The stratigraphy of supracrustal rocks, granitization and tectonics in the Precambrian Telemark area, southern Norway. *Norges geologiske undersøkelse* **212h,** 1-30.

Dutrow, B.L. and Henry, D.J. (2011) Tourmaline: a geologic DVD. *Elements* **7,** 301-306. doi: 10.2113/gselements.7.5.301.

Dyar, M.D. *et al.,* (1998) Inclusive chemical characterization of tourmaline: Mössbauer study of Fe valence and site occupancy. *American Mineralogist* **83,** 848–864.

Dyar, M.D. *et al.,* (2001) Reference minerals for microanalysis of light elements. *Geostandards Newsletter* **25,** 441–463.

Eby, N. (1990) The A-type granitoids: A review of their occurrence and chemical characteristics and speculations on their petrogenesis. *Lithos* **26,** 115-134. doi: 10.1016/0024-4937(90)90043-Z

GFZ - Helmholtz Centre Potsdam (2019) German Research Centre for Geosciences <http://sims.gfz-potsdam.de/> accessed February 7th 2019

GIA (2019) Gemological Institute of America – Tourmaline <http:// https://www.gia.edu/> accessed January 9th 2019

Glover, A. *et al.,* (2012) Granitic Pegmatites: Storehouses of Industrial Minerals. *Elements* **8,** 269-273. doi: 10.2113/gselements.8.4.269.

GMV (1991a) Interne Notater 1961-1990. Mineralogisk-Geologisk Museum, Universitet i Oslo. *Geologisk Museums Venner*, p. 86.

GMV (1991b) Interne Notater 1961-1990. Mineralogisk-Geologisk Museum, Universitet i Oslo. *Geologisk Museums Venner*, p. 99.

GMV (1993a) Interne Notater 1990-1993. Mineralogisk-Geologisk Museum, Universitet i Oslo. *Geologisk Museums Venner*, p. 114.

GMV (1993b) Interne Notater 1990-1993. Mineralogisk-Geologisk Museum, Universitet i Oslo. *Geologisk Museums Venner*, p. 163.

Graversen, O. (1984) Geology and structural evolution of the Precambrian rocks of the Oslofjord-Øyeren area, southeast Norway. *Norges geologiske undersøkelse Bulletin* **398,** 1-50.

Grujic, D. and Mancktelow, N. (1998) Melt-bearing shear zones: analogue experiments and comparison with examples from southern Madagascar. *Journal of Structural Geology* **20,** 673-680. doi: 10.1016/S0191-8141(98)00006-6.

Haapala, I. *et al.,* (2007) Cretaceous Gross Spitzkoppe and Klein Spitzkoppe stocks in Namibia: Topaz-bearing A-type granites related to continental rifting and mantle plume. *Lithos* **97,** 174–192.

Hawthorne, F.C. and Henry, D.J. (1999) Classification of the minerals of the tourmaline group. *European Journal of Mineralogy* **11,** 201-215. doi: 10.1127/ejm/11/2/0201.

Henry, D.J. *et al.,* (2011) Nomenclature of the tourmaline-supergroup minerals. *American Mineralogist* **96,** 895–913. doi:10.2138/am.2011.3636.

Hensen, B.J. (1987) P-T grids for silica-undersaturated granulites in the system MAS (n+4) and FMAS (n+3) - tools for derivation of P-T paths of metamorphism. *Journal of Metamorphic Geology* **5,** 255- 271.

Hervig, R.L. *et al.,* (2002) Isotopic and elemental partitioning of boron between hydrous fluid and silicate melt. *American Mineraogist* **87,** 769 –774. doi: 10.2138/am-2002-5-620

Hinsberg, V. *et al.,* (2011) Tourmaline: An ideal indicator of its host environment. *Canadian Mineralogist* **49,** 1-16. doi: 10.3749/canmin.49.1.1.

Icenhower, J.P. and London, D. (1996) Experimental partitioning of Rb, Cs, Sr, and Ba between alkali feldspar and peraluminous melt. *American Mineralogist* **81,** 719-734.

Jacobsen, S. B. and Heier, K. S. (1978) Rb-Sr isotope systematics in metamorphic rocks, Kongsberl; sector, south Norway. *Lithos* **I1,** 257-276.

JEOL USA (2018) <https://www.jeolusa.com/> accessed 18th October 2018.

Johansson, L. *et al.,* (1991) Late Sveconorwegian (Grenville) high-pressure granulite facies metamorphism in southwest Sweden. Journal of *Metamorphic Geology* 9, 283–292. doi: 10.1111/j.1525-1314.1991.tb00523.x

Kasemann, S.A. *et al.,* (2004) Boron isotope composition of geothermal fluids and borate minerals from salt deposits (central Andes/NW Argentina). Journal of South *American Earth Sciences* **16,** 685–697

Kolitsch, U. *et al.,* (2011) New crystal-chemical data for members of the tourmaline group from Norway: occurences of fluor-schorl and luinaite-(OH). BERGVERKSMUSEETS SKRIFTSERIE NR 46: F. S. Nordrum og A. O. Larsen (red): *Kongsberg Mineralsymposium* 2011, pp. 17- 24

Kolitsch, U. *et al.,* (2013) Tourmaline-group minerals from Norway, part II: Occurrences of luinaite-(OH) in Tvedalen, Larvik and Porsgrunn, and fluor-liddicoatite, fluor-elbaite and fluor-schorl at Ågskardet, Nordland. BERGVERKSMUSEETS SKRIFTSERIE NR 50: A. O. Larsen og K. E. Larsen (red): *Kongsberg Mineralsymposium*, pp. 23-41.

Kowalski, P. and Wunder, B. (2018) Boron isotope fractionation among vapor–liquids–solids–melts: experiments and atomistic modeling. doi: 10.1007/978-3-319-64666-4_3.

Laajoki, K. *et al.,* (2002) Lithostratigraphy and U-Pb geochronology of the Telemark supracrustals in the Bandak-Sauland area, Telemark, South Norway. *Norwegian Journal of Geology* **82,** 119-138.

Larsen, A.O. *et al.,* (1999) Turmaliner i Norge. Bergverksmuseets Skriftserie NR 15: F. S. *Nordrum (red): Kongsberg Mineralsymposium*, pp. 21-30

Le Bas, M.J. *et al.,* (1986) A chemical classification of volcanic-rocks based on the total alkali silica diagram. *Journal of Petrology* **27,** pp. 745–750

Lindh, A. *et al.,* (1998) Beskrivning till berggrundskartan över Värmlands Län; Västra Värmlands Berggrund. *Sveriges Geologiska Undersökning Ser. Ba,* **45:2,** 1-405.

Linnen, R. *et al.,* (2012) Granitic Pegmatites as Sources of Strategic Metals. *Elements* **8,** 275-280. doi: 10.2113/gselements.8.4.275.

London, D. (1995) Geochemical features of peraluminous granites, pegmatites, and rhyolites as sources of lithophile metal deposits. *In* Magmas, Fluids, and Ore Deposits. *Mineralogical Association of Canada, Short Course Handbook* **23,** 175-202.

London, D. (2008) Pegmatites. *Canadian Mineralogist Special Publication* **10,** 368 pp.

London, D. (2014) A petrologic assessment of internal zonation in granitic pegmatites. *Lithos,* 184-187. 74-104. doi: 10.1016/j.lithos.2013.10.025.

London, D. and Kontak, D. (2012) Granitic Pegmatites: Scientific Wonders and Economic Bonanzas. *Elements* **8,** 257-261. doi: 10.2113/gselements.8.4.257.

Magnusson N.H. (1960) Age determinations of Swedish Precambrian rocks, *Geol. Fören. Stockholm Förh.* **82,** 407.

Marchal, K.L. *et al.,* (2014) Geochemistry, mineralogy, and evolution of Li-Al micas and feldspars from the Mount Mica Pegmatite, Maine, USA. *Canadian Mineralogist* **52,** 221–233.

Marschall, H.R. and Jiang, S.Y. (2011) Tourmaline isotopes: no element left behind. *Elements* **7,** 313–319. doi: 10.2113/gselements.7.5.313.

Martin, R.F. and De Vito, C. (2005) The patterns of enrichment in felsic pegmatites ultimately depend on tectonic setting. *Canadian Mineralogist* **43,** 2027-2048. doi: 10.2113/gscanmin.43.6.2027

Melka, K. (2009) A scheme for the classification of micaceous minerals. *Acta Geodynamica et Geomaterialia* **6,** 69-75.

Meyer, C. *et al.,* (2008) Boron-isotope fractionation between tourmaline and fluid: An experimental re-investigation. *Contributions to Mineralogy and Petrology* **156,** 259-267. doi: 10.1007/s00410-008-0285-1.

MINDAT (2018) Mindat.org: Spro pegmatite, Nesodden, Akershus, Norway <https://www.minerals.net/> accessed 19th September 2018.

Minerals.net (2018) TheMinerals and Gemstone Kingdom, The Tourmaline ineral Group <https://www.mindat.org/> accessed 19th September 2018.

Möller, C. *et al., (*2007) Linking deformation, migmatite formation and zircon U-Pb geochronology in polymetamorphic gneisses, Sveconorwegian province, Sweden. *Journal of Metamorphic Geology* **25,** 727-750.

Morgan VI, G.B. and London, D. (1987) Alteration of amphibolitic wall rocks around the Tanco rare-element pegmatite, Bernic Lake, Manitoba. *American Mineralogist* **72**, 1097-1121.

Morgan VI, G.B. and London, D. (1989) Experimental reactions of amphibolite with boron-bearing aqueous fluids at 200 MPa: implications for tourmaline stability and partial melting in mafic rocks. *Contributions to Mineralogy and Petrology* **102,** 281-297.

Müller, A. *et al.,* (2006) The Land's End granite, Cornwall: the evolution of a composite and mineralised pluton. *Ore Geology Reviews* **28,** 329-367. doi: 10.1016/j.oregeorev.2005.05.002.

Müller, A. *et al.,* (2015a) The chemistry of quartz in granitic pegmatites of southern Norway: Petrogenetic and economic implications. *Economic Geology* **110,** 1737–1757.

Müller, A. *et al.,* (2015b) The Sveconorwegian pegmatite province: 5000 pegmatites and no parental granite? Book of Abstracts, 7th International Symposium on Granitic Pegmatites, PEG 2015 Ksiąź, Poland (58–59).

Müller, A. *et al.,* (2017) The Sveconorwegian Pegmatite Province – Thousands of pegmatites without parental granites. *Canadian Mineralogist* **55,** 283-315. doi: 10.3749/canmin.1600075.

Müller, A. *et al.,* (2018) 'Alkali-F-rich albite zones in evolved NYF pegmatites - the product of melt-melt immiscibility', *Canadian Mineralogist* **56 (4),** 657–687. doi: https://doi.org/10.3749/canmin.1700087

Munz, I.A. *et al.,* (1994) Retrograde fluid infiltration in the high-grade Modum Complex, S Norway: evidence for age, source and REE mobility. *Contributions to Mineralogy and Petrology* **116,** 32-46.

Neiva, A.M.R. (2013) Micas, feldspars and columbitetantalite minerals from the zoned granitic lepidolitesubtype pegmatite at Namivo, Alto Ligonha, Mozambique. *European Journal of Mineralogy* **25,** 967–985.

NTS (2018) Testing, Inspection & Certification Services < https://www.nts.com/> accessed 26th October 2018.

Palmer, M.R. and Slack, J.F. (1989) Boron isotopic composition of tourmaline from massive sulfide deposits and tourmalinites. *Contributions to Mineralogy and Petrology* **103,** 434–451.

Park, R.G. *et al.,* (1991) The Sveconorwegian shearzone network of SW Sweden in relation to mid-Proterozoic plate movements. *Precambrian Research* **49,** 245-260.

Pearce, J. *et al.,* (1984) Trace Element Discrimination Diagrams for the Tectonic Interpretation of Granitic Rocks. *Journal of Petrology* **25,** 956-983. doi:10.1093/petrology/25.4.956.

Pedersen, S. *et al.,* (1978) Rb/Sr-dating of the plutonic and tectonic evolution of the Sveconorwegian province, southern Norway. Sixth European Colloquium. In Zartman, (ed.): Short papers of the 4th International Conference on Geochronology, *Cosmochronology and Isotope Geology. US Geological Survey Open-file Report* **78-701,** 329--331.
Pózer Bue, E. (2008) Age and Origin of the Mesoproterozoic Basement of the Nesodden Peninsula, SE Norway : A Geochronological and Isotopic Study. MsC. Thesis, University of Oslo, Norway.

Raade, G. (1965) The minerals of the granite pegmatite at Spro, Nesodden, near Oslo. *Norges Geologiske Undersøkelse* 234 [Årbok 1964], 160-166.

Raade, G. (1982) Alvitt fra Spro, Nesodden. in Geologisk Museum. Interne notater 1961-1990. Published by Geologisk Museums Venner, Oslo 1991, p 99.

Rieder, M. *et al.,* (1998) Nomenclature of the micas. *The Canadian Mineralogist* **36,** 905-912.

Rosing-Schow, N. *et al.,* (2018) A Comparison of the Mica Geochemistry of the Pegmatite Fields
inSouthernNorway. *CanadianMineralogist.* ISSN 00084476. 56(4), s 463488 . doi: 10.3749/canmin.1700086

Rosing-Schow, N. (in progress) The Sveconorwegian pegmatite province: Identifying the genetic parameters controlling the abundance and diversity of the rare metal mineralization . Ph.D. Thesis, Natural History Museum of Oslo, University of Oslo, Norway.

Rudnick, R.L. Gao, S. (2004) Composition of the continental crust. In Treatise on Geochemistry; Holland, H.D., Turekian, K.K., Eds.; Elsevier: Amsterdam, The Netherlands, 2004; Volume 3, pp. 1–64.

RUHR-Universität Bochum (2018) <http://www.ruhr-uni-bochum/> accessed 26th Octoer 2018.

Sawyer, E. *et al.,* (2011) When the Continental Crust Melts. *Elements* **7,** 229-234. doi: 10.2113/gselements.7.4.229.

SERC (2018) The Science Resource Center at Carleton College <https://serc.carleton.edu/> accessed 25th October 2018 and February 7th 2019.

Shand, S.J. (1943) Eruptive Rocks. Their Genesis, Composition, Classification, and Their Relation to Ore-Deposits with a Chapter on Meteorite; JohnWiley & Sons: New York, NY, USA, 1943; p. 350.

Slack, J.F. and Trumbull, R.B. (2011) Tourmaline as a recorder of ore-forming processes. *Elements* **7,** 321–326.

Simmons, W. and Webber, K. (2008) Pegmatite genesis: State of the art. *European Journal of Mineralogy* **20,** 421-438. doi: 10.1127/0935-1221/2008/0020-1833.

Simmons, W. *et al.,* (2003) Pegmatology – pegmatite mineralogy, petrology and petrogenesis. Rubellite Press, New Orleans, LA, 176 p.

Simmons, W. *et al.,* (2013) Granitic Pegmatites as Sources of Colored Gemstones. *Elements* **8,** 281-287. doi: 10.2113/gselements.8.4.281.

Skiöld, T. (1976) The interpretation of the Rb-Sr and K-Ar ages of late Precambrian rocks in south-western Sweden. *GFF* **98,** 3-29. doi: 10.1080/11035897609454335.

Soares, D.R. *et al.,* (2008) Compositional variation of tourmaline-group minerals in the Borborema Pegmatite Province, northeastern Brazil. *Canadian Mineralogist* **46,** 1097–1116.

Söderlund, U. *et al.,* (1999) Protolith ages and timing of deformation in the eastern marginal part of the Sveconorwegian orogen, southwestern Sweden. *Precambrian Research* **94,** 29–48.

Swensson, E. (1990) Cataclastic rocks along the Nesodden Fault, Oslo Region, Norway: a reactivated Precambrian shear zone. *Tectonophysics* **178,** 51-65. doi: 10.1016/0040-1951(90)90459-L.

Taghipour, B. and Mackizadeh, M. (2014) The origin of the tourmaline-turquoise association hosted in hydrothermally altered rocks of the Kuh-Zar Cu-Au-turquoise deposit, Damghan, Iran. Neues Jahrbuch für Geologie und Paläontologie - Abhandlungen. 272. doi: 10.1127/0077-7749/2014/0397.

Thompson, A.B. and Connolly, J. (1995) Melting of the continental crust: Some thermal and petrological constraints on anatexis in continental collision zones and other tectonic settings. *Journal of Geophysical Research* **100.** 15565-15580. doi: 10.1029/95JB00191.

Tischendorf, G. *et al.,* (2001) Minor- and trace-element composition of trioctahedral micas: a review. *Mineralogical Magazine* **65,** 249-276. doi: 10.1180/002646101550244.

Tischendorf, G. *et al.,* (2007) True and brittle micas: Composition and solid-solution series. Mineralogical Magazine **71,** 285-320. doi:10.1180/minmag.2007.071.3.285.

Trumbull, R. and Slack, J.F. (2018) Boron Isotopes in the Continental Crust: Granites, Pegmtites, Felsic Volcanic Rocks, and Related Ore Deposits. pp.249-272. doi: 10.1007/978-3-319-64666-4_10.

Trumbull, R.B. *et al.,* (2008) Chemical and boron-isotope variations in tourmalines from an S-type granite and its source rocks: the Erongo granite and tourmalinites in the Damara Belt, Namibia. *Contributions to Mineralogy and Petrology* **155,** 1–18. doi: 10.1007/s00410-007-0227-.

Trumbull, R.B. *et al.,* (2011) Fluid sources and metallogenesis in the Blackbird Co–Cu–Au–Bi– Y–REE district, Idaho, U.S.A.: insights from major-element and boron isotopic compositions of tourmaline. *Canadian Mineralogist* **49,** 225– 244. doi: 10.3749/canmin.49.1.225.

Trumbull, R. *et al.,* (2013) The diversity of B-isotope variations in tourmaline from rare-element pegmatites in the Borborema Province of Brazil. *Chemical Geology* **352,** 47–62. doi: 10.1016/j.chemgeo.2013.05.021.

Trumbull, R.B. *et al.,* (2018) Tourmaline in the Passagem de Mariana gold deposit (Brazil) revisited: major-element, trace-element and B-isotope constraints on metallogenesis. *Mineralium Deposita*. doi: 10.1007/s00126-018-0819-z.

Turtumøygard, S. (2004) Steinhoggerne på Spro. Follo Historielag Årbok 2014 *Follominne,* 13-20.

Versteeve, A. J. (1975) Isotope geochronology in the highgrade metamorphic Precambrian of Southwestern Norway. *Nor. Geo/. Unders.* **318,** 1-50.

Vorren, T. and Mangerud, J. (2008) Glaciations come and go. Pleistocene, 2.6 million-11,500 years ago. In: Ramberg, I., Bryhni, I., Nøttvedt, A., Rangnes, K. (Eds.), The Making of a Land—Geology of Norway.

Winchester, J.A. and Floyd, P.A. (1977) Geochemical discrimination of different magma series and their differential products, using immobile elements. *Chemical Geology* **20,** 325–344.

Winchester, J. A. and Max, M. D. (1984) Geochemistry and origin of the Annagh Division of the Precambrian Erris complex, NW County, Mayo, Ireland. *Precambrian Research* **25,** 397–414.

Wolf, M. and London, D. (1997) Boron in granitic magmas: stability of tourmaline in equilibrium with biotite and cordierite. *Contributions to Mineralogy and Petrology* **130,** 12-30. doi: 10.1007/s004100050346.

8. Appendix

Appendix 8.1 Sample List

Sample	Mineral/Rock	Preparation	Analyses	UTM zone	East	North
157a	Pyrite	-	Photograph	-	-	-
157b	Malachite	-	-	-	-	-
158	Samarskite	-	Photograph	-	-	-
159	Fluorite	-	Photograph	-	-	-
191a	Muscovite	1-inch mount	Photograph	-	-	-
191b	K-feldspar	Thick section	-	-	-	-
614	Topaz	-	Photograph	-	-	-
616	Columbite-(Fe)	1-inch mount	-	-	-	-
690a	Tourmaline	Thin section	EPMA	-	-	-
690b	Tourmaline	Thin section	EPMA	-	-	-
690c	Tourmaline	Thin section	EPMA	-	-	-
690x	Tourmaline	-	Photograph	-	-	-
693	Calcite	-	-	-	-	-
734a	K-feldspar	Thin section	-	-	-	-
734b	K-feldspar		-	-	-	-
-	Muscovite	1-inch mount	-	-	-	-
-	Muscovite	-	-	-	-	-
18081709	Quartz	Thick section	-	32V	589134	6626548
18081710	Muscovite	1-inch mount	-	32 V	589134	6626548
18081711	Samarskite	-	-	32 V	589134	6626548
18081712	Euxenite-(Y)?	-	Photograph	32 V	589134	6626548
18081713	Fluorite	Thick section	-	32 V	589134	6626548
18081714	Tourmaline	-	-	32 V	589134	6626548
18081715	Tourmaline	Thin section	EPMA	32 V	589134	6626548
18081716	Beryl	-	Photograph	32 V	589134	6626548
10451*	Anatase	-	Microphoto	-	-	-
11235*	Bastnäsite	-	Photograph	-	-	-
14140*	Pyrite	-	Photograph	-	-	-
14183*	Hydrocerussite	-	-	-	-	-
14629*	Zircon	-	-	-	-	-
15688*	Monazite	-	Photograph	-	-	-
16209*	Microlite	-	Microphoto	-	-	-
16758*	Samarskite	-	Photograph	-	-	-
17131*	Columbite-(Fe)	-	-	-	-	-
20160*	Tourmaline	Thin section	EPMA, photo	-	-	-
24156*	Bertrandite	-	Microphoto		-	-
26348*	Muscovite	-	-	-	-	-
31471*	Beryl	-	-	-	-	-
35699*	Euxenite-(Y)	-	-	-	-	-
35700*	Euxenite-(Y)	-	-	-	-	-
35701*	Euxenite-(Y)	-	-	-	-	-
35702*	Euxenite-(Y)	-	-	-	-	-
35703*	Euxenite-(Y)	-	Photograph	-	-	-
35886*	Euxenite-(Y)	-	-	-	-	-
36446*	Samarskite	-	-	-	-	-
41072*	Euxenite-(Y)	-	Photograph	-	-	-
04061801	Amphibole Gneiss	Thin section, crushing,	Whole rock: ICP-MS	32 V	0589138	6626670

		milling,				
04061802	Granite	Thin section, crushing, milling,	Whole rock: ICP-MS	32 V	0589148	6626665
04061803	K-Feldspar	Epoxy Cast 9	EMPA	-	-	-
04061804	K-feldspar	Epoxy Cast 9	EMPA	-	-	-
04061805	K-feldspar	Epoxy Cast 9	EMPA	-	-	-
04061806	K-feldspar lightest	Epoxy Cast 9	EMPA	-	-	-
04061807	Plagioclase	Epoxy Cast 9	EMPA	-	-	-
04061808	Plagioclase	Epoxy Cast 10	EMPA	-	-	-
04061809	k-feldspar	Epoxy Cast 10	EMPA	-	-	-
04061810	k-feldspar	Epoxy Cast 10	EMPA	-	-	-
04061811	Plagioclase	Epoxy Cast 10	EMPA	-	-	-
04061812	Cleavelandite	Epoxy Cast 10	EMPA	-	-	-
04061813	Plagioclase	Epoxy Cast 10	EMPA	-	-	-
04061814	Dark Muscovite	Epoxy Cast 13	EMPA	-	-	-
04061815	Dark Muscovite	Epoxy Cast 13	EMPA	-	-	-
04061816	Wavy finer Muscovite	Epoxy Cast 13	EMPA	-	-	-
04061817	Intergrown Albite-coarse Muscovite	Epoxy Cast 12	EMPA	-	-	-
04061818	Coarse Yellow Muscovite	Epoxy Cast 13	EMPA	-	-	-
04061819	Fine yellow Muscovite	Epoxy Cast 12	EMPA	-	-	-
04061820	Muscovite	Epoxy Cast 12	EMPA	-	-	-
04061821	Muscovite	Epoxy Cast 12	EMPA	-	-	-
04061822	Tourmalines	-	-	-	-	-
04061823	Tourmaline	-	-	-	-	-
04061824	Tourmaline	-	-	-	-	-
04061825	Tourmaline	-	-	-	-	-
04061827	Fluorite coating	-	-	-	-	-
04061828	Massive Fluorite	-	-	-	-	-
04061829	Fergusonite	-	-	-	-	-
04061830	Fergusonite	-	-	-	-	-
04061831	Fergusonite	-	-	-	-	-
05061801	Granite	Thin section, crushing, milling,	Whole rock: ICP-MS	32 V	0589113	6626486
05061802	Amphibole Gneiss	Thin section, crushing, milling,	Whole rock: ICP-MS	32 V	0589119	6626473
05061803	Granite	Thin section, crushing, milling,	Whole rock: ICP-MS	32 V	0589106	6626483
05061804	Amphibole Gneiss	Thin section, crushing, milling,	Whole rock: ICP-MS	32 V	0589119	6626473
05061805	Muscovite	Epoxy Cast 19	EMPA	-	-	-
05061806	Muscovite	Epoxy Cast 19	EMPA	-	-	-
05061807	Muscovite	Epoxy Cast 19	EMPA	-	-	-
05061808	Muscovite	Epoxy Cast 19	EMPA	-	-	-
05061809	K-Feldspar	Epoxy Cast 10	EMPA	-	-	-
05061810	Plagioclase	Epoxy Cast 10	EMPA	-	-	-
05061811	K-feldspar	Epoxy Cast 11	EMPA	-	-	-
05061812	Plagioclase	Epoxy Cast 11	EMPA	-	-	-
05061813	K-Feldspar	Epoxy Cast 11	EMPA	-	-	-
05061814	Albite	Epoxy Cast 11	EMPA	-	-	-
16091806	Bulk Pegmatite	crushing, milling,	Whole rock: ICP-MS	-	-	-
690	Albite-Zone	crushing, milling,	Whole rock: ICP-MS	-	-	-

*NHM mineral collection; Thin sections prepared with 300-μm thickness

Appendix 8.2: Epoxy Casts Scans

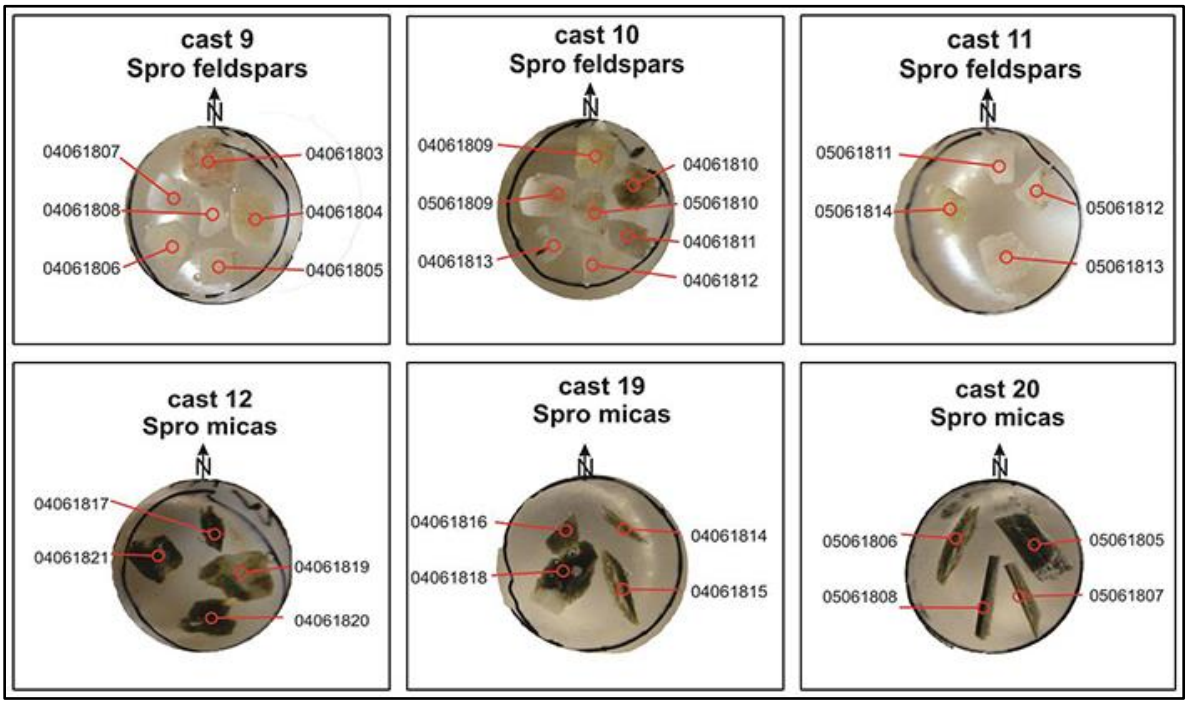

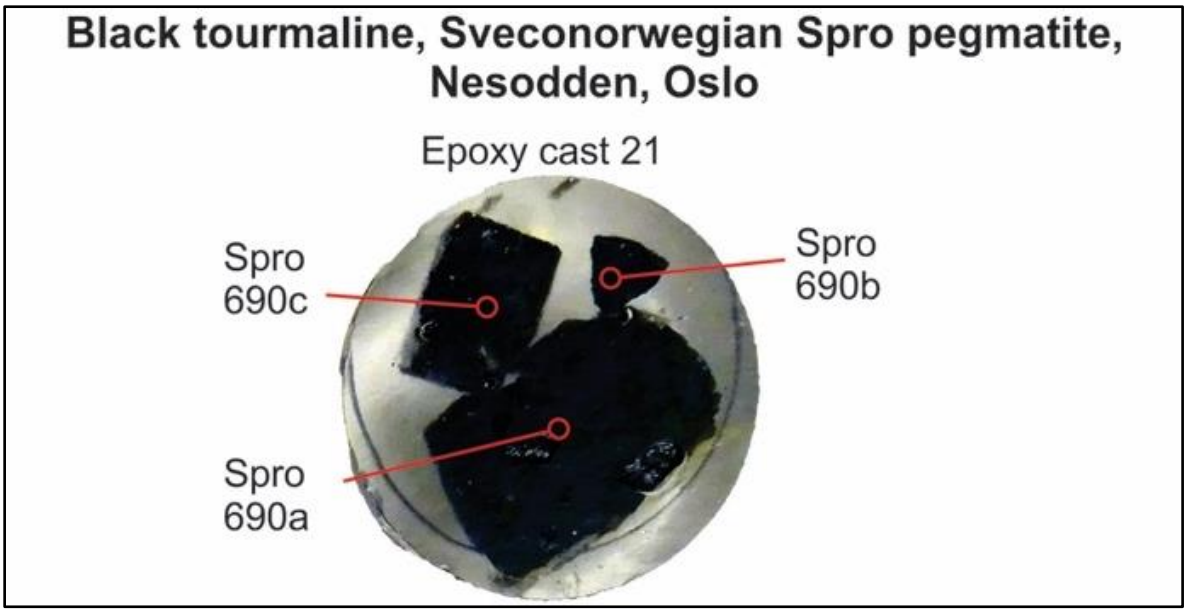

Appendix 7.2- Epoxy casts scans: Casts 9-11) Feldspars; Casts 12, 19 and 20) Micas; Cast 21) Tourmalines.

Appendix 8.3: Thin sections scans

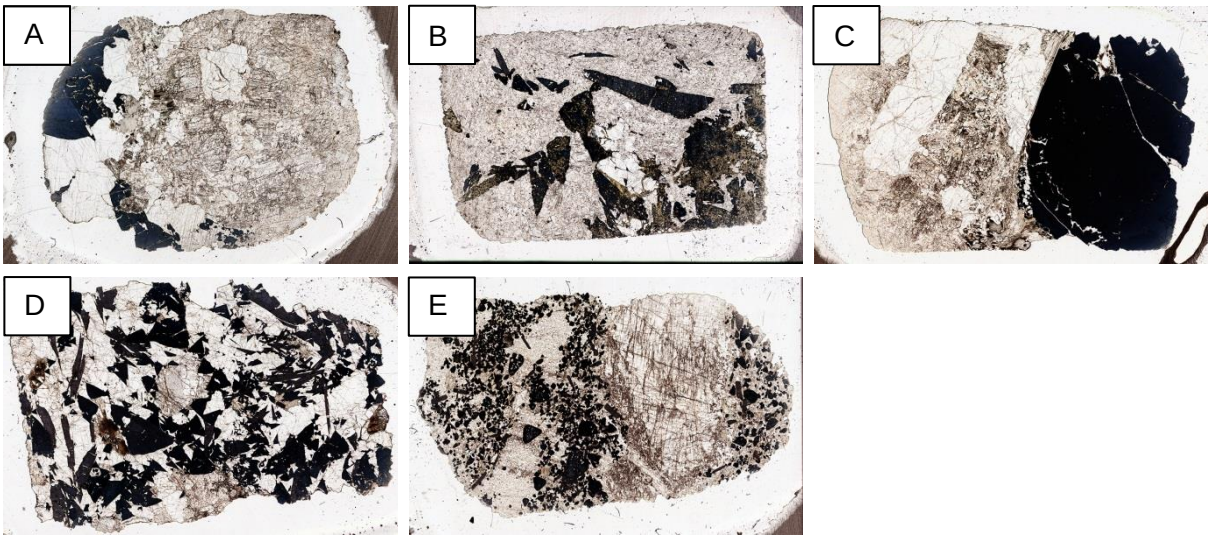

Appendix 7.3.1- Tourmaline Thin Section Scans: A) sample 690a; B) sample 690B; C) sample 690C; D) sample 20160; E) sample 18081715.

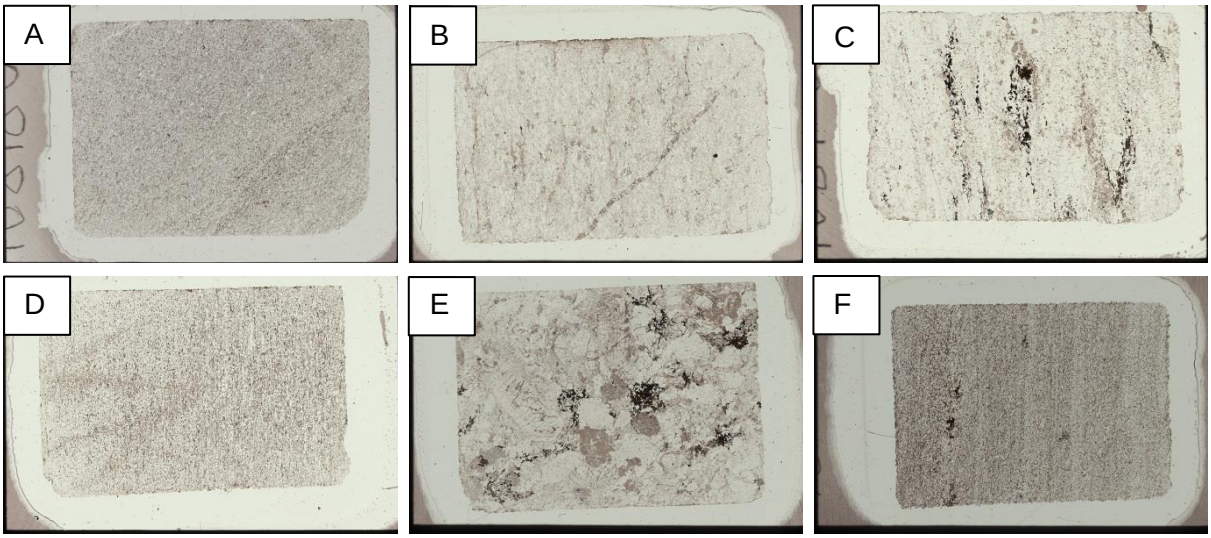

Appendix 7.3.2- Host Rocks Thin Section Scans: A) sample 04061801; B) sample 04061802; C) sample 05061801; D) sample 05061802; E) sample 05061803; F) sample 05061804.

Appendix 8.4: Mineral Inventory

Appendix 8.4 : Mineral inventory from the Spro area adapted from - https://www.mindat.org/loc-32870.html.

Albite	$NaAlSi_3O_8$
var: Oligoclase-Albite	$NaAlSi_3O_8$
Anatase	TiO_2
Apatite	$Ca_5(PO_4)_3X$
Bastnäsite	$(REE)CO_3F$
Bertrandite	$Be_4Si_2O_7(OH)_2$
Beryl	$Be_3Al_2Si_6O_{18}$
Calcite	$CaCO_3$
Chalcopyrite	$CuFeS_2$
Columbite-(Fe)-Columbite-(Mn) Series	$Fe^{2+}Nb_2O_6$ to $Mn^{2+}Nb_2O_6$
Euxenite-(Y)	$(Y,Ca,Ce,U,Th)(Nb,Ta,Ti)_2O_6$
Fluorite	CaF_2
Galena	PbS
Gypsum	$CaSO_4 \cdot 2H_2O$
Hydrocerussite	$Pb_3(CO_3)_2(OH)_2$
Malachite	$Cu_2(CO_3)(OH)_2$
Microcline	$KAlSi_3O_8$
Microlite Group	$(Ca,Na)_2Ta_2(O,OH,F)_7$
Molybdenite	MoS_2
Monazite	$(Ce,La)PO_4$
Muscovite	$KAl_2(Si_3Al)O_{10}(OH)_2$
Pyrite	FeS_2
Quartz	SiO_2
Samarskite-(Y)	$YFe^{3+}Nb_2O_8$
Thorite	$ThSiO_4$
Topaz	$Al_2SiO_4F_2$
Tourmaline (schorl)	$NaFe_3^{2+}Al_6(Si_6O_{18})(BO_3)_3(OH)_3OH$
Zircon var. alvite	$Zr(SiO_4)$, commonly referred to as a metamict hafnium-rich zircon

Appendix 8.5-16 are attached as excel spreadsheets.

Appendix 8.5: ICP-MS bulk rock geochemistry data of the investigated host rock samples from the Spro area: 04061802, 05061801, 05061803, 05061804, 05061802, 04061801

Appendix 8.6: ICP-MS bulk rock geochemistry data of the investigated pegmatite samples samples from the Spro area: bulk pegmatite – 16091806 and Albite zones – 690.

Appendix 8.7: EPMA-acquired data of Tourmaline samples chemical compositions.

Appendix 8.8: EPMA-acquired data of Feldspars chemical compositions.

Appendix 8.9: EPMA-acquired data of Micas chemical compositions.

Appendix 8.10:SEM/EDS-acquired data of minerals present in tourmaline sample 690a.

Appendix 8.11:SEM/EDS-acquired data of minerals present in tourmaline sample 690b.

Appendix 8.12:SEM/EDS-acquired data of minerals present in tourmaline sample 690c.

Appendix 8.13:SEM/EDS-acquired data of minerals present in tourmaline sample 20160.

Appendix 8.14:SEM/EDS-acquired data of minerals present in tourmaline sample 18081715.

Appendix 8.15:SEM/EDS-acquired data of minerals present in amphibole gneiss sample 18081715 for investigation of tourmaline presence in the host rocks.

Appendix 8.16:SIMS-acquired data of tourmaline B-isotopic composition in sampls 690a, 690b and 690c.